ROTORDYNAMIC AND THERMAL ANALYSES OF COMPLIANT FLEXURE PIVOT TILTING PAD GAS BEARINGS

A Dissertation

by

KYU-HO SIM

Submitted to the Office of Graduate Studies of
Texas A&M University
in partial fulfillment of the requirements for the degree of

DOCTOR OF PHILOSOPHY

August 2007

Major Subject: Mechanical Engineering

ROTORDYNAMIC AND THERMAL ANALYSES OF COMPLIANT FLEXURE PIVOT TILTING PAD GAS BEARINGS

A Dissertation

by

KYU-HO SIM

Submitted to the Office of Graduate Studies of
Texas A&M University
in partial fulfillment of the requirements for the degree of

DOCTOR OF PHILOSOPHY

Approved by:

Chair of Committee,	Daejong Kim
Committee Members,	Alan B. Palazzolo
	Gerald L. Morrison
	Wayne N.P. Hung
Head of Department,	Dennis L. O'Neal

August 2007

Major Subject: Mechanical Engineering

ABSTRACT

Rotordynamic and Thermal Analyses of

Compliant Flexure Pivot Tilting Pad Gas Bearings. (August 2007)

Kyu-Ho Sim, B.S., Yeonsei University;

M.S., Korea Advanced Institute of Science and Technology

Chair of Advisory Committee: Dr. Daejong Kim

Rotordynamic and thermal analyses of compliant flexure pivot tilting pad gas bearings were performed. First, compliant flexure pivot tilting pad gas bearings with pad radial compliance (CFTPBs) were introduced and designed for high-speed oil-free micro turbomachinery. The pad radial compliance was for accommodation of large rotor growth at high speeds. Parametric studies on pivot offset, preload, and tilting stiffness were performed using non-linear orbit simulations and coast-down simulations for an optimum design. Second, coast-down tests for imbalance response and stability of typical rotor-bearing system with a rigid rotor and two CFTPBs designed from the above design studies were conducted over operating speeds up to 55 krpm. Prediction of synchronous rotordynamic responses was made in terms of critical speed for various imbalance modes by using a rotordynamic analysis software (XLTRC), combined with dynamic force coefficients from the perturbation analysis. For stability analyses, a generalized orbit simulation program was developed considering both the translational and angular rotor motions with two different bearings. Linear stability analyses for the

conical vibration mode were also performed by using XLTRC and the perturbation analysis based on the Lund method. Predictions of whirl speed showed good agreement to the tests, but the estimated onset speed of instability appeared lower than the measured instability. Finally, a new thermo-hydrodynamic analysis model of a typical rotor-bearing system with CFTPBs was presented, accompanying linear perturbation analyses to investigate thermal effects on the rotordynamic performance. A numerical procedure was established for solving the generalized Reynolds equation, the 3-D energy equation, and the associated boundary conditions at the pad inlet flow and solid walls (rotor and pad) simultaneously. Parametric studies were conducted on nominal clearance and external load. Nominal clearance showed significant influence on temperature fields, and external load had uneven thermal effects among pads. Case studies with heat flux and temperature boundary conditions on the rotor end surface were performed to simulate various working conditions of the bearing. Large rotor thermal growth due to the high rotor temperature showed noticeable influence on rotordynamic performance by increasing direct stiffness and damping coefficients.

To
My family and friends

ACKNOWLEDGEMENTS

I would like to express my sincere gratitude to my academic advisor, Dr. Daejong Kim, for his inspiration, advice, and encouragement. He helped me to be a productive and professional researcher. I also thank my committee members, Dr. Palazzolo, Dr. Morrison, Dr. Hung, and Dr. Jung. I appreciate the Turbomachinery Laboratory and all the members for providing functionalized research facility and participating in many helpful discussions. I also appreciate Dr. Jongsoo Kim at KMC Bearings, Inc. for valuable support. Financial support from TEES is also acknowledged.

Special thanks go to Mr. Taeho Kim for valuable discussions on this research and also to my former and current colleagues: Juho Song, Soonkuk Kim, and Aaron Rimpel. In addition, I was fortunate to share priceless experience and memories with Ickchan Kim, Yeonseok Kim, Minseok Ko, Clint Carter, Eric Hensley, Bill Roberts, Brandon Rodgers and other Korean and American friends. Finally, from the bottom of my heart, I thank my parents and brother who have supported me throughout my studies. Without them, my work would not have been accomplished.

TABLE OF CONTENTS

CHAPTER Page

CHAPTER Page

LIST OF TABLES

LIST OF FIGURES

FIGURE Page

FIGURE Page

FIGURE Page

FIGURE Page

NOMENCLATURE

C	Nominal bearing clearance [m]
$e_{X,,}e_Y$	Journal eccentricities in X and Y [m]
h	Film thickness [m]
H	Dimensionless film thickness (=h/C)
i_p	Dimensional pad mass moment of inertia for the tilting motion [kg-m^2]
k_ϕ	Dimensional pad tilting stiffness [N-m/rad]
k_δ	Radial stiffness of pivot [N/m]
L	Axial length of bearing [m]
m_r	Rotor mass [kg]
m_p	Pad mass [kg]
p	Pressure in gas film [Pa]
p_a	Atmospheric pressure [Pa]
P	Dimensionless pressure (=p/p_a)
r_p	Preload [m]
r_g	Radial rotor growth [m]
r_{gc}	Centrifugal rotor growth [m]
r_{gt}	Thermal rotor growth [m]
R	Bearing radius [m]
X, Y, Z	Bearing global coordinates

ϕ	Tilting angle of each pad [rad]
δ	Radial motion of each pad [m]
Λ	Bearing number ($\Lambda=6\mu\Omega R^2/p_aC^2$)
θ	Circumferential coordinate [rad]
θ_p	Angular location of pivot web [rad]
σ	Squeeze number ($\sigma=12\mu\omega R^2/P_aC^2$)
τ	Non-dimensional time ($\tau=\omega t$)
Ω	Rotor spin speed [rad/s]

Material properties

c_p	Specific heat capacity of air [J/kg°K]
k	Heat conductivity of air [W/(mK)]
k_r	Heat conductivity of rotor [W/(mK)]
μ	Viscosity of air [Pa-s]
ρ	Density of air [kg/m^3]
α	Linear thermal coefficient of rotor
E	Elastic modulus of rotor [N/m^2]
ρ_r	Density of rotor [kg/m^3]
ν	Poison's ratio of rotor

Subscript

p	Pad (exception: preload, specific heat)
r	Rotor

Chapter III

$\varepsilon_X, \varepsilon_Y$	Non-dimensional journal eccentricities in X and Y(ε=e/C)
F_p	Force on each pad in radial direction due to film pressure [N]
F_X, F_Y	Bearing reaction force components applied to rotor [N]
$\overline{F}_X, \overline{F}_Y$	Summations of bearing reaction force and destabilizing force averaged over one cycle along the X and Y direction [N]
i_r	Mass moment of inertia of rotor along the rotational axis [Nms^2/rad]
R_i	Rotor inner radius [m]
T_f	Frictional torque applied to rotor [Nm]
T_m	Motor torque applied to rotor [Nm]
T_p	Tilting torque on each pad due to film pressure [Nm]
T	Temperature in air film [^{o}K]
T_∞	Ambient temperature [^{o}K]
u_{im}	Imbalance radius [m]

Chapter IV

d	Dimensional split distance [m]
D	Non-dimensional split distance (D=d/C)
$d_{\alpha\beta}$	Damping force coefficient [N-s/m]; $\alpha, \beta = X, Y$
$f_{p\delta}$	Radial force to each pad due to film pressure [N]

$F_{p\Psi}$ Non-dimensional radial force to a pad due to film pressure ($F_{\Psi} = \frac{f_{\delta}}{p_a R^2}$)

ΔH Non-dimensional perturbed film thickness

H_{α} Non-dimensional perturbed film thickness gradient (α=*X, Y, Φ, Ψ*)

I_p Non-dimensional pad mass moment of inertia for the tilting motion ($I_p = \frac{C\omega^2}{p_a R^4} i_p$)

$k_{\alpha\beta}$ Stiffness force coefficient [N/m]; α, β = *X, Y*

K_{Φ} Non-dimensional pad tilting stiffness ($K_{p\Phi} = \frac{C}{p_a R^4} k_{p\phi}$)

K_{Ψ} Non-dimensional pad radial stiffness ($K_{p\Psi} = \frac{C}{p_a R^2} k_{p\delta}$)

M_p Non-dimensional pad mass ($M_p = \frac{C\omega^2}{p_a R^2} m_p$)

$m_{p\phi}$ Tilting moment to each pad due to film pressure [N-m]

$M_{p\Phi}$ Non-dimensional tilting moment to a pad due to film pressure ($M_{\Phi} = \frac{m_{\phi}}{p_a R^3}$)

ΔP Non-dimensional perturbation of pressure field

P_{α} Non-dimensional perturbed pressure gradient (α=*X, Y, ϕ, δ*)

R_p Non-dimensional preload ($R_p = r_p/C$)

R_g Non-dimensional radial rotor centrifugal growth ($R_g = r_g/C$)

W Non-dimensional external force normalized by a reference load

	($W_0=p_aR^2$)
$\Delta W_{X,Y}$	Perturbation of external forces in X and Y [N]
X, Y	Cartesian coordinates for rotor motion
$Z_{\alpha\beta}$	Non-dimensional impedance matrix coefficients ($\alpha, \beta=X, Y, \phi, \delta$)
$[Z_R]$	Non-dimensional system impedance matrix
$\Delta\varepsilon_{X,Y}$	Non-dimensional perturbation of rotor motions in X and Y
Φ	Non-dimensional tilting angle of each pad ($\Phi = \phi R / C$)
Ψ	Non-dimensional radial motion of each pad ($\Psi = \delta / C$)
$\Delta\Phi$	Non-dimensional perturbed radial motion of a pad
$\Delta\Psi$	Non-dimensional perturbed tilting angle of a pad
Ω_s	Onset speed of instability: threshold speed [rad/s]
ω	Excitation frequency of perturbation [rad/s]
ω_s	Whirl speed on instability [rad/s]
ξ	Whirl frequency ratio ($=\omega_s/\Omega$)

Chapter V

h_c	Heat convection coefficient [W/m^2K]
L	Axial length of bearing [m]
$\dot{m}_{exit}$	Exit flow [kg/s]
$\dot{m}_{suc}$	Sucked ambient air [kg/s]
$\dot{m}_{inlet}$	Inlet flow [kg/s]

Q_{conv1}, Q_{conv2}	Axial heat flux in the rotor at bearing edge [W]
Q_E, Q_C	Heat flux boundary condition at rotor end [K]
T_E, T_C	Temperature boundary condition at rotor end [K]
t_p	Pad thickness [m]
t_r	Rotor wall thickness [m]
T_{bs}	Bearing shell temperature [K]
T_{exit}	Exit flow temperature [k]
T_{inlet}	Inlet flow temperature [k]
T_{suc}	Sucked ambient air temperature [k]
T_{r_av}	Averaged rotor temperature along the rotor axis [K]
T_{f_av}	Averaged air film temperature for all pads [K]
T_{p_av}	Averaged pad temperature for all pads [K]
T_r	Local rotor temperature along rotor axis [K]
T_p	Local pad temperature along radial direction [K]
U	Circumferential linear velocity of rotor surface
u, v, w	Air velocity component in the x, y, z directions
x, y, z	Cartesian coordinates for air film
Φ	Heat dissipation function

CHAPTER I

INTRODUCTION

1.1 Background

Small oil-free turbomachinery require very high-speed operations to achieve meaningful power and efficiency. The high-speed operations can cause a noticeable temperature increase, due to large viscous heat dissipation in the fluid film between rotor and bearing, as well as significant centrifugal growth (and decrease of film thickness). Rotor growth in the radial direction, caused by centrifugal force and thermal expansion, has a large influence on the performance of the bearing-rotor system. Furthermore, when the rotor growth becomes too large, the rotor-bearing system can experience operation failure. Therefore, high-speed turbomachinery require a compliant surface structure in the bearing to accommodate the large rotor growth.

Ideal tilting pad gas bearings are known to have very high stability due to self-adjusting tilting motions of the pads, following the rotor movements [1]. Conventional pivots such as axial pins or ball-sockets cause a stack-up of manufacturing tolerance and pivot wear due to continuous sliding contact [2], rendering high manufacturing cost and limited reliability. Moreover, they cannot accommodate rotor growth because the tilting pads are fixed in the radial direction.

Recently, flexure pivot tilting pad gas bearings (FTPBs) have been investigated extensively [3-5]. The FTPBs [5] do not experience pivot wear or tolerance

---

This dissertation follows the style of Journal of Tribology.

accumulation because of their monolithic structure, which is manufactured by a simple cutting process, e.g. the wire EDM (electrical discharge machining), without an assembly process. To accommodate the rotor growth, various compliant structures have been employed behind the tilting pads (viscoelastic materials, mechanical compliant structure, etc.). For FTPBs manufactured via wire EDM, beam structures behind the pivots are common approaches for design and manufacturing simplicity [3,6]. Those configurations allow radial movements of pads, which can accommodate rotor growth very effectively (called compliant flexure pivot tilting pad gas bearings (CFTPBs) in this dissertation). In small high-speed oil-free turbomachinery, CFTPBs can be a good alternative to foil gas bearings.

1.2 Objectives and Dissertation Outline

The main objectives of this dissertation are to present rotordynamic analyses with experimental validation to predict the dynamic performance of CFTPBs, and to develop a thermo-hydrodynamic (THD) model of a rotor-bearing system with CFTPBs for more sophisticated analyses of the bearing performance. Comprehensive rotordynamic studies are performed by developing numerical programs for the orbit simulation and the perturbation analysis. Experimental studies are also conducted to validate the rotordynamic analyses by constructing a test rig with CFTPBs designed by parametric studies, and performing coast-down tests for imbalance response and stability. A THD analysis program for a typical rotor-bearing system with CFTPBs is developed and simulated for parametric studies on a few important design parameters

and case studies for various operating conditions. Linear perturbation analyses are also conducted to investigate thermal effects on the rotordynamic performance.

In Chapter II, a review of the literature about rotordynamic analyses and experiments of tilting pad bearings is presented. It also contains a review of thermal analyses of fluid bearings.

In Chapter III, design studies for CFTPBs were conducted using the orbit simulation. The orbit simulation program for CFTPBs was developed by incorporating pad and rotor motions to air film pressure. The orbit simulations including coast-down simulations were performed for parametric studies of design parameters of CFTPBs.

In Chapter IV, coast-down tests for imbalance response and stability were conducted, and the results were investigated by using the orbit simulation and the perturbation analysis with XLTRC. The orbit simulation program was developed for general rigid rotor motion with two different bearings. The perturbation analysis program was implemented based on the formulation in [7].

In Chapter V, a THD model capable of predicting the thermal performances of a rotor-bearing system with CFTPBs was presented. Parametric studies on several design parameters and case studies on various operating conditions were conducted to provide a useful design guide, accompanying linear perturbation analysis to investigate thermal effects on rotordynamic performance.

In Chapter VI, concluding remarks and contributions of this research were presented to summarize the findings of this work, and future research directions were proposed.

CHAPTER II

LITERATURE REVIEW

2.1 Hydrodynamic Analyses

An orbit method, which traces the path of journal center by solving rotor radial motions and unsteady Reynolds Equation simultaneously in time domain [8,9], can predict complete nonlinear behavior including sub-synchronous and super-synchronous whirling motions, molecular rarefaction effect at high temperature under very small bearing clearances and arbitrary external loadings, to name a few. On the other hand, a perturbation method [10-13] has been widely used to investigate the dynamic performance of a rotor supported by gas bearings. In the perturbation method, force coefficients (stiffness and damping coefficients) of the support bearings are calculated from perturbed pressure field about a static equilibrium position. Once the force coefficients of the support bearings are calculated, stability of the system can be decided from the signs of eigenvalues for the rotordynamics equations.

Lund [14] first published a perturbation solution of the Reynolds equation to calculate the dynamic force coefficients of tilting pad bearings. Lund [15] described how the dynamic force coefficients are employed to investigate critical speed, imbalance response, and rotor-bearing stability of gas-lubricated tilting pad bearings. Zhu and San Andrés [4] performed experimental tests on hybrid (hydrostatic and hydrodynamic) FTPBs. Coast-down imbalance response tests were performed with the hydrodynamic and hybrid modes for various hydrostatic supply pressures. The test bearings showed

stable operation up to 100 krpm with a hydrostatic pressure range from 2.4 ~ 5.2 bar; however, in the hydrodynamic mode, sub-synchronous responses appeared at 81 krpm with the whirl frequency ratio of 0.2. Higher hydrostatic pressures led to higher critical speeds (direct stiffness), and lower damping ratios. Delgado et al [7] conducted a perturbation analysis of brush seals with reverse rotation capability. The pads on the brush seals have the same mechanism as the tilting pads in terms of preload and pad motions in the tilting, radial, and transverse (tangent to circumference) directions. The perturbation method developed for the brush seals [7] provided a foundation for perturbation analyses of hydrodynamic FTPBs in [4]. San Andrés [16] further developed the analytical model used in [4] to perform perturbation analyses of hybrid FTPBs. The new model showed a better agreement of calculated damping coefficients with the experimentally measured ones. The paper provides a good foundation for understanding rotor-bearing characteristics of hybrid FTPBs.

2.2 Thermal Analyses

In the fluid film bearings, numerous studies have been carried out. Cope [17] proposed a simplified energy equation neglecting temperature variations across the fluid film. Numerical studies in [18,19] presented simultaneous solutions for the Reynolds equation and the energy equation including temperature variations across the film, and showed that the inclusion of the temperature variation may have a significant influence on the pressure and temperature distributions in the film. Dowson [20] introduced the

generalized Reynolds equation and the energy equation, taking into account viscosity and density variations across the film.

Knight and Barrett [21] established a 2D THD model for oil-lubricated tilting pad bearings, where the bulk temperature was calculated only in the circumferential direction. Temperature profile across the film was approximated by a 2^{nd} order polynomial using the journal and pad surface temperatures as wall boundary conditions, and temperature gradients at the journal and pad surfaces were obtained from the 2^{nd} order polynomials. Heat conduction in the pads was assumed to be purely radial with a uniform temperature on the backside of each pad. Journal surface temperature was assumed to be constant along the circumference, and calculated by averaging the film temperature around the circumference. Inlet flow temperature at the leading edge of a pad was obtained by mass and heat balance of the exit flow from the preceding pad, the supply oil, and the inlet flow to the pad in the mixing chamber between pads, assuming heat transfer through the solid walls negligible. Results of sample calculations indicated that the two bottom pads were slightly warmer than the two top pads, and temperature distribution of the lubricant in a pad was slightly increased at the trailing edge. Knight and Barrett [21] gives a simple way to calculate the bulk temperature considering rotor and pad temperatures as wall boundary conditions.

Taniguchi et al [22] performed 3D THD analyses with the upwind finite difference scheme in both laminar and turbulent flow regimes for oil-lubricated tilting pad bearings. Film temperature of the exit and side flows at the pad edges were obtained by parabolic extrapolation of the near edge temperatures. Experimental studies were also

conducted with a 19 inch test bearing. The numerical simulations showed a good agreement in film pressure, pad surface temperature, and film thickness with the experiment results.

Kim et al [23] introduced a thermoelastohydrodynamic (TEHD) model incorporating heat transfer in the lubricant and elastic deformation of pads into dynamic force coefficient calculation. A 2D energy equation was formulated with an assumption of negligible temperature variation in the axial direction, and implemented by finite element method with the upwind scheme. Thermal shaft expansion was taken into account in calculating the film thickness. As a result, the simulated temperature distribution of the shaft and the loaded pads had a good agreement with the experiment results given in [24]. The two papers above commonly made use of a 2D heat conduction model in the radial and circumferential directions for pad temperature solution, and employed the mass and heat balance in the mixing chamber for the pad inlet flow temperature calculation. Journal surface temperature was assumed to be constant along the circumference, and they assumed that net heat flux from the pads to the shaft is zero as adopted by [25].

Salehi et al [26] conducted analytical and experimental investigations on the thermal characteristics of air-lubricated compliant foil bearing. In their analysis, a linear viscosity-temperature relation, which agrees well with measurements in the range of 0 to 550℃, was employed, and a Couette flow approximation [27] was adopted to simplify the energy equation to 1-D problem, where heat flows induced by pressure gradients are negligible as compared to those by the Couette flow. As a result, the simplified analyses

uncouple the energy equation (temperature) from the Reynolds equation (pressure), leading to only a temperature variation along the circumferential direction. Even though the uncoupling of temperature field in the film from pressure fields gave at most 20% overestimation of the film temperature, this paper elicited overall thermal characteristics of compliant air foil bearings, and showed that Couette approximation provides reasonable approximations of temperature within moderate operating conditions.

The most advanced THD analysis so far on the air foil bearing has been performed by Peng and Khonsari [28]. They developed a 3-D THD model accounting for the compressibility and viscosity-temperature characteristic of air and the compliance of the bearing surface. In their analysis, the heat conduction across the air film is assumed to be dominant over heat conductions along the film plane as adopted in [26], and only the velocity gradients with respect to the cross-film direction are considered. The linear viscosity-temperature relationship adopted in [26] was used. However, their model assumes the top foil can take sub-ambient pressure at trailing edge of the top foil and generate suction flow into the foil bearing, which can be unrealistic for actual foil bearings. Inlet temperature at leading edge of the top foil is calculated by averaging temperatures of the suction and recirculation flows. Shaft temperature is estimated by the mean temperature of the side flow without calculating rotor temperature directly. Heat transfer to rotor was not considered and only the radial heat conduction through the top foil (and convection by cooling air through the space between the top foil and bearing sleeve) is taken into account.

THD studies on fluid film bearings above [22,23,28] indicate thermal effects cannot be neglected in design and analyses of hydrodynamic gas bearings. Temperature rise due to the viscous dissipation in the gas film leads to change of gas viscosity and higher temperature of rotor, which causes thermal expansion of the rotor, change of average film thickness, and then overall bearing performance. The thermal analyses are more important in high speed microturbomachinery. While the centrifugal growth can be estimated by elasticity theory or FEM for the rotor, the thermal expansion should be evaluated by investigating all the heat flows through the bearing and rotor.

CHAPTER III

DESIGN STUDY OF CFTPBS*

3.1 Introduction

Introduced in this chapter is a compliant flexure pivot tilting pad gas bearing with pad radial compliance (CFTPBs) as an alternative to the foil gas bearings. An ideal tilting pad gas bearing (with no tilting stiffness) may have no instability because of zero cross-coupled stiffness due to self-adjusting tilting motion of pads following the rotor movements [1]. However, conventional pivots such as axial pins or ball-sockets cause tolerance accumulation and pivot wear [2], rendering high manufacturing cost and limited reliability. Furthermore, traditional tilting pad gas bearings cannot accommodate rotor thermal and centrifugal growth, which are very common in high-speed turbomachinery. Flexure pivot tilting pad gas bearings [4-6] have no pivot wear and tolerance accumulation with a penalty of finite tilting stiffness because the pads and bearing housing are constructed as a monolithic structure. Despite the very simple structure and proven performance of these types of bearings, detailed design studies and experimental studies are very few [2,4,16]. However, the simple flexure pivot tilting pad gas bearings cannot accommodate rotor growth either. Straight beam structure behind the pivot (Fig. 3.1) has been adopted [6] for years to solve the rotor growth issues but

---

*Reprinted with permission from "Design of Flexure Pivot Tilting Pad Gas Bearings for High Speed Oil-Free Micro Turbomachinery" by Sim, K. and Kim, D., 2007, Journal of Tribology, **129**, pp. 112-119. 2007 by ASME

systematic design studies are lacking. A conceptual design of CFTPB is presented in Fig. 3.1.

This chapter provides detailed parametric studies using nonlinear orbit simulation for optimal selection of pad radial stiffness, nominal clearance, and other design variables, such as pivot offset and preload, and investigates the characteristics of the flexure pivot tilting pad gas bearings with radial compliance, and for design optimization. An orbit method, which traces the path of journal center by solving rotor radial motions and unsteady Reynolds Equation simultaneously in time domain [8,9], can predict complete nonlinear behavior including sub-synchronous and super-synchronous whirling motions, molecular rarefaction effect at high temperature under very small bearing clearances and arbitrary external loadings, to name a few.

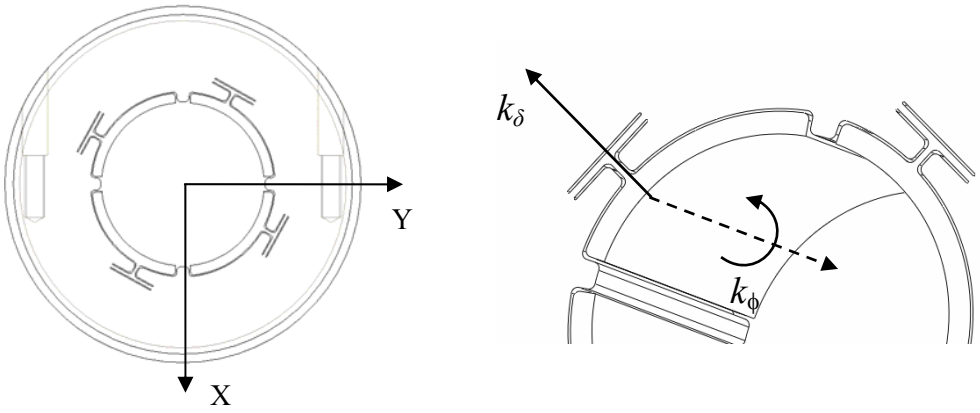

(a) Overall shape (b) Tilting and radial stiffness

Fig. 3.1 Compliant flexure pivot tilting pad bearing with radial stiffness

3.2 Formulation

A rotor is assumed rigid and aligned with bearing along the axial direction. The orbit simulation involves solving journal motions, pad dynamics, and unsteady Reynolds equation simultaneously. Design parameters and rotor and pad motions of CFTPBs are presented in Fig. 3.2. Each pad has finite tilting (ϕ) and radial (δ) stiffness. Non-dimensional film thickness, H, normalized by nominal bearing clearance C, is given by

$$H(\theta) = h(\theta)/C \tag{3.1}$$

$$h(\theta) = C - \left(r_{gc} + r_{gt}\right) + e_X \cos\theta + e_Y \sin\theta - R\phi \sin\left(\theta - \theta_p\right) - \left(r_p - \delta\right)\cos\left(\theta - \theta_p\right)$$

where e_X and e_Y are respective eccentricities of the journal center along the X and Y directions, ϕ is the pad tilting angle, δ is the pad radial displacement, r_{gc} is the rotor centrifugal growth, r_{gt} is the rotor thermal growth averaged along the rotor axis, and r_p is the preload (pad center offset). The nominal clearance is defined as the clearance at $\pm 90^o$ from the pivot, and physically the set bore clearance (clearance at pivot) plus the pad center offset (preload). θ_p is the angular position to the pivot, and defines the pivot offset which is the ratio of the angle of the pivot from the pad leading edge to the total pad angle. In this design study, the thermal rotor growth is assumed to be zero, and in Chapter VI, the effects of the thermal growth will be investigated.

As Fig. 3.1 indicates, hydrodynamic pressure on the pad generates both tilting moment and transverse (tangential) force on the pad. The tilting motion can also generate transverse motion of the tilting pad along the circumferential direction. However, from simple beam theory [29], the transverse deflection of pad equals to $\phi L_p/2$,

where L_p is the length of the pivot web. Because of the very small clearance, the maximum allowable tilting angle is about 10^{-3} radian and the maximum transverse deflection of the pad is less than 1μm when L_p~0.001m. In addition, net transverse component of the hydrodynamic pressure force on a pad is very small, and the direction is opposite to the transverse deflection due to the tilting motion. Furthermore, for given web geometry (straight beam), the ratio of transverse stiffness to tilting stiffness is $3/L_p^2$. For given web length (~0.001m), transverse stiffness is significantly larger than tilting stiffness. Therefore, any coupled effect between the pad tilting motion and pad transverse motion is almost completely negligible. Preliminary orbit simulations considering the coupled effect produced no distinguishable results.

The preload is a non-dimensional distance between pad center and bearing center normalized by clearance C at $\pm 90^o$ from the pivot. Therefore, actual bearing clearance at pivot becomes $C(1-r_p)$. Note that bearing clearance at the leading and trailing edges of each pad is smaller than the nominal clearance because pad arc length is less than 90^o from pivot in either direction. The preload is a hydrodynamic preload generated by a converging bearing clearance at leading edge of each pad. Therefore, the higher the preload, the more wedge is formed in leading edge of each pad. The pivot offset is defined as the ratio of the angular position of pivot from the leading edge to the total pad arc length. Larger pivot offset provides more pad area with converging wedge for given tilting angle.

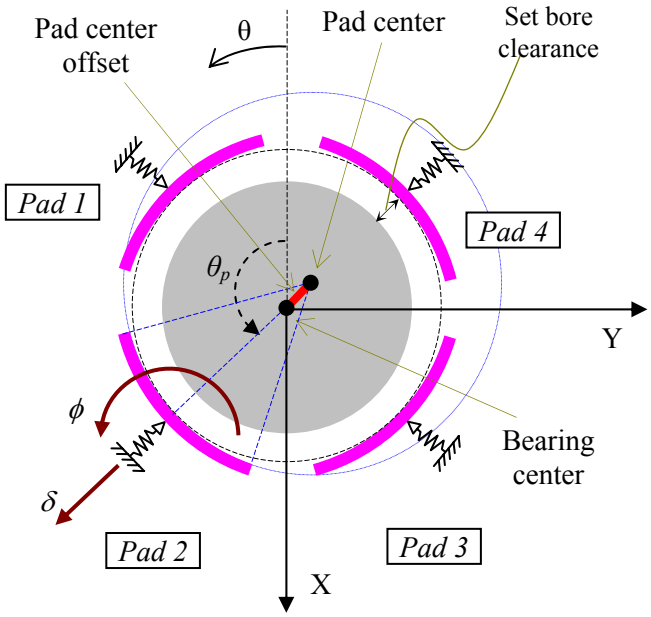

Fig. 3.2 Design parameters and rotor and pad motions of CFTPBs

With the film thickness given in Eq. (3.1), the pressure field can be obtained by solving the unsteady Reynolds Equation with an assumption of isothermal continuum flow given by

$$\frac{\partial}{\partial\theta}\left(PH^3\frac{\partial P}{\partial\theta}\right)+\frac{\partial}{\partial Z}\left(PH^3\frac{\partial P}{\partial Z}\right)=\Lambda\frac{\partial}{\partial\theta}(PH)+\sigma\frac{\partial}{\partial\tau}(PH), \tag{3.2}$$

$$\Lambda=\frac{6\mu\omega}{p_a}\left(\frac{R}{C}\right)^2,\ \sigma=2\Lambda\ .$$

Here, P is a dimensionless pressure normalized by atmospheric pressure (p_a), μ is air viscosity, θ is circumferential coordinate, Z is a dimensionless axial coordinate ($=z/R$), τ is a dimensionless time ($=\omega t$), Λ is a bearing number, and σ is a squeeze number.

Equations of rotor radial motions are given by:

$$m_r \ddot{e}_X = F_X + m_r u_{im} \omega^2 \cos \omega t + m_r g \,, \tag{3.3a}$$

$$m_r \ddot{e}_Y = F_Y + m_r u_{im} \omega^2 \sin \omega t \,, \tag{3.3b}$$

where m_r is a rotor mass, u_{im} is an imbalance radius, g is a gravity constant, and $F_{X,}$ and F_Y are dynamic bearing reaction forces applied to the rotor. The dynamic bearing reaction forces are calculated by solving Eq. (3.2). The dynamic equations for the pad radial and tilting motions are:

$$m_p \ddot{\delta} = F_p - k_\delta \delta \,, \tag{3.4}$$

$$i_p \ddot{\phi} = T_p - k_\phi \phi \,, \tag{3.5}$$

where δ and ϕ are pad radial motion and tilting angle of each pad, respectively. m_p and i_p are mass and moment of inertia of pad, F_p and T_p are radial force and tilting moment on each pad due to the dynamic film pressure, and k_δ and k_ϕ are radial and tilting stiffness of pivot, respectively.

Coast-down and speed-up simulations were used to find a critical speed and onset speed of instability, just like actual experiments. The equation for coast-down or speed-up is a simple first order differential equation, given by

$$i_r \dot{\omega} = T_m - T_f \,, \tag{3.6a}$$

$$T_f = C_0 \omega \,. \tag{3.6b}$$

Here i_r is a mass moment of inertia of the rotor along the axis of rotation, T_m is a motor torque and T_f is a total friction (or drag) torque generated from bearings and other parts of the rotor. The total friction was assumed proportional to the rotor speed with appropriate proportionality constant C_0. Coast-down simulation from a specific target speed begins with an initial speed-up from a certain speed lower than the target speed to eliminate numerical transient motions of the rotor and pads. During the initial speed-up, certain amount of motor torque is applied to reach the target speed. A numerical transition from the speed-up to coast-down occurs by setting motor torque zero once target speed has been reached.

The equations of rotor and pad motions, Eqs. (3.3-3.6), are solved using a 5^{th} order Adams-Bashforth scheme [30]. The unsteady Reynolds Equation is solved at every time step using the displacements and velocities of rotor and pads evaluated at the previous time step [8,9]. A Gauss-Seidal iteration method with power-law scheme was used for excellent numerical stability up to very large bearing numbers [31]. The number of grid points to solve the Reynolds Equation was 13×8 (θ and Z) for each pad. Numerical accuracy was confirmed by doubling the grid points with almost identical orbits within the difference of 3%.

3.3 Parametric Studies on Design Parameters

A baseline design for the parametric studies was a simple flexure pivot gas bearing without radial compliance, presented in [4]. Table 3.1 summarizes the base line design from [4].

Table 3.1 Baseline design, from [4]

Parameters	SI unit	
Number of pads	4	
Pad mass (m_p)	0.0072	kg
Pad inertia (i_p)	2.53×10^{-7}	kg-m^2
Pad start angle	9	degree
Pad arc length	72	degree
Pivot offset	0.6	
Preload (r_p)	0.4	
Tilting stiffness (k_ϕ)	20	Nm/rad
Nominal clearance (C)	20	μm
Bearing radius (R)	14.26	mm
Bearing length (L)	33.2	mm
Imbalance ($m_r r_u$)	414	mg-mm
Rotor mass (m_r)	0.414	kg
Air viscosity(μ)	1.85×10^{-5}	Pa-s

The characteristics of the time responses were investigated in terms of critical speeds and onset speeds of instability. The critical speed is defined as a speed at which the maximum synchronous amplitude occurs, and the critical speed is slightly higher than rotor-bearing natural frequency, where phase angle of the synchronous response to imbalance force becomes 90°. Onset speed of instability is defined as a speed at which a sub-synchronous motion (whirl) begins to occur. The frequency of the sub-synchronous motion with associated instability is sub-harmonic and approximately equal to the natural frequency of the bearing system [1]. The ratio of whirl speed and rotor rotational

speed is defined as whirl frequency ratio (WFR) and it is very close to 0.5 in plain journal bearings.

There are two types of sub-synchronous motions, bounded and diverging. Linearized system model with force coefficients from perturbation method regards the bounded sub-synchronous motion as unstable. On the other hand, non-linear orbit simulation can predict non-linear rotor behavior including the bounded sub-synchronous motions. In the experiment [4], small sub-synchronous motions around 81 krpm are initiated but it is not clear whether they are growing or bounded. Non-linear orbit simulations predict an initiation of sub-synchronous but bounded stable whirl at about 87 krpm as in Fig. 3.3(a) and Fig. 3.4. The orbits in Fig. 3.3 and the amplitude in Fig. 3.4 were plotted with non-dimensional eccentricity (ε) normalized by bearing clearance C. As shown in Fig. 3.3, the bounded sub-synchronous motion is maintained up to 115 krpm, above which the orbit begins to diverge.

Because the main purpose of this paper is to find an optimum design for the maximum operating speed without instability, even the bounded sub-synchronous motions are considered as onset of instability for conservative design practice. Therefore, 87 krpm is regarded as the onset speed of instability for the baseline design in this paper. Parametric studies were performed with respect to pivot offset, preload, and tilting stiffness, and brief results are presented. Here, the rotor was assumed rigid and any rotor growth was neglected.

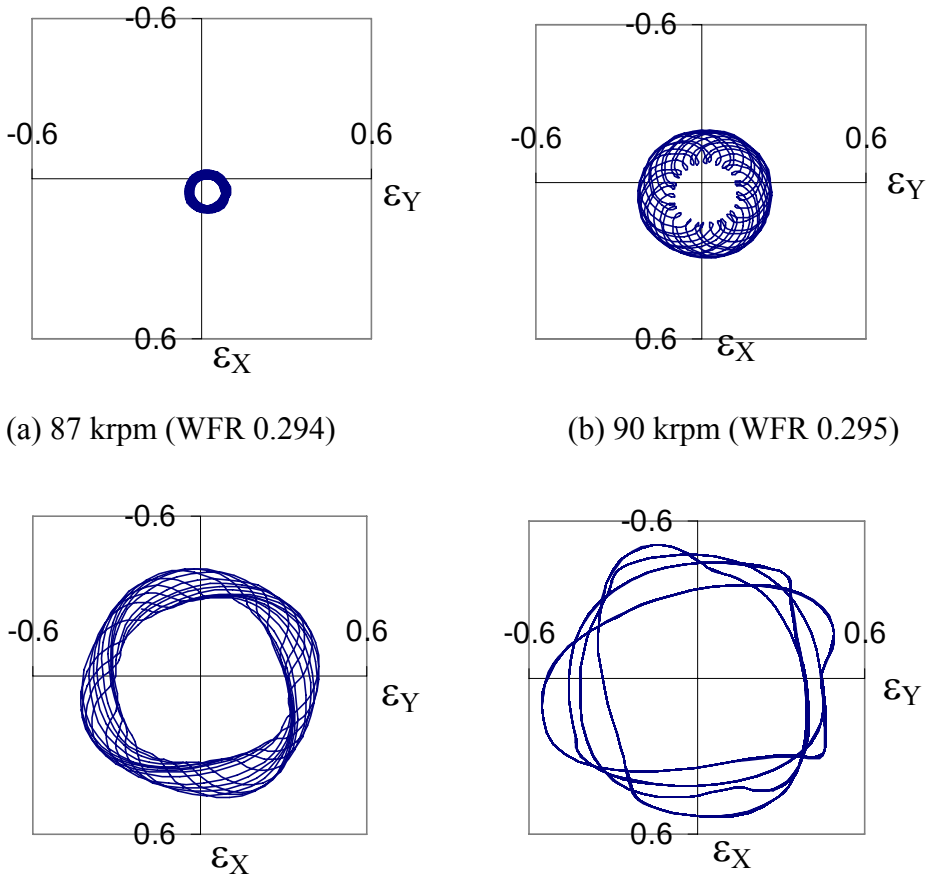

Fig. 3.3 Bounded sub-synchronous rotor orbit for baseline design

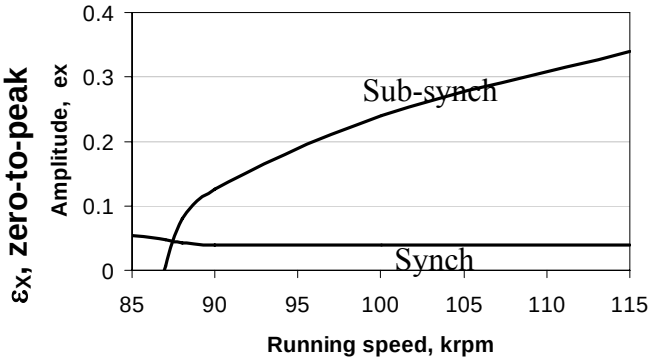

Fig. 3.4 Amplitudes of vibration components from 87 to 115 krpm (extracted from Fast Fourier Transform of the simulated vibration signal along the X direction)

A finite tilting stiffness is inevitable in flexure pivot tilting pad bearings since a beam-like structure connects the pad to the bearing housing. The finite tilting stiffness can make the rotor-bearing system unstable at high-speeds due to a certain amount of cross-coupled stiffness. As expected, smaller tilting stiffness increases the onset speed of instability but not the critical speed, which indicates the tilting stiffness affects mainly cross-coupled stiffness. However, tilting stiffness of the baseline design, i.e., 20 Nm/rad, was maintained in this design study to have a physically achievable web geometry by current manufacturing method (i.e., wire electrical discharge machining).

The responses for pivot offset of 0.5 and 0.7 and preload of 0.3 and 0.5 were compared with the baseline design. Overall bearing performance was very sensitive to both pivot offset and preload. The critical speed and the onset speed of instability were increased significantly as the pivot offset was increased from 0.5 to 0.7. Similar effects were observed as the preload was increased from 0.3 to 0.5. Higher pivot offset rendered higher average tilting angle, leading to increased wedge and stabilizing action. In case of preload, higher preload itself produces higher wedge on the pad. Therefore, higher values of the pivot offset and preload are desirable to make rotor-bearing system stable at high-speeds. However, pivot offset of 0.8 leads to very large rotor vibration amplitude at the critical speed due to reduction of damping ratio. Preload of 0.6 renders too small clearance at pivot, which can be detrimental to the accommodation of any rotor centrifugal growth that will be addressed later.

As expected, a combined effect of increased preload and pivot offset is very noticeable as presented in Table 3.2, where Set 0 is the baseline design with preload of

0.4 and pivot offset of 0.6, and Set 1 is for preload of 0.5 and pivot offset of 0.7. To reduce the maximum peak-to-peak vibration at critical speed, imbalance was reduced to 331mg-mm (80% of the value in Table 3.1) for the simulation for Set 1. As Table 3.2 shows, increasing both the pivot offset and preload increased the critical speed and onset speed of instability by about 60% and more than 400%, respectively.

Table 3.2 Increased critical speed and onset speed of instability by higher pivot offset and preload (C=20μm, tilting stiffness: 20Nm/rad)

	Pivot offset	Preload	Critical speed (rpm)	Onset speed of instability (rpm)
Set 0	0.6	0.4	35,000	87,000
Set 1	0.7	0.5	55,000	above 350,000

However, it should be noted that physically existing rotor centrifugal growth would limit the actual maximum operating speed. For example, a hollow shaft with wall thickness of 3mm has an upper speed limit of 110 krpm because of shaft growth of 10μm at pivot (preload 0.5 with C=20μm) from Eq. (3.7). Therefore, in order to achieve higher operating speeds, a physical mechanism to accommodate the rotor radial growth is required.

3.4 Estimation of Centrifugal Rotor Growth

In this design study, only the centrifugal rotor growth is considered assuming the rotor thermal growth is eliminated through an adequate cooling system. The rotor radial

centrifugal growth is predicted via the plain stress model of a thin circular disc [32], such that

$$r_g = \frac{1}{E}\left[(1-\nu)RC_0 - (1+\nu)\frac{1}{R}C_1 - \frac{(1-\nu^2)}{8}\rho_r\omega^2 R^3\right] \tag{3.7}$$

$$\text{with } C_0 = \frac{3+\nu}{8}\rho_r\omega^2(a^2+R^2) \text{ and } C_1 = -\frac{3+\nu}{8}\rho_r\omega^2 a^2 R^2$$

where ρ_r, E, ν, Ω are the density, Young's modulus, and Poison's ratio of the rotor, respectively, R_i is the inner radius of the rotor, and Ω is the rotor spin speed in rad/sec. Even if most rotors are long shaft, Eq. (3.7) agrees very well with finite element analyses for 120mm long rotor as shown in Fig. 3.5. Since the centrifugal growth is proportional to Ω^2, the growth is significant at high-speeds. The rotor growth of a hollow rotor made of steel with wall thickness of 3mm is more than 20μm above 150 krpm from Fig. 3.5, which implies the actual speed limit of the bearing with geometries in Table 3.1 will be less than 120krpm. Therefore, practically important design parameters for high-speed applications are the bearing nominal clearance and pad radial stiffness once preload and pad offset are determined.

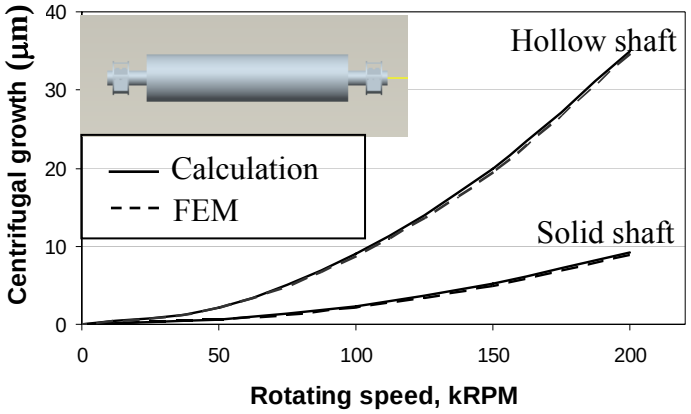

Fig. 3.5 Centrifugal growth of the steel hollow shaft (3mm thickness and 28.52mm outer diameter)

3.5 Design of Nominal Clearance and Radial Stiffness

The nominal clearance is an important design parameter to determine the stability of a bearing-rotor system. Generally, smaller clearance increases system stiffness, thus the critical speed and onset speed of instability. However, small clearance limits the maximum operating speed. Larger clearance has more allowance for rotor growth with a penalty of low load capacity. Another important aspect in selection of bearing clearance is heat generation due to gas viscosity.

Even if no thermal growth is assumed in this paper, the general trend of the effect of nominal clearance on the gas bearing temperature rise is noteworthy. Adopting adiabatic energy equation applied to journal bearings, neglecting heat conduction within the gas film and to the bearing/rotor [33], and also neglecting all the pressure gradient terms within the energy equations, an approximate solution of the adiabatic *averaged* gas film temperature across the film thickness can be derived as,

$$\frac{T(\theta)-b}{T_\infty - b} = \exp\left[\frac{2a\Omega}{\rho c_p}\left(\frac{R}{C}\right)^2 \int_0^\theta \frac{d\theta}{H^2}\right], \tag{3.8}$$

where θ is measured from the leading edge of each pad and T_0 is an ambient temperature at the leading edge of each pad. The a and b are appropriate regression constants for air viscosity $\mu = a(T-b)$ used in [26]. More details involved in the assumptions to achieve Eq. (3.8) can be found in [26,33]. Even though Eq. (3.8) overestimates the gas film temperature, a noticeable fact is that the gas film temperature is proportional to $\exp(1/C^2)$ at high-speeds. Therefore, nominal clearance should be as large as possible within performance requirements. However, too large nominal clearance deteriorates the bearing stability as will be discussed later.

Radial pad stiffnesses for parametric studies were selected in the range of $0.1\sim10\times10^7$ N/m with pivot offset, preload, and tilting stiffness from Set 1 in Table 3.2. To be sought is the right combination of pad radial stiffness and bearing clearance that can provide large average film thickness (over one rotational cycle at steady state) and stable operation beyond 100,000rpm. In general, a larger clearance can accommodate rotor growth more easily but can deteriorate the stability.

Net clearances at pivot with nominal clearance of 35μm for different pad radial stiffnesses considering rotor centrifugal growth is shown in Fig. 3.6(a). When the pad stiffness is above 4×10^7 N/m, the net clearance at pivot approaches zero, indicating the high pad radial stiffness cannot accommodate the rotor growth and limit the maximum speed below 180krpm. As speed is reduced, the net clearance at pivot increases.

Minimum radial stiffness for a stable operation up to 180 krpm appeared to be about 0.5×10^7 N/m. Finding exact lower limit of the radial stiffness was not attempted due to the limitation of repeated orbit simulations. Below the presumed lower limit, the bearing system became unstable with severe sub-synchronous motions at the speeds below 100 krpm. Simulation results for nominal clearance of 30μm are shown in Fig. 3.6(b). The centrifugal growth at 180 krpm is 27.9μm from Eq. (3.7), almost equal to the nominal clearance. Only the radial stiffnesses of 0.5×10^7 N/m and 1.0×10^7 N/m showed stable operations with very small net clearance below 1μm at pivot. Further decrease of pad radial stiffness below 0.5×10^7 N/m leads to instability at below 100krpm. As the maximum speed is reduced to 150krpm, the range of possible radial stiffnesses is extended to $0.5\sim4\times10^7$ N/m, and the net clearance at pivot also increases.

Coast down simulations of peak-to-peak amplitudes of ε_X for 40μm (Fig. 3.7) shows very interesting phenomena. Instability is initiated at around 32 krpm and terminated at 50 krpm for pad stiffness of 2.0×10^7 N/m. This anomaly can be explained from the parabolic curve of rotor centrifugal growth. As speed increases beyond 50 krpm, the rotor growth becomes large enough to decrease actual film thickness, thus suppress the instability.

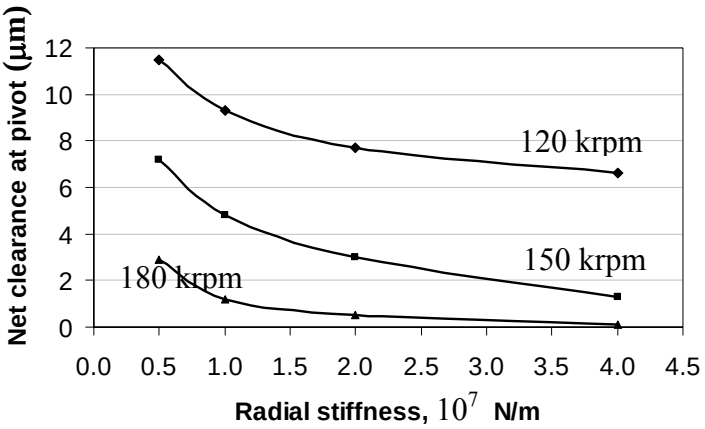

(a) C=35μm

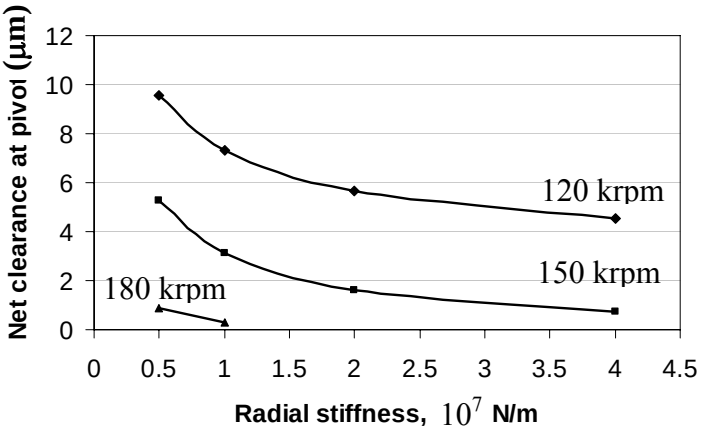

(b) C=30μm

Fig. 3.6 Simulated net clearance at pivot vs. radial stiffness with speed as a curve parameter

Peak-to-peak amplitudes of ε_X during the coast down simulations are presented in Fig. 3.8 for various stiffnesses with C=35μm. Table 3.3 presents critical speeds and damping ratios extracted from Fig. 3.8 using half power bandwidth method. As expected, increased damping ratio increases critical speeds and decreases peak vibrations at the critical speeds.

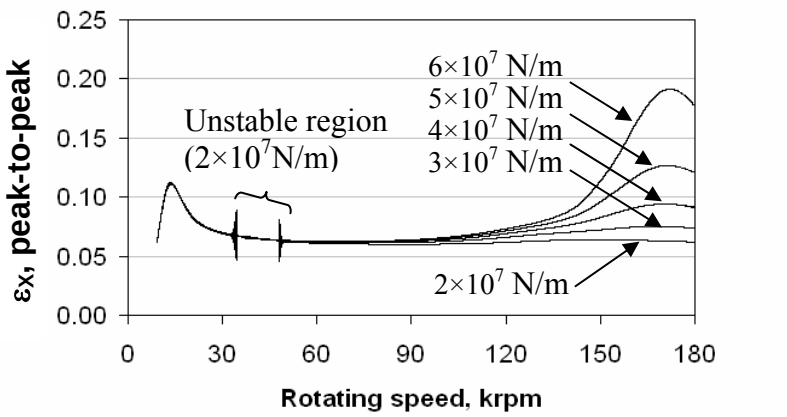

Fig. 3.7 Coast down simulations of peak-to-peak amplitudes of ε_X with respect to pad radial stiffness (C=40μm)

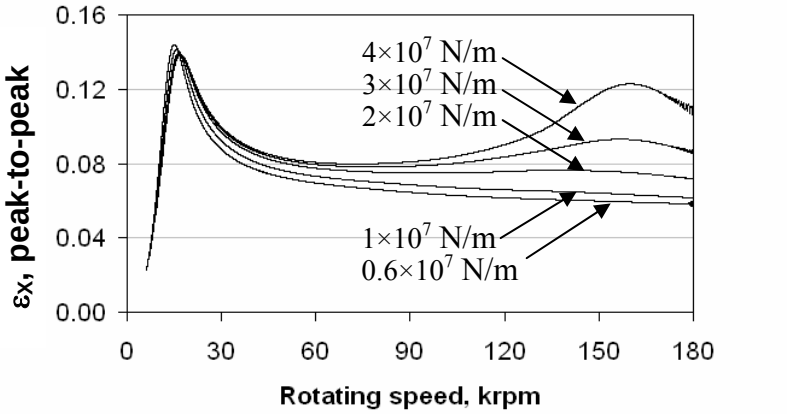

Fig. 3.8 Coast down simulations of peak-to-peak amplitudes of ε_X with respect to pad radial stiffness (C=35μm)

Table 3.3 Critical speeds and damping ratio extracted from Fig. 3.8

Radial stiffness (10^7 N/m)	Critical speed (krpm)	Damping ratio
0.6	14.8	0.44
1.0	15.6	0.46
2.0	16.3	0.52
3.0	16.6	0.55
4.0	16.8	0.56

3.6 Effect of Nominal Clearance to Coast-down Responses

The design parameters such as pivot offset, preload, tilting stiffness, and pad radial stiffness cannot be changed once the bearings have been made. However, the nominal clearance is adjustable in a limited way by coating or grinding the rotor surface. Therefore, a relation between overall bearing performance and nominal clearance is of interest. In general, decreasing the nominal clearance leads to higher critical speeds and onset speed of instability. Simulated coast-down responses for different clearances for pad radial stiffness of 1.0×10^7N/m are presented in Fig. 3.9, where the critical speed and its amplitude increase as the nominal clearance decreases. The nominal clearance of 25μm was too small to accommodate the rotor growth at high-speeds. In case of 40μm, there is a range of instability between 30 krpm and 64 krpm, which can be explained by the parabolic curve of rotor centrifugal growth as explained earlier.

It is interesting to note that unstable bearings with large clearance can be stabilized at high-speeds due to the large rotor centrifugal growth. Not shown in the graphs but similar phenomena was observed for pad radial stiffness of 0.5×10^7 N/m.

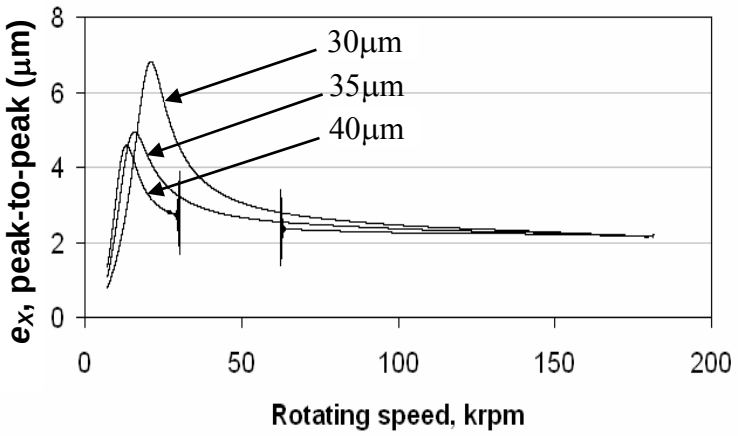

Fig. 3.9 Coast down simulations of peak-to-peak amplitudes of e_X with pad radial stiffness of 1.0×10^7N/m for various nominal clearances

Considering that large bearing clearance can be achieved with smaller pad radial stiffness, a selection of lower limit of possible pad stiffness (from Fig. 3.6) is desirable. Small pad radial stiffness can also eliminate undesirable second critical speeds (explained in Discussion) observed in Fig. 3.7 and Fig. 3.8. Large bearing clearance of 40μm could not be stable at below 100 krpm even if bearing became stabilized again at high-speeds (Fig. 3.7 and Fig. 3.9). Considering these factors in mind, optimum pad radial stiffness and bearing clearance are $1\sim2\times10^7$ N/m and 35μm, respectively, and the maximum achievable speed appears 180krpm for the bearing with diameter in 28.5mm and length in 33.2mm.

3.7 Discussion

From Fig. 3.3 for base line design without pad radial stiffness, bounded sub synchronous vibration initiates at 87krpm and continue to grow until 115krpm. Separate coast down simulation shows the natural frequency with phase angle of 90^o appears at 27krpm, very close to the whirl frequency at 87 krpm, where the sub-synchronous whirl begins to appear. On the other hand, whirl frequency at 115 krpm, where the synchronous whirl begins to diverge, is very close to the critical speed, i.e., 35 krpm. The growth of the bounded orbit is mainly due to the growth of sub-synchronous components. The rotor synchronous vibration is the largest at critical speed. Likewise, the amplitude of sub synchronous vibration keeps increasing as the sub-synchronous speed approaches the rotor critical speed. The large difference between the system natural frequency (speed) and the critical speed implies large bearing damping at the low speed ranges, which is abnormal in gas bearings. Experimental studies in [4] have limited information regarding the high damping at the critical speed and further experimental validation is necessary.

As shown by the parametric studies with pad radial stiffness and bearing clearance, overall bearing stability is very sensitive to the clearance and pad radial stiffness, and the effect of rotor growth should be implemented carefully in the design process of high-speed gas bearings. Another important design aspect is a thermal issue. Most gas bearing designs have been performed assuming isothermal operation regardless of running conditions. These assumptions of isothermal operation of gas bearings rely on the assumption of negligible heat generation or existence of very effective heat

dissipation path to the bearing and/or rotor. However as Eq. (3.9) suggests, under certain conditions, e.g., pure hydrodynamic at very high-speeds with very small bearing clearances, the rotor can experience very large thermal growth. However, an estimation of accurate rotor thermal growth requires knowledge of overall rotor-bearing configurations, i.e., all the heat paths, rotor types (solid or hollow), operating environments, and thermal deformation of all the constituent parts. These parameters depend on the actual system where the gas bearing is applied and considerations of all these aspects are beyond the scope of this paper.

Interesting phenomena are observed for large pad radial stiffnesses from Fig. 3.7 and Fig. 3.8. As pad radial stiffness increases, second critical speeds appear at above 150krpm. At the high-speeds, bearing clearance becomes very small due to the rotor growth, and direct stiffness of gas film is much higher than pad radial stiffness, and equivalent radial stiffness of the total bearing system is determined from the pad radial stiffness. From the rotor mass (0.414 kg) used for orbit simulations, the natural frequency of rotor-pad radial stiffness is 133 krpm ($=\frac{60}{2\pi}\sqrt{\frac{2k_\delta}{m_r}}$) for pad radial stiffness of 4.0×10^7 N/m. Twice the pad radial stiffness is used because of the two pads along either X or Y direction. From highly nonlinear behavior of gas bearing and other factors, such as finite cross-coupled stiffnesses and gas film damping, the second critical speeds appear at around 160krpm. As the pad radial stiffness is decreased, the peak magnitude at the second critical speeds decreases and eventually disappears when pad radial stiffness is below 2×10^7 N/m.

For bearing nominal clearance of 40μm, existence of rotor instability at intermediate speeds (Fig. 3.7 and Fig. 3.9) is quite interesting. Experimental verification with test bearings with relatively large nominal clearance was not successful due to incurring instability and bearing failure before the rotor exits the upper bound of instability.

Due to the simple spring element added to the tilting pads to accommodate the rotor growths, a concern on losing damping capability to any external destabilizing force was raised. Note most gas bearing tests have been demonstrated in an ideal rigid rotor configuration without any destabilizing force, which always exists in actual turbomachinery. These destabilizing forces can come from seals or shroud clearances between impellers and shrouds. Effect of destabilizing forces on the bearing stability is investigated. Equations of rotor motions in matrix form with additional destabilizing forces becomes

$$\begin{bmatrix} m_r & 0 \\ 0 & m_r \end{bmatrix} \begin{bmatrix} \ddot{e}_X \\ \ddot{e}_Y \end{bmatrix} = \begin{bmatrix} F_X \\ F_Y \end{bmatrix} + \begin{bmatrix} m_r u_{im} \omega^2 \cos \omega t + m_r g \\ m_r u_{im} \omega^2 \sin \omega t \end{bmatrix} + \begin{bmatrix} 0 & -k \\ k & 0 \end{bmatrix} \begin{bmatrix} e_X \\ e_Y \end{bmatrix}, \quad (3.9)$$

where k is a cross-coupled stiffness that generates destabilizing forces to the rigid rotor. Typically these destabilizing forces are very small compared to bearing forces because seal clearances or impeller-shroud clearances are much bigger than gas bearing clearances. However, these small destabilizing forces can excite the natural frequency of the rotor-bearing system and can be problematic. Any external cross-coupled damping terms were not included here because damping (if positive) always stabilizes the system.

Cross-coupled stiffnesses were increased from 0 to 10×10^5 N/m at 180 krpm to investigate the rotor stability under various levels of destabilizing forces.

The $\overline{F}_X$ and $\overline{F}_Y$ in Fig. 3.10 show the summations of bearing reaction force and destabilizing force averaged over one cycle along the *X* and *Y* directions, respectively, for different cross-coupled stiffnesses at 180 krpm. Pad radial stiffness and bearing clearance were 1×10^7 N/m and 35μm for the simulations. The zero cross-coupled stiffness simulates ideal test rig conditions without any seal or impeller shroud. The dynamic bearing forces generated by synchronous imbalance are canceled out during the averaging process. While the bearing is stable, the $\overline{F}_X$ and $\overline{F}_Y$ are maintained as the rotor weight (4.06N) and zero, respectively. The dynamic balances are maintained up to the cross-coupled stiffness of about 6×10^5 N/m, above which the balances are broken as indicated by slight slope changes of $\overline{F}_X$ and $\overline{F}_Y$, and initiation of sub synchronous whirl as in Fig. 3.11(b). Full coast down simulations were not attempted because a speed-independent fixed cross-coupled stiffness rendered too large destabilizing forces at near critical speeds, which is not feasible in actual systems. If experimental information on speed-dependent external destabilizing forces is available, more accurate prediction would be possible.

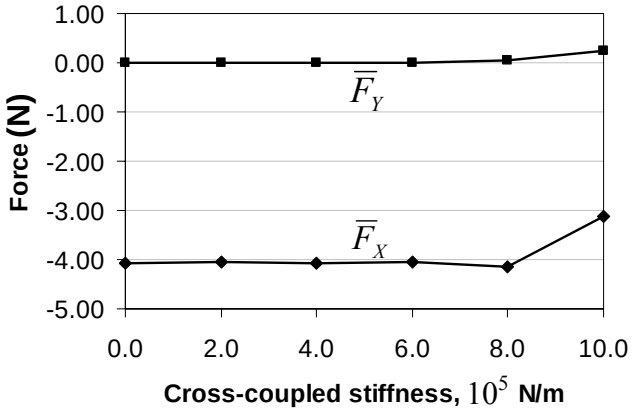

Fig. 3.10 Effect of external destabilizing forces on bearing forces

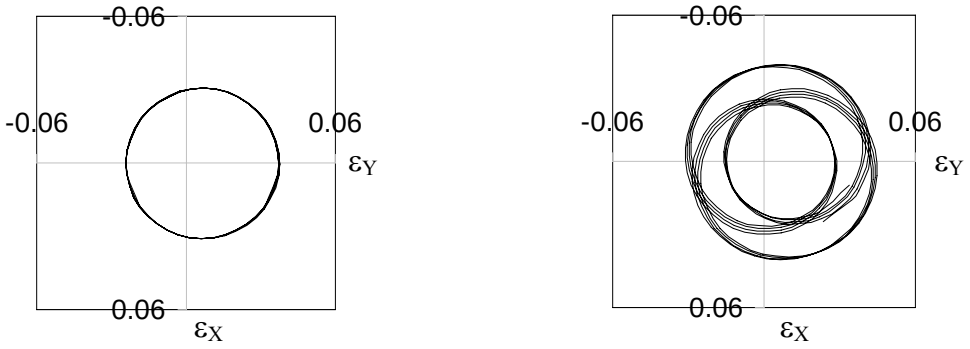

(a) No external destabilizing force (b) Cross-coupled stiffness 8×10^5 N/m

Fig. 3.11 Effect of external destabilizing forces on rotor orbits; cross-coupled stiffness above 8×10^5 N/m initiates sub synchronous whirl

3.8 Conclusion

Parametric studies were performed to understand overall rotor-bearing system characteristics of a flexure pivot tilting pad gas bearing with radial compliance. To fully understand the non-linear characteristics at high-speeds, nonlinear orbit simulations and coast down simulations were used. Higher preload and pivot offset increased both

critical speeds of the rotor-bearing system and onset speeds of instability due to the increased wedge effect. A change of tilting stiffness has little effect on the critical speed but smaller tilting stiffness increased onset speed of instability in a linear fashion reducing the WFR, which implies the change of tilting stiffness affects cross-coupled stiffness rather than direct system stiffness and damping at critical speed. Higher pivot offset increased direct stiffness with a little effect on the direct damping, rendering a higher rotor vibration at higher critical speeds than the baseline design. On the other hands, the larger preload increased both direct stiffness and damping, rendering rotor peak-to-peak vibration at critical speed as similar to baseline design.

Pad radial stiffness and nominal bearing clearance were very important design parameters for high-speed applications due to physically existing rotor centrifugal growth. From the series of parametric studies, the maximum achievable rotor speed was limited by the minimum clearance at pivot calculated from the rotor growth and radial deflection of pads due to the hydrodynamic pressure. Pad radial stiffness also affects rotor instability significantly. Small radial stiffness could accommodate rotor growth more effectively but deteriorated rotor instability. From parametric studies on a bearing with 28.5mm in diameter and 33.2mm in length, optimum pad radial stiffness and bearing clearance are $1\sim2\times10^7$ N/m and 35μm, respectively, and the maximum achievable speed appears 180krpm. The final design with suggested optimum design variables could be also stable under relatively large destabilizing forces.

CHAPTER IV

ROTORDYNAMIC PERFORMANCE OF CFTPBS

4.1 Introduction

In this chapter, coast-down tests for imbalance response and stability of typical rotor-bearing system with a rigid rotor and two CFTPBs are conducted over operating speeds up to 55 krpm. The coast-down responses are investigated through non-linear orbit method and linear perturbation method incorporating XLTRC (a rotordynamic analysis software developed and presented by the Turbomachinery Laboratory at Texas A&M University). The test bearings of CFTPB were designed in the previous studies [3], employing orbit and coast-down simulations for parametric studies of pivot offset, preload, tilting stiffness, and optimal selection of pad radial stiffness and nominal clearance. The manufactured CFTPBs have the upper and lower parts as in Fig. 4.1, and the distance between the parts (called split offset in this research) are increased or decreased for stability control.

For investigation of synchronous rotordynamic responses, XLTRC is used with dynamic force coefficients from the perturbation analysis. XLTRC provides calculations of undamped and damped critical speeds, synchronous rotordynamic response plots, mode shape analyses, transient analyses, e.t.c. of rigid and bending vibration modes for general rotor-bearing systems using defined bearings with synchronous force coefficients over operating speeds (the dynamic force coefficients for each bearing are

calculated by the perturbation analysis, where equilibrium positions of rotor are searched by using the orbit methods [3]). In standard turbomachinery analyses of a typical rotor-bearing system, dynamic properties of each bearing are given through corresponding force coefficients from either perturbation analysis or experimental measurement. The rotor is represented by a structural-dynamic model of a beam with a series of lumped masses, considering bending and shear deflection, transverse and rotation inertia, and gyroscopic effects with free end boundary conditions [1]. Coupled effects of the two bearings are also taken into account, as well as dynamic properties of each bearing. This research follows the convectional turbomachinery methodology for typical rotor-bearing systems with a relatively long shaft and two support fluid bearings: only the force coefficients of translational rotor motion are of importance [34]. In addition, only the rigid vibration mode (conical and cylindrical) are considered because the rotor was designed to have much higher bending critical speeds than operating speeds.

Fig. 4.1 Manufactured compliant flexure pivot tilting pad gas bearing

For stability analyses of general rotor-bearing systems, two different methods are proposed in this paper: generalized orbit simulations and linear stability analyses. For general orbit simulations, an orbit simulation program for general rigid rotor motions with two different bearings is developed. While the orbit simulations in the design studies were performed for only the translational rotor motion assuming two bearings are identical, the general orbit simulation program considers both the translational and angular rotor motions with two different bearings. For the linear stability analyses for conical rotor motion, XLTRC is used to find critical speeds for conical motion, and the perturbation analysis with the Lund method [14] is employed to calculate whirl frequency ratios (WFRs) for cylindrical vibration mode. The relation between WFRs for the conical and cylindrical vibration mode is investigated by the generalized orbit simulations. Predictions of onset speed of instability by the generalized orbit simulations and the linear stability analyses are compared to coast-down tests for stability. Formulations of the perturbation analysis are presented in Appendix A, and details on the generalized orbit simulations are given in [3,8].

Design parameters and rotor and pad motions of CFTPBs are presented in Fig. 3.2. For an arbitrary pad and rotor position, local film thickness is described by Eq. (3.1). The split offset (d), i.e. the distance between the upper and lower parts of bearing in Fig. 4.2, is implemented by adding $0.5d\left|\cos\theta\right|$ to Eq. (3.1). The original symmetric configuration (Fig. 3.2(a)) has zero split offset.

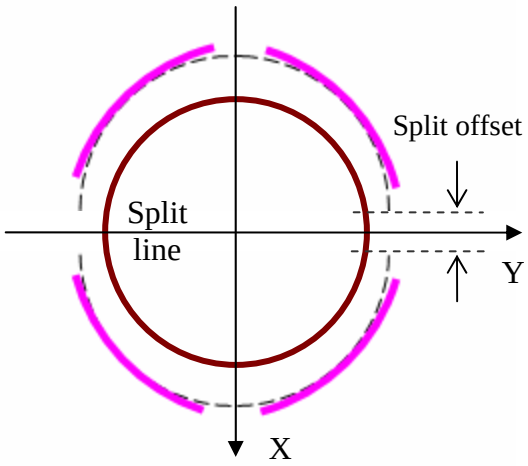

Fig. 4.2 Split offset of CFTPB

4.2 Experimental Facility

4.2.1 Test Bearing

Test bearings were manufactured, based on the optimized design [3]. Test bearings have non-symmetric pad radial stiffnesses: two upper pads (pads 1 and 4) have half the radial stiffness of two lower pads (pads 2 and 3) to accommodate rotor growth effectively with smallest nominal clearance (30 μm). Specific design parameters of the manufactured bearing are given in Table 4.1. Pad mass and moment of inertia were increased to avoid possible deformation of pads due to fluid film pressure (pad deformation would cause a change in preload). The tilting stiffness (i.e. web thickness) was increased to reduce stress level due to tilting motion in pivot web. Furthermore, mass of the machined hollow rotor with wall thickness of 3mm and length of 120mm

was decreased to 0.130 kg for enhanced stability. Nominal clearance is subject to change due to manufacturing uncertainty and wear over time.

Table 4.1 Specifications of manufactured bearing

CFTPB Parameters	SI unit	
Number of pads	4	
Pad mass (m_p)	16×10^{-3}	kg
Pad inertia (i_p)	1×10^{-6}	kg-m^2
Pad start angle	5	degree
Pad arc length	80	degree
Pivot offset	0.7	
Preload (r_p)	15	μm
Tilting stiffness (k_ϕ)	34.3	Nm/rad
Radial stiffness (Upper pads, k_δ)	0.5×10^{7}	N/m
Radial stiffness (Lower pads, k_δ)	1×10^{7}	N/m
Bearing length (L)	33.2	mm
Nominal clearance (C)	30	μm
Rotor mass per bearing (m_r)	0.130	kg
Rotor diameter ($2R$)	28.60	mm
Total rotor length	120	mm
Rotor wall thickness	3	mm

4.2.2 Test Rig Description

A test rig (Fig. 4.3) was constructed with a rotor assembly (Fig. 4.4), two CFTPBs, two bearing housings, and two thrust nozzles. The rotor assembly is composed

of a stainless steel hollow shaft (the length of 120mm, the diameter of 28.60mm and the wall thickness of 3mm, coated with hard Cr on the outer surface) and two impulse turbines. For initial coast-down tests, the test rotor was balanced down to about 150 mg-mm using a balancing machine in the test cell. However, the exact amount and location of the imbalance of the rotor assembly are unknown because of accuracy limitation of the balancing machine. Each bearing housing supporting the CFTPB is equipped with 2 proximity probes (measuring horizontal and vertical displacements), and a tachometer is placed between the two bearing housings. Two thrust air nozzles with 5mm nozzle diameters along the rotor axis act as thrust bearings.

The impulse turbine is assembled at each end of the rotor, as seen in Fig. 4.4, enclosed by a shroud. Four jets of pressurized air are supplied into the shroud, causing a fast, circular flow. The gap between the turbine and the shroud is less than 0.5mm so as to minimize the momentum loss of the pressurized air, and thus maximize the turbine efficiency. The rotor assembly was designed to have relatively high bending critical speeds such that only rigid vibration modes (cylindrical and conical) appear in an operating speed range less than 100 krpm. Using XLTRC, which presents a damped critical speed map where all the critical speeds of vibration modes are calculated with force coefficients over a range of operating speeds, all the bending modes of the current rotor were evaluated to have natural frequencies above 400 krpm, which is far higher than the operating speeds. Therefore, only the rigid modes of rotor motion are taken into account.

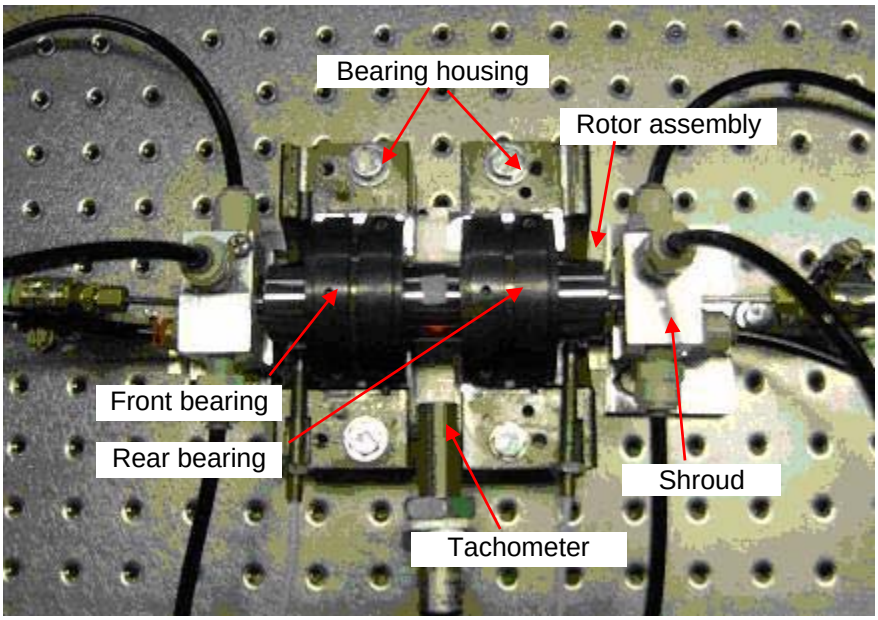

(a) Bearings and Rotor assembly

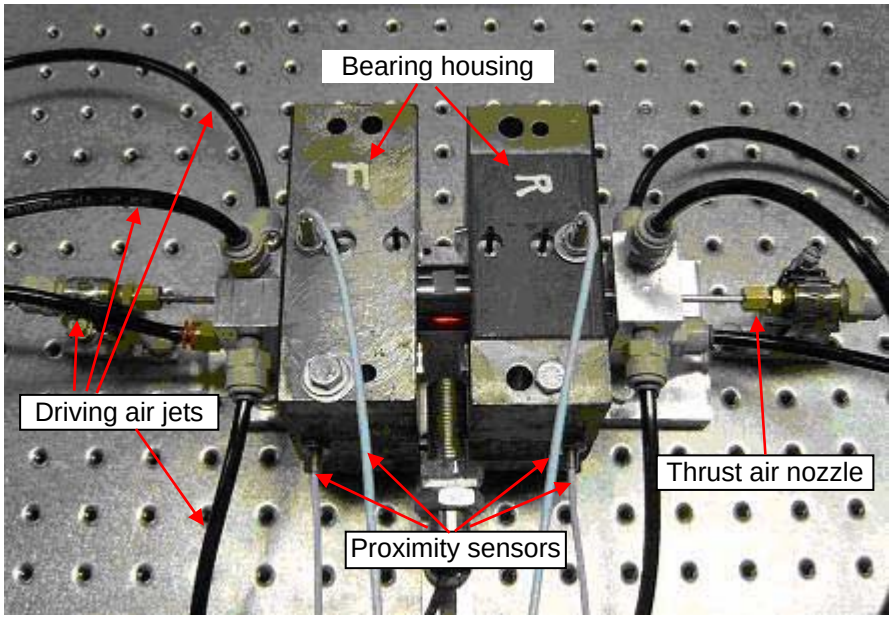

(b) Sensors and air supplies

Fig. 4.3 Test rig

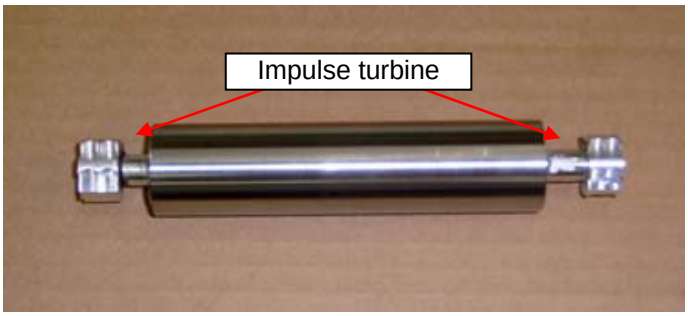

Fig. 4.4 Rotor assembly with the impulse turbine

4.3 Experiment and Prediction for Synchronous Response

Imbalance coast-down tests are performed from 55 kprm with three imbalance modes: a baseline (the residual imbalance after rotor balancing) and two calibrated imbalance configurations (to excite the cylindrical and conical vibration modes, respectively). Sub-synchronous instability did not occur in this speed range. Predictions of synchronous rotordynamic response are made by XLTRC associated with dynamic force coefficients from the perturbation analysis, and then compared to the test results.

4.3.1 Nominal Clearance and Split Offset of Bearing Set I

Nominal clearance of the manufactured bearing-rotor system was determined by simple calculation using preload, rotor diameter, and set bore diameter. In tilting pad bearings, nominal clearance can not be measured directly because of the preload of each pad. Therefore, nominal clearance was calculated by the relation that a nominal clearance equals the preload (15 μm) plus a clearance at pivot (half of the difference between the rotor diameter and the set bore diameter). The measured rotor diameter is 28.60 mm with an uncertainty of 2.0 micrometer (Electro-Coatings, Inc.), which gives a

tolerance of ±1.0 μm to the radial clearance. The set bore diameters of the rear and front bearing are 28.642 and 28.632 mm with an uncertainty of 0.5 micrometer (KMC, Inc.). As a result, the calculated nominal clearances of the rear and front bearings are respectively 36 and 31 μm with a tolerance of ±1.5 μm.

The front bearing with nominal clearance of 36 μm had early instability at less than 40 krpm, which is too low to observe overall synchronous responses over operating speeds (<55 krpm). For imbalance coast-down tests, the vertical distance between the upper and lower parts of the front bearing were decreased by 14 μm by grinding the surface of the lower parts (split line in Fig. 4.2) to increase onset speed of instability above the speed limit of 55 krpm. Nominal clearance and split offset of the rear and front bearings for imbalance coast-down tests (named Bearing Set I) are tabulated in Table 4.2, where the rear bearing have a smaller nominal clearance (31 μm) with zero split offset (symmetric bearing configuration), and the front bearing has a larger nominal clearance (36 μm) with a asymmetrical clearance distribution (split offset of -14 μm). Numerical simulations for synchronous rotordynamic responses, hereafter, are conducted using the nominal clearance and split offset in Table 4.2.

Table 4.2 Nominal clearance and split offset of Bearing Set I for imbalance coast-down tests (tolerance: ±2 μm)

	Nominal clearance	Split offset
Rear bearing	31 μm	0 μm
Front bearing	36 μm	-14 μm

4.3.2 Imbalance Coast-down Test

Coast-down tests were conducted to measure rotor motions for various imbalance conditions: the baseline (residual) imbalance and two calibrated imbalance configurations (in-phase and out-of-phase) to excite the cylindrical and conical rotor vibration modes. The rotor assembly was balanced to have an amount of imbalance less than 150 mg-mm for each bearing at a speed of 1500 rpm with a balancing machine in the laboratory, and the residual imbalance is the baseline imbalance. However, the angular location and axial distribution of the imbalance are unknown, and the actual imbalance can be different because operating speeds are much higher than the balancing speed. For calibrated imbalances, two identical masses (10mg) are located on the rotor surface at both ends of rotor with angular orientations of 0 and 180° to excite the cylindrical and conical vibration modes, respectively. Dominant imbalance masses over the residual imbalance (to identify pure conical and cylindrical responses) could not be applied because the baseline response amplitude reached up to two-thirds of clearance at pivot. The cylindrical imbalance masses are aligned to the tachometer optical tape.

Coast-down responses in the vertical and horizontal directions at the rear bearing measured from 55 krpm for the baseline, in-phase and out-of-phase imbalance mass configurations are presented in Fig. 4.5, Fig. 4.6 and Fig. 4.7, respectively. All the vertical responses have critical speeds around 33 krpm. On the other hand, the horizontal responses show slightly different rotordynamic behavior: critical speeds for the baseline and the out-of-phase imbalance masses are about 31 krpm (Fig. 4.5 and Fig. 4.7), and particularly for the in-phase imbalance masses, separation of the critical speed occurs

from 31 krpm to 28 and 41 krpm (Fig. 4.6). Even the vertical response shows slight excitation around 41 krpm. The vertical responses at the front bearing have double peaks for all the imbalance modes as in Fig. 4.8(b). Investigation of measured time responses at the front and rear bearings showed that the rotor motions over the operating speeds for all the imbalance modes are subject to the conical vibration mode with the forward precession (the rotor spin direction). Major critical speeds of the imbalance coast-down responses are approximated by calculating the major amplitude[1] ($\sqrt{(e_H{}^2 + e_V{}^2)/2}$, where e_H and e_V are the amplitudes of the horizontal and vertical responses in Fig. 4.5, Fig. 4.6, and Fig. 4.7). The major amplitudes are presented in Fig. 4.9, where the major critical speeds for all the imbalance modes are about 32 krpm. Even though the in-phase imbalance masses caused a separation of critical speed in the horizontal response, the major critical speed change is very small (<5%).

At about 2 krpm (touch-down speed), the peak-to-peak amplitudes in the vertical responses for all the imbalance mode are less than 4μm, as presented in Fig. 4.8(a). Taken into account the high reduction rate of the amplitudes at the touch-down speed, the amplitudes are expected to be much decreased at zero rotor speed and approach to less than 2μm. Therefore, ratio of run-out amplitudes to peak amplitudes is less than 10%. Even if the amplitude at the touch-down speed is considered, the ratio is less than

[1] Under the limitation that the measured coast-down responses provide only the horizontal and vertical amplitudes without information on the shape and orientation of an orbit, the exact maximum amplitude of the orbit cannot be calculated. However, an approximate outline encompassing both the horizontal and vertical amplitudes can be obtained by root mean square of the horizontal and vertical responses.

20%. Moreover, the peaks are sharp and run-out is continuous with limit, so that the variation of the critical speed due to run-out is expected to be minimal.

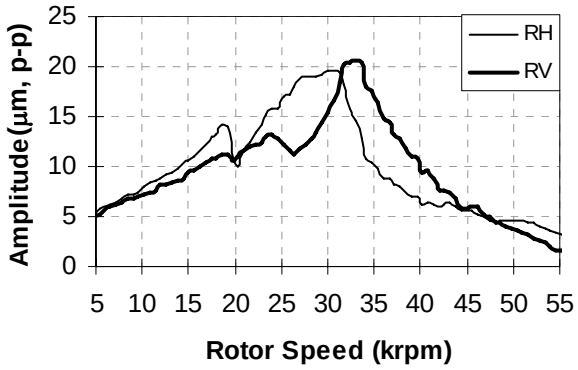

Fig. 4.5 Coast-down responses for the baseline at the rear bearing; RH and RV denote the horizontal and vertical response at the rear bearing, respectively.

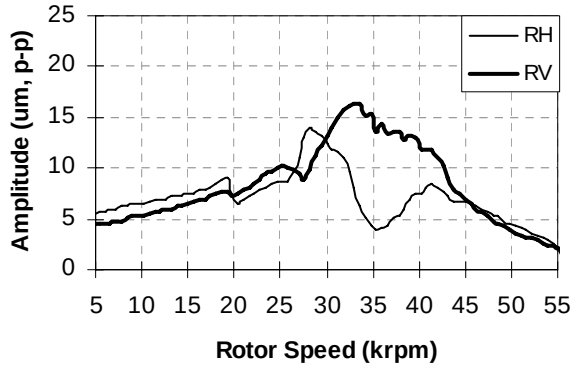

Fig. 4.6 Coast-down responses for in-phase imbalance masses at the rear bearing

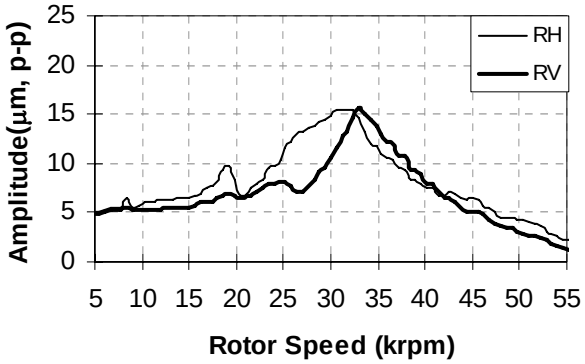

Fig. 4.7 Coast-down responses for out-of-phase imbalance masses at the rear bearing

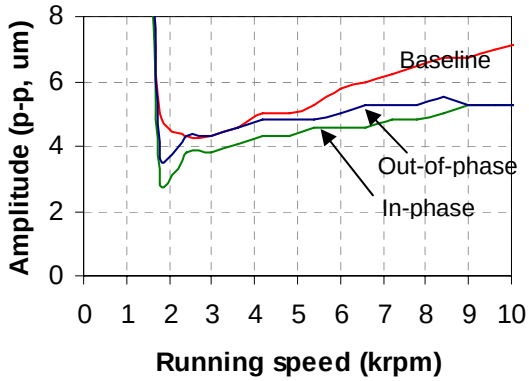

(a) Magnified view of coast-down responses at the rear bearing

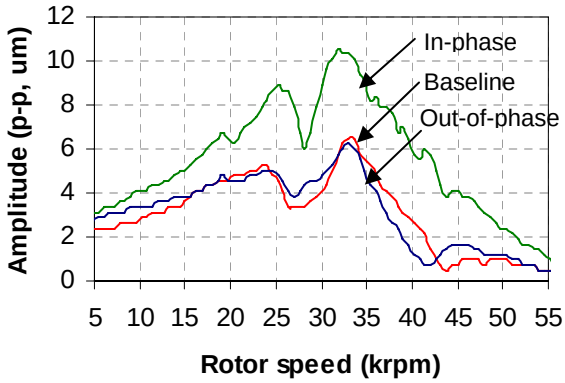

(b) coast-down responses at the front bearing

Fig. 4.8 Coast-down responses in the vertical direction at the rear and front bearing

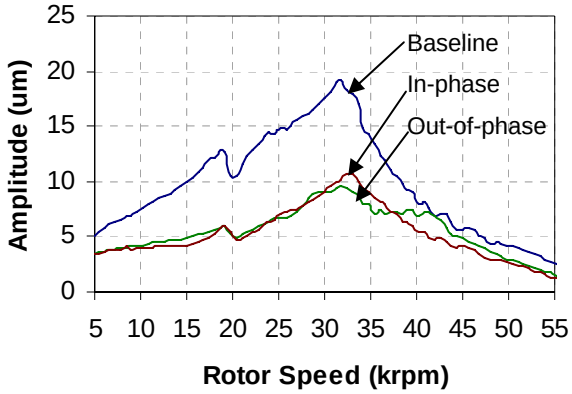

Fig. 4.9 Major amplitude responses at the rear bearing

4.3.3 Prediction of Synchronous Response

Effects of imbalance mass and stiffness orthotropy on synchronous responses are investigated for each bearing separately by using XLTRC, because combined responses of Bearing Set I are so complicate that the effects are difficult to be identified. The stiffness orthotropy is caused by the unsymmetrical clearance at the front bearing. Assuming both bearings for XLTRC simulations are identical, synchronous rotordynamic simulations are performed for two cases (Table 4.3): Case 1 is for the rear bearing configuration (nominal clearance of 31 μm), and Case 2 is for the front bearing configuration (nominal clearance of 36 μm and split offset of -14 μm). Simulated imbalance modes are out-of-phase (180^o), mixed (90^o), and in-phase (0^o) to excite conical, cylindrical and mixed rotor vibration mode, respectively. Each bearing is defined by dynamic force coefficients calculated from the perturbation analysis.

From the XLTRC simulations for Case 1 and 2, in-phase imbalance masses showed a tendency to raise critical speeds for both the cases, and the double peaks in the

experiment (Fig. 4.6) appeared to result from the in-phase imbalance component. For Case 1 with the rear bearing configuration, observation of critical speeds for the various imbalance modes reveals the dependence of critical speed on imbalance mode (Fig. 4.10). The critical speed for the out-of-phase imbalance mode, i.e. critical speed for the conical vibration mode, is about 31 krpm, which is smaller than the critical speed of 39 krpm for the in-phase imbalance mode. Furthermore, for the mixed imbalance mode, double peaks, i.e. separation of critical speed, is observed at 27 and 44 krpm. This phenomenon is also observed in the experiments where double peaks occurred only when the in-phase imbalance masses were applied. As a result, the separation of critical speed is found to result from the in-phase imbalance component. For Case 2 with the front bearing configuration (stiffness orthotropy), double peaks are observed for all the imbalance modes only in the vertical responses (Fig. 4.11, Fig. 4.12, and Fig. 4.13), which were also observed in the experiment (Fig. 4.8). The simulated major critical speeds for conical vibration mode are 35 krpm for Case 1 and 31 krpm for Case 2, which shows a favorable agreement to the measured major critical speeds of 32 krpm (recall that the measured coast-down responses are in the conical vibration mode). Summary of the critical speeds for Case 1 and 2 are presented in Table 4.4.

Table 4.3 Two cases for XLTRC simulations for rotordynamic analyses of Bearing Set I (imbalance quantity per mass is 150mg-mm)

	Bearing type	Bearing configuration
Case 1	The rear bearing configuration	C = 31 μm, d = 0 μm
Case 2	The front bearing configuration	C = 36 μm, d = -14 μm

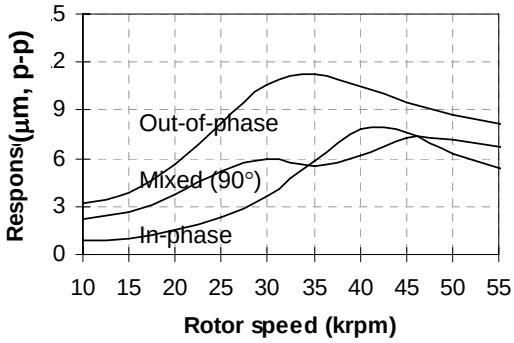

Fig. 4.10 Rotordynamic response from XLTRC for Case 1; the major, vertical and horizontal responses are identical for each imbalance mode.

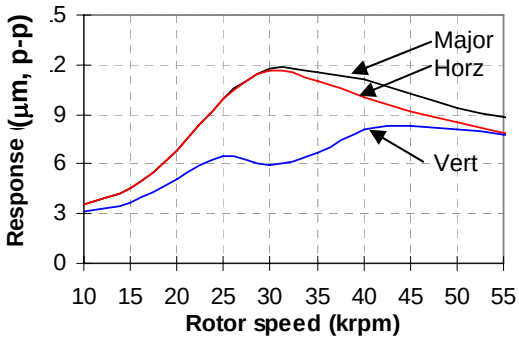

Fig. 4.11 Rotordynamic response for the out-of-phase imbalance mode for Case 2 from XLTRC

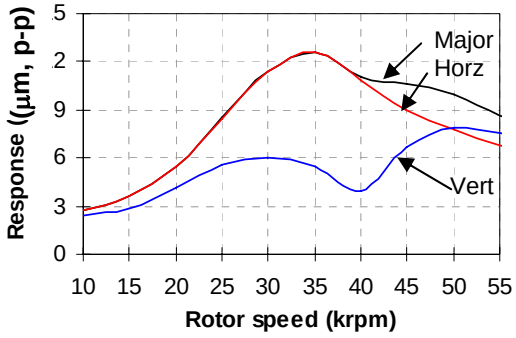

Fig. 4.12 Rotordynamic response for the mixed imbalance mode (90°) for Case 2 from XLTRC

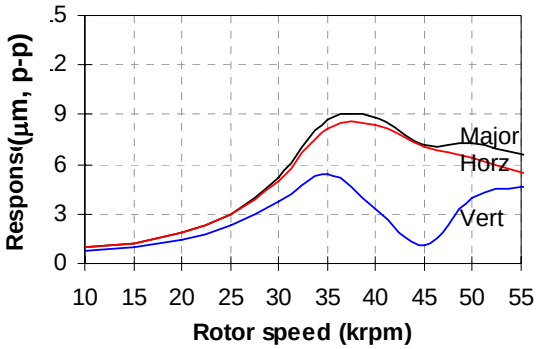

Fig. 4.13 Rotordynamic response for the in-phase imbalance mode for Case 2 from XLTRC

Table 4.4 Critical speeds in the rotordynamic response prediction for Case 1 and 2 (unit: krpm); for Case 1, major, vertical and horizontal critical speeds are identical.

	Imbalance mode	Critical speed				
		Major		Vertical		Horizontal
Case 1	Out-of-phase	34		-		-
	Mixed (90°)	30	47			
	In-phase	41				
Case 2	Out-of-phase	31		26	43	31
	Mixed (90°)	35		30	50	35
	In-phase	37		35	55	37

4.4 Experimental Studies on Onset Speed of Instability

The rotor-bearing configuration (Bearing Set I) is stable up to 55 krpm. To excite instability within the speed limit, the vertical clearances of both bearings were increased by inserting a 10 μm thick shim at the bearing split line in Fig. 4.2. Nominal clearances and split offsets for the rear and front bearings are given in Table 4.5, and named

Bearing Set II for stability coast-down tests. Predictions of onset speed of instability are made by two methods of the orbit simulation and the perturbation method, and the results are compared to the experimental tests. The orbit simulation program for general rotor motion with two different bearings was developed to deal with the conical vibration mode. Predictions by the perturbation method are performed by calculating conical critical speed by XLTRC and WFR for cylindrical vibration mode by the Lund method. From the generalized orbit simulations, the WFR for cylindrical rotor motion turned out to be virtually identical to that for conical motion (details are given in the following section of prediction of instability by orbit method).

Table 4.5 Nominal clearance and split offset of Bearing Set II for stability coast-down tests (tolerance: ±2 μm)

	Nominal clearance	Split offset
Rear bearing	31 μm	10 μm
Front bearing	36 μm	-4 μm

4.4.1 Stability Coast-down Test

Coast-down tests for the baseline imbalance mode are performed with the split offset of the rear and front bearings of Bearing Set I increased by 10 μm. Overall rotor motions are in the conical mode with forward precession. Two whirl motions are initiated at about 49 krpm with whirl speeds of 17 and 32 krpm (Fig. 4.14) with WFRs of 0.35 and 0.65 (Table 4.6), and their amplitudes increase rapidly thereafter as the running speed increases (Fig. 4.15). The rear bearing increased vertically by 10 μm is considered

as the normal-loose model which has characteristics of a fractional frequency phenomenon due to non-symmetrical clearance and a widening range of unstable speeds centered about WFR of 0.5 by increases of radial stiffness differences. The two WFRs show the fractional frequency phenomenon of 1/3 and 2/3 of the rotor speed (situated around 0.5 with a difference of 0.15). The amplitude of the 2nd whirl motion is approximately two times that of the 1st whirl motion, and thus, the 2nd whirl is estimated to be more harmful. A waterfall plot of the vertical response at the rear bearing is shown in Fig. 4.16, where overall behavior of the 1st and 2nd whirls and the synchronous motion are presented with their amplitudes. The 1x motion corresponds to the synchronous motion in Fig. 4.16; the two vibration components around 0.5X correspond to the WFRs of 0.35 and 0.65 in Fig. 4.14. The two whirl motions are observed to have been initiated at 49.2 krpm and to grow exponentially, as in Fig. 4.15. A 2X vibration component is observed in the waterfall plot, which has limited amplitudes and eventually disappears at high speeds.

Table 4.6 Two whirling motions and their amplitude and whirl frequency ratio (units of speed: krpm and amplitude: μm)

Running speed	Whirl 1			Whirl 2			Synch Amp
	Speed	Amp	WFR	speed	Amp	WFR	
49.2	17.4	0.72	0.35	31.8	1.20	0.65	2.64
51.0	19.2	0.96	0.38	33	1.92	0.65	2.40
53.4	19.8	1.68	0.37	34.2	4.10	0.64	1.68
55.2	20.4	2.88	0.37	35.4	5.52	0.64	1.20

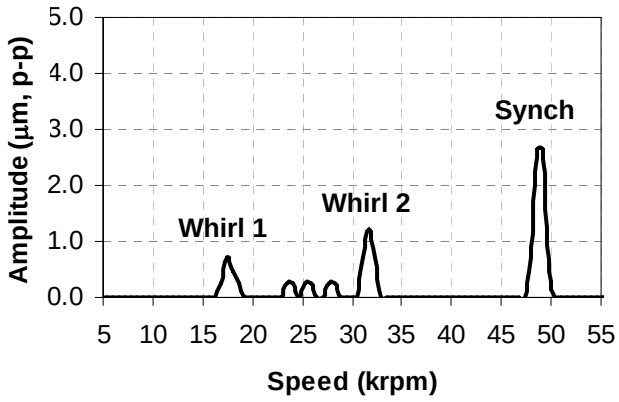

Fig. 4.14 Initiation of the 1st and 2nd whirl motions at 49.2 krpm (from FFT)

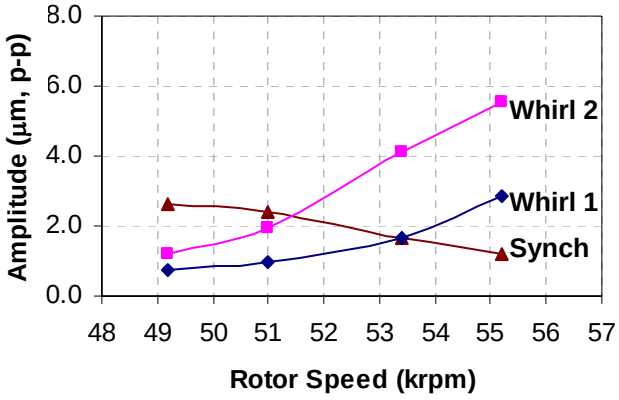

Fig. 4.15 Amplitude of synchronous and whirl motions

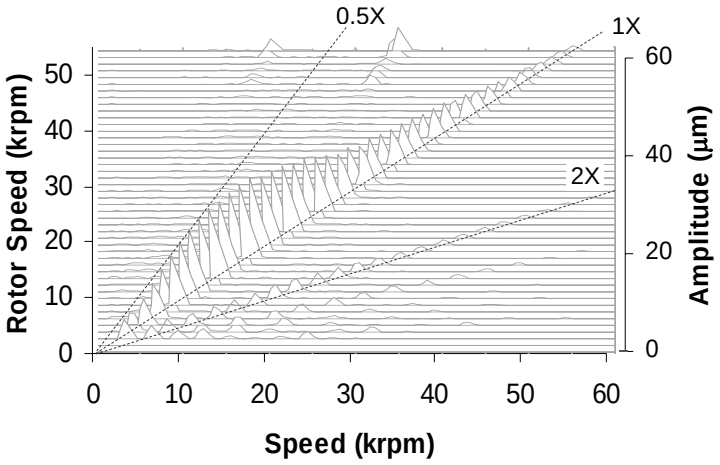

Fig. 4.16 Waterfall plot of vertical coast-down response for the baseline imbalance mode at the rear bearing (speed in the label corresponds to frequency in FFT)

4.4.2 Prediction of Instability by Orbit Method

Orbit simulations for general rigid rotor motions with two different bearings were performed to find onset speeds of instability and corresponding whirl speeds for Bearing Set II. In conventional orbit methods [3,8], the path of the journal center is evaluated by solving dynamic equations of rotor and pad motions and unsteady Reynolds Equation simultaneously, assuming cylindrical vibration mode, i.e. translational rotor motion. However, for stability analyses of the current rotor-bearing system (Bearing Set II) which has the conical rotor vibration mode and two different bearings, solution to the angular motion of rotor is required as well as the translational motion. While the cylindrical vibration mode for symmetric rotor-bearing systems can be evaluated assuming half the rotor mass and one of the bearings, the conical rotor motion with two different bearings requires concurrent calculation of film pressure at each bearing separately. Pad radial and tilting motions are calculated with corresponding bearing

reaction force at each bearing, and rotor motions are updated with net force and moment induced by the two bearing reaction forces and the rotor imbalance force and weight. Dynamic equations of the translational and angular rotor motion of rotor are presented in [8], and detailed numerical solution procedures for orbit simulations are presented in [3] including those for pad radial and tilting motions.

From the generalized orbit simulations, unstable rotor motions for the conical vibration mode were estimated to initiate at 39 kprm with whirl speed of 24.5kprm (WFR 0.63), as in Fig. 4.17. Rotor orbits at the initiation of instability at the rear bearing are presented in Fig. 4.18, where a vertically long elliptical orbit occurred due to the split offset of 10 μm at the rear bearing. On the other hand, horizontally long elliptical orbits are observed at the front bearing (Fig. 4.19) which has the negative split offset of -4 μm. For the cylindrical vibration mode, initiation of instability occurred at 41 krpm (Fig. 4.20) with whirl speed of 26 krpm and WFR of 0.63. The onset speed of instability is slightly higher than that for the conical mode by 2 krpm; however, the WFR for the cylindrical vibration mode at the onset of instability is virtually identical to that for the conical vibration mode (this finding will be employed in prediction of onset speed of instability by the perturbation method). As a result, the estimated whirl speed of 24.5 krpm for the conical vibration mode is very close to the average whirl speed of 25 krpm in the tests (Fig. 4.14). On the other hand, the estimated onset speed of instability of 39 krpm is less than the measured instability speed of 49 krpm by 10 krpm. The predicted and measured instabilities are tabulated in Table 4.8.

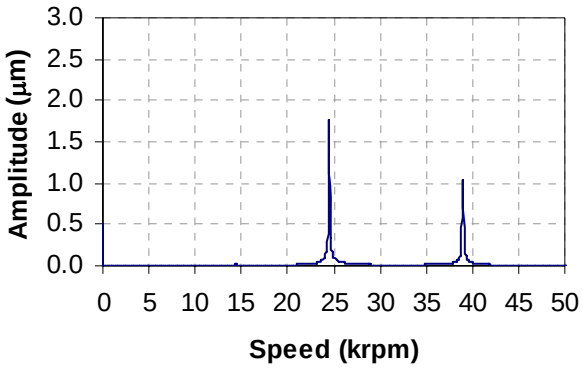

Fig. 4.17 FFT result of simulated vertical response at the rear bearing at 39 krpm for conical vibration mode

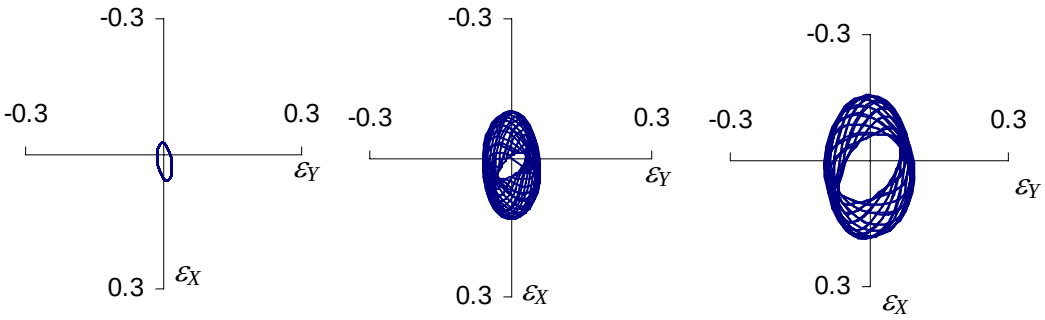

(a) 38 krpm (b) 39 krpm (c) 40 krpm

Fig. 4.18 Orbit of rotor center at the initiation of instability at the rear bearing; normalized by the nominal clearance of 31 μm

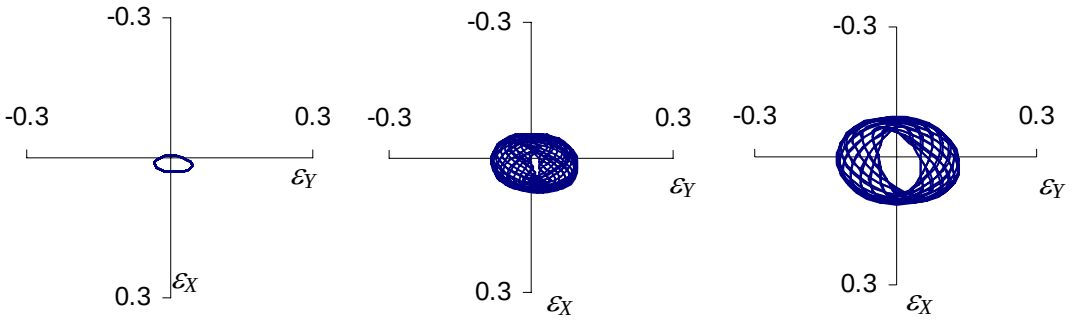

(a) 38 krpm (b) 39 krpm (c) 40 krpm

Fig. 4.19 Orbit of rotor center at the initiation of instability at the front bearing; normalized by the nominal clearance of 36 μm

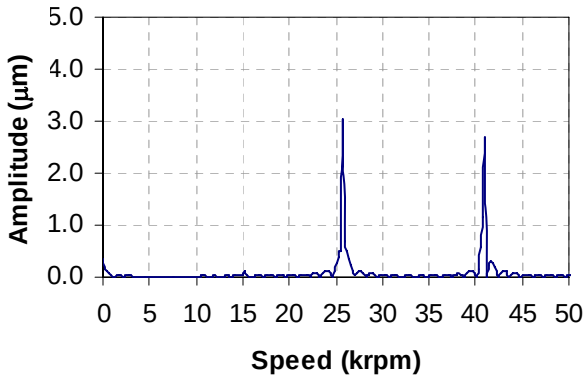

Fig. 4.20 FFT result of simulated vertical response at the rear bearing at 41 krpm for cylindrical vibration mode

4.4.3 Prediction of Instability by Perturbation Method

Onset speeds of instability for Bearing Set II in Table 4.5 are also estimated by combination of critical speeds from XLTRC and WFRs from linear stability analyses, assuming whirl motions at onset of instability take place at system critical speed. Linear stability analyses are not directly applicable to the current rotor-bearing system because

of the rotor vibration mode difference: the dominant rotor vibration mode was conical from the tests, but the perturbation analysis assumes cylindrical vibration mode. Critical speeds for the conical vibration mode are estimated by XLTRC[2] with force coefficients from the perturbation analysis for each bearing configuration (Table 4.7, where both bearings of each case are assumed identical). WFRs for the cylindrical vibration mode are calculated from the perturbation analysis based on the Lund method [15], where at a given rotor speed a whirl speed with zero modal damping is searched by iterations with non-synchronous force coefficients at the whirl speed, and then, a critical mass is calculated with the whirl speed and corresponding modal stiffness. System stability is judged by the critical mass, which is a maximum rotor mass for stable operations: at a given rotor speed, a rotor-bearing system is considered as unstable when the rotor mass is larger than the critical mass (details on the formulation is given in Appendix). Based on the orbit simulation result, i.e. WFRs for the cylindrical and conical vibration modes are virtually identical, onset speeds of instability for conical vibration mode are determined by the critical speeds divided by the WFRs. The critical speeds and WFRs are calculated for each bearing separately, and the lower one is considered to approximate onset speed of instability of the rotor-bearing system.

4.4.3.1 Force Coefficients and Critical Speed

Synchronous force coefficients were calculated for the rear and front bearing of Bearing Set II, and presented in Fig. 4.21 and Fig. 4.22. The synchronous force

[2] XLTRC provides functions of calculating synchronous rotordynamic responses for any imbalance configurations using dynamic force coefficients from the perturbation analysis.

coefficients for the rear bearing in Fig. 4.21 show strong asymmetry of direct force coefficients, i.e. the direct stiffness and damping coefficients in the vertical direction (k_{xx} and d_{xx}) are smaller than those in the horizontal direction due to the split offset of 10 μm. The general trend of cross-coupled stiffness shows an increase as speed increases, especially after 40 krpm. Synchronous force coefficients (Fig. 4.22) for the front bearing of Bearing Set II have the similar level of values to those for the rear bearing, but the asymmetry of the force coefficients (difference between k_{XX}/d_{XX} and k_{YY}/d_{YY}) is less due to the smaller split offset of -4 μm. The vertical direct stiffness and damping coefficients are higher than the horizontal coefficients due to the negative split offset, opposite to the rear bearing. The calculated synchronous force coefficients are fed into XLTRC for rotordynamic analyses to find critical speeds for conical vibration mode.

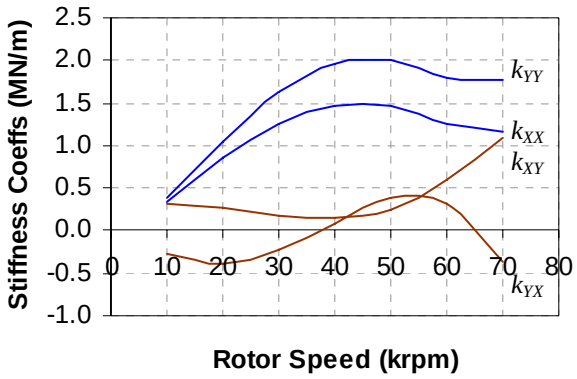

(a) Stiffness coefficients

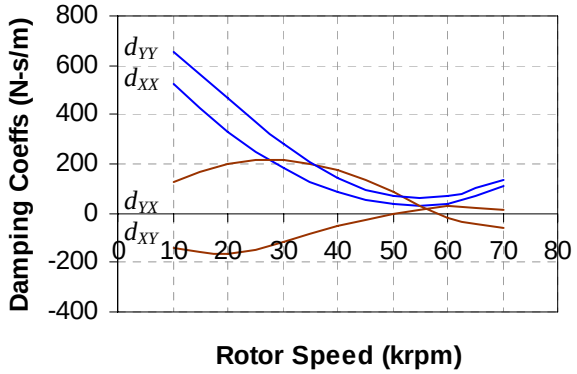

(b) Damping coefficients

Fig. 4.21 Synchronous force coefficients for the rear bearing of Bearing Set II (MN/m: 10^6N/m)

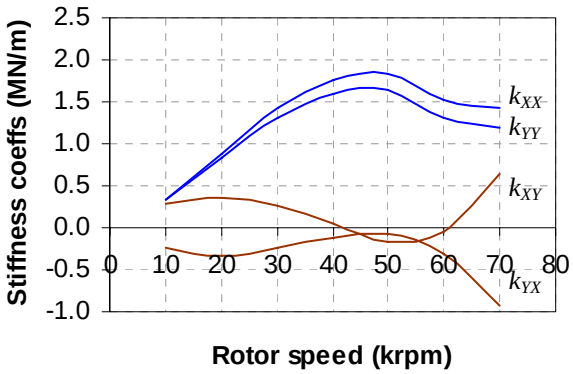

(a) Stiffness coefficients

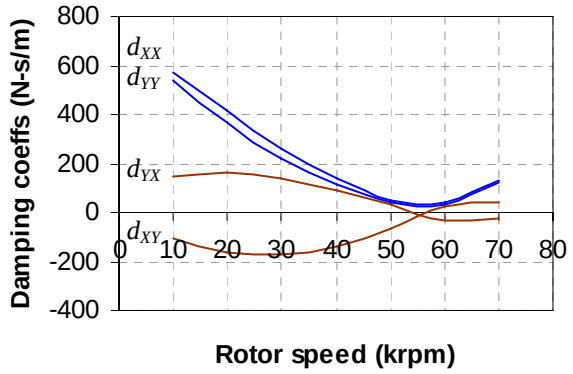

(b) Damping coefficients

Fig. 4.22 Synchronous force coefficients for the front bearing of Bearing Set II

Critical speeds of Bearing Set II for conical vibration mode were estimated by using XLTRC and the force coefficients above for each bearing configuration. Both bearings are assumed identical in each case of Table 4.7: Case 3 is for the rear bearing configuration (nominal clearance of 31 μm and split offset of 10 μm), and Case 4 is for the front bearing configuration (nominal clearance of 36 μm and split offset of -4 μm). From rotordynamic analyses with XLTRC, the major critical speeds for Case 3 and 4 are observed to be about 26 and 27 krpm (Fig. 4.23 and Fig. 4.24, respectively). For Case 3

with the rear bearing configuration, the vertical amplitude is larger than the other due to the positive split offset, and Case 4 shows the opposite due to the negative split offset. The major critical speeds of 26 and 27 krpm are close to the averaged whirl speed of 25 krpm (two whirl speeds from the tests were 18 and 32 krpm in Fig. 4.14). The estimated critical speeds for conical vibration mode are divided by WFRs from the following linear stability analyses to find onset speed of instability for each bearing.

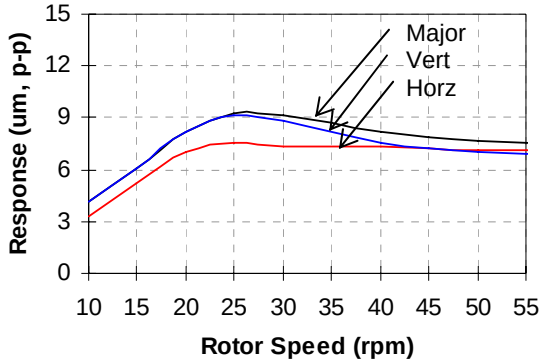

Fig. 4.23 Rotordynamic response for Case 3 for the conical vibration mode from XLTRC

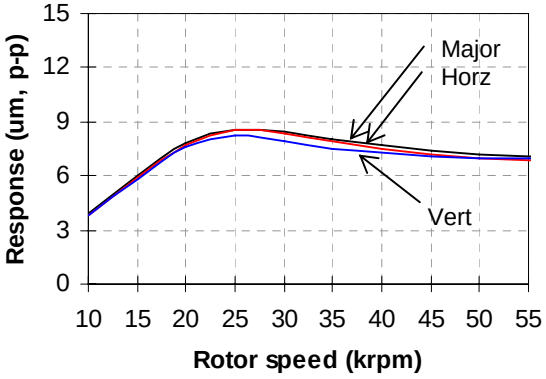

Fig. 4.24 Rotordynamic response for Case 4 for the conical vibration mode from XLTRC

Table 4.7 Two cases for XLTRC simulations for critical speeds of Bearing Set II (imbalance quantity per mass is 150mg-mm)

	Bearing type	Bearing configuration
Case 3	The rear bearing configuration	C = 31 μm, d = 10 μm
Case 4	The front bearing configuration	C = 36 μm, d = -4 μm

4.4.3.2 Whirl Frequency Ratio (WFR)

WFRs at onset of instability for each bearing of Bearing Set II were calculated based on the Lund method [15]. As presented in Fig. 4.25 and Fig. 4.26, unstable rotor motions for the rear bearing were estimated to initiate with WFR of 0.57, and for the front bearing, critical mass did not go below the rotor mass line, i.e. stable for entire speeds. Based on the orbit simulation finding that WFRs at onset of instability for the conical and cylindrical vibration modes were virtually identical in the current system, onset speed of instability for the rear bearing are estimated to be 46 krpm with the major critical speeds of 26 krpm and corresponding WFRs of 0.57. The estimated onset speed of instability for the rear bearing is approximated to be system onset speed of instability. Summary on the predicted instability is presented in Table 4.8.

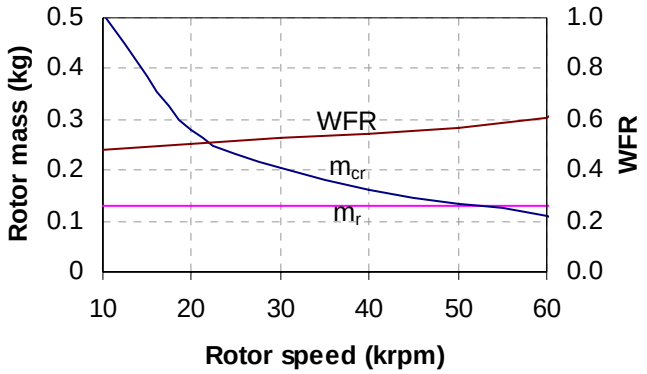

Fig. 4.25 Critical mass and WFR for the rear bearing of Bearing Set II

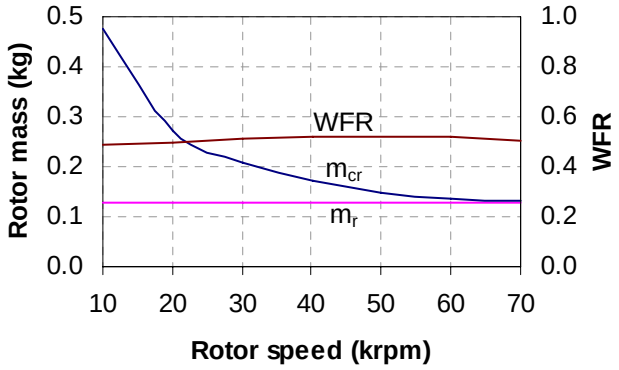

Fig. 4.26 Critical mass and WFR for the front bearing of Bearing Set II

Table 4.8 Onset speed of instability, whirl speed and WFR of prediction and measurement

	Onset speed of instability (krpm)	Whirl speed (krpm)	WFR
Orbit simulation	39	24.5	0.63
Perturbation analysis	46	26	0.57
Coast-down test	49	25 (18/32)	0.51

4.5 Discussion

4.5.1 Prediction of Instability by XLTRC

Stability analyses were also performed by using an inherent stability analysis function of XLTRC with synchronous force coefficients of Bearing Set II (Fig. 4.21 and Fig. 4.22), where a negative damping ratio indicates onset of instability. XLTRC has shown good estimations of instability for oil-lubricated fluid bearings; however, for air-lubricated bearings, XLTRC has a limitation since non-synchronous force coefficients at sub-synchronous whirl speeds are different from the synchronous force coefficients due to air compressibility. The rotordynamic stability map from XLTRC (Fig. 4.27) indicates that onset of instability occurs at 63.5 and 64 krpm for the forward conical vibration mode and forward cylindrical mode, respectively, and corresponding natural frequencies are about 28 and 33 krpm, respectively. The other two curves correspond to the backward conical and cylindrical vibration mode, as indicated in Fig. 4.27(b). Taking into account the measured vibration is in the forward conical mode, onset of instability is predicted to occur at about 63.5 krpm with whirl speed of 28krpm, which shows overestimation of onset speed of instability because XLTRC makes use of synchronous force coefficients instead of non-synchronous force coefficients at whirl speeds. Therefore, the generalized orbit simulation or the linear stability analysis are recommended for conservative design of rotor-bearing systems with air-lubricated CFTPBs,

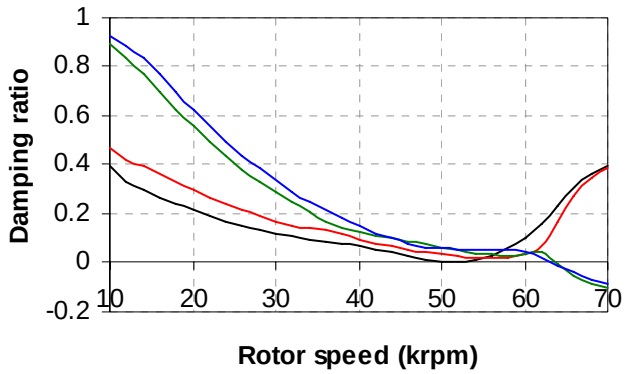

(a) Damping ratio over speeds

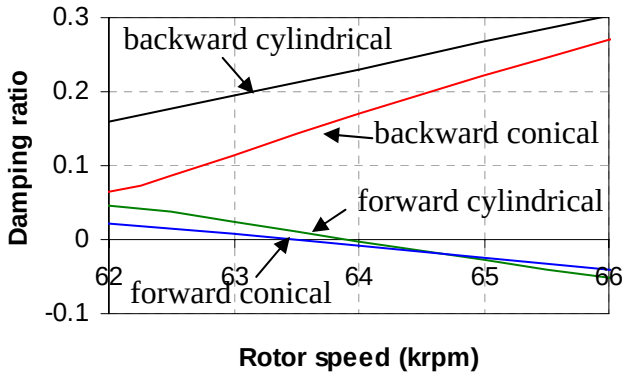

(b) Magnified damping ratio for instability

Fig. 4.27 Rotordynamic stability map for Bearing Set II from XLTRC

4.6 Conclusions

Imbalance coast-down response tests were performed for a rotor-bearing system with CFTPBs with different nominal clearance and split offset (Bearing Set I) over rotor speeds less than 55 krpm. Overall rotor vibrations for all the imbalance modes are subjected to the conical vibration mode with the forward precession, and their major critical speeds are about 32 krpm. Double peaks occurred for the in-phase imbalance

mode. Rotordynamic performance of the rotor-bearing system was investigated by using XLTRC in terms of critical speeds in the conical, cylindrical, and mixed rotor vibration modes. Each bearing in XLTRC was defined by synchronous force coefficients, which were calculated by the perturbation analysis considering rotor centrifugal growth. The predicted critical speeds for conical vibration mode were 31 and 34 krpm for the rear and front bearing, respectively, and showed a favorable agreement to the measurement. The double peaks in the coast-down test for in-phase imbalance masses were evaluated to result from the cylindrical imbalance component of the rotor.

Stability coast-down tests were conducted with the vertical distance between the upper and lower parts of the bearings increased (Bearing Set II), in order for onset speed of instability to be placed in the operating speeds. Predictions of onset speed of instability and whirl speed were made by the generalized orbit simulation and the linear stability analysis based on the Lund method. In coast-down tests for stability, sub-synchronous instabilities were initiated at about 49 krpm with whirl speeds of 18 and 32 krpm (WFRs of 0.35 and 0.65, respectively). From the orbit simulations, onset speeds of instability were estimated to occur at 39 krpm with whirl speeds of 24.5 krpm. From the linear stability analyses with XLTRC and the perturbation analysis, the predicted onset speed of instability was 46 krpm with the critical speed of 26 krpm (WFR 0.57). On the whole, predictions of whirl speed by the generalized orbit simulations and the linear stability analyses showed good agreement to the averaged whirl speed of 25 krpm from the test. However, the estimated onset speed of instability appeared lower than the measured instability.

CHAPTER V

THERMO-HYDRODYNAMIC ANALYSIS OF CFTPBS

5.1 Introduction

For successful implementation of the tilting pad gas bearings to oil-free microturbomachinery, a compliant structure similar to foil bearings should be employed to accommodate the large rotor centrifugal and thermal growth. One approach to avoid the accumulation of manufacturing tolerances and to provide radial compliance is a flexure pivot tilting pad bearings introduced by [6]. Analytical design studies were performed in Chapter III, using orbit simulations, on compliant flexure pivot tilting pad gas bearings (CFTPBs). Each pad has a radial compliant beam structure behind the pad to accommodate any rotor growth in the radial direction.

Due to tight bearing clearance at the pivot, a small change of rotor diameter can cause large change of bearing preload (to be explained later) and performance characteristics. Estimation of the rotor centrifugal growth is well-established from elasticity theory. However, the thermal growth of the rotor has been neglected in most cases, and isothermal analyses have been adopted as a standard numerical method to predict performance of gas-lubricated bearings. However, for higher operating speeds and better understanding of effects of heat generation in the film on the overall bearing characteristics, detailed thermal analyses of gas film and surrounding rotor and bearing

surfaces becomes necessary. Furthermore, thermal stability of the rotor-bearing system should be ensured as well as the rotordynamic stability.

In this chapter, a new computational method for the thermo-hydrodynamic (THD) analysis of rotor-bearing systems with air-lubricated CFTPBs is presented. The developed method is applicable to any rotor-bearing sub-system with various global thermal boundary conditions at the bearing housing and rotor ends away from the bearing. The thermal model of the rotor-bearing sub-system is composed of the rotor (inside and outside the bearing), bearing (pad and bearing shell), and air film in the bearing clearance. The air film temperature is calculated by solving the generalized Reynolds equation and 3-D energy equation. The associated thermal boundary conditions of the air film such as inlet flow temperature at the pad leading edges, rotor surface temperature inside the bearing, and pad temperatures are calculated through iterative evaluation of heat balances at these boundaries. Only global thermal boundary conditions at the rotor away from the bearing and bearing housing are input parameters.

Based on the calculated temperature fields from the THD analyses, the perturbation analysis was performed to calculate dynamic force coefficients of the bearing considering air film temperature and rotor growth (thermal and centrifugal). Parametric studies on several design parameters are presented and compared with isothermal solutions.

5.2 Formulation

General thermal analyses require full understanding of all the heat paths around the rotor-bearing system. This paper focuses on developing a thermal analysis program of a sub-system with the bearing and rotor considering all the heat transfer within the sub-system, given global thermal boundary conditions at the interfaces between the sub-system and surroundings.

The newly-developed THD model was applied to the imbalance test rig developed for experimental studies on rotordynamic performance in Chapter IV, where the test rig was constructed with a rotor assembly, two CFTPBs, and two bearing housings. The thermal sub-system including the rotor, rotor ends, bearing pad, and bearing shell is presented in Fig. 5.1. Within the sub-system, the heat generated by viscous dissipation in the air film is transported to the bearing pads and rotor. The heat to the rotor is conducted through the rotor shell and convected to the ambient air through the exposed rotor surfaces. The heat flux to the bearing pad (modeled as lumped heat capacity) is transported to the bearing shell through the pivot web by heat conduction. At the interfaces of the sub-system (rotor ends and bearing shell), either temperature or heat flux boundary conditions can be given. For the current test rig configuration, the rotor center is adiabatic due to the symmetry of the test rig. Axial heat flux within the rotor shell and heat convection to the ambient is modeled using the 1-D fin theory [35]. Multiple iteration loops are located within the software to satisfy the heat flux continuity at multiple interfaces. Detailed approach on the solution procedures will follow.

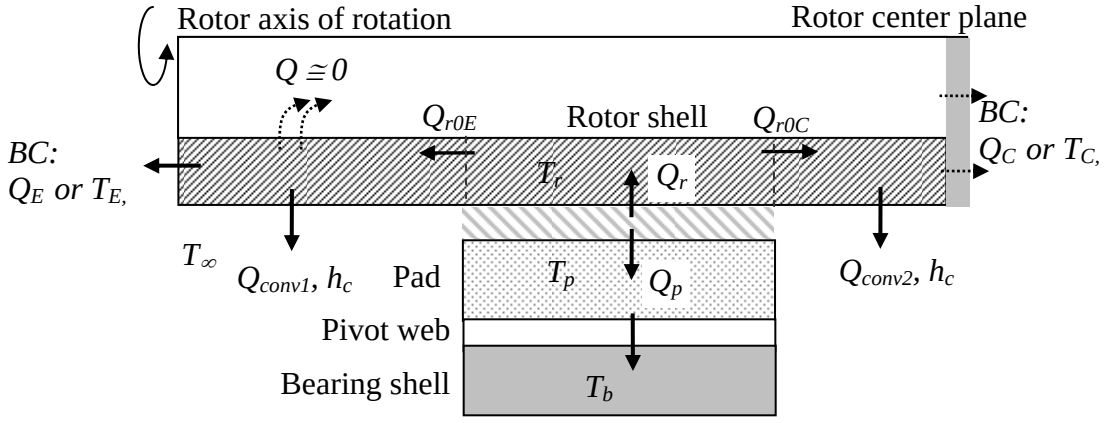

Fig. 5.1 Heat flux within the thermal sub-system of current test rig

Design parameters and rotor and pad motions of CFTPBs are presented in Fig. 3.2, and for an arbitrary pad and rotor position, local film thickness is described by Eq. (3.1). Rotor growths are caused by large centrifugal forces or temperature rises. Rotor centrifugal growths for the hollow rotor (Table 5.1) are estimated from a cylindrical plane stress model [32], and given by Eq. (3.7). Thermal rotor growths are estimated by the following equation

$$r_{gt} = \alpha R\left(T_{r\_av} - T_\infty\right) \tag{5.3}$$

where α is the linear thermal expansion coefficient of rotor, T_{r_av} and T_∞ are the rotor temperature averaged along the rotor axis and the ambient temperature, respectively. The total rotor growth is a summation of the centrifugal and thermal growths. However, thermal distortion of the pad was not considered.

5.2.1 THD model for Air Film

5.2.1.1 Governing Equations

Governing equations of the generalized Reynolds Equation and the energy equation are employed to calculate temperature fields in the air film. For most operating conditions, air flow in the film is laminar due to very small Reynolds number much less than 1000. Temperature evaluation in the air film at steady state operations requires simultaneous calculation of the generalized Reynolds Equation and the energy equation, given by

$$\frac{\partial}{\partial x}\left(\frac{\rho h^3}{\mu}\frac{\partial p}{\partial x}\right)+\frac{\partial}{\partial z}\left(\frac{\rho h^3}{\mu}\frac{\partial p}{\partial z}\right)=6U\frac{\partial}{\partial x}(\rho h) \tag{5.4}$$

$$\rho c_p V\cdot\nabla T=\nabla\cdot(k\nabla T)+V\cdot\nabla p+\Phi \tag{5.5}$$

where c_p is the air specific heat capacity under constant pressure, V is the air velocity vector, k is the air heat conductivity, and Φ is the heat dissipation function. The coordinate system for the governing equations in the air film is given in Fig. 5.2, where x, y and z denote the circumferential, cross-film and axial directions, respectively. The two equations are coupled by temperature- and pressure-dependence of the air viscosity and density. The ideal gas equation and the linear viscosity-temperature relation [26] lead the governing equations to be coupled only by temperature and pressure fields. Neglecting

all the velocity gradients except for $\partial u/\partial y$ and $\partial w/\partial y$ [28], the viscous heat dissipation term (Φ) is simplified to

$$\Phi = \mu\left[\left(\frac{\partial u}{\partial y}\right)^2 + \left(\frac{\partial w}{\partial y}\right)^2\right]. \tag{5.6}$$

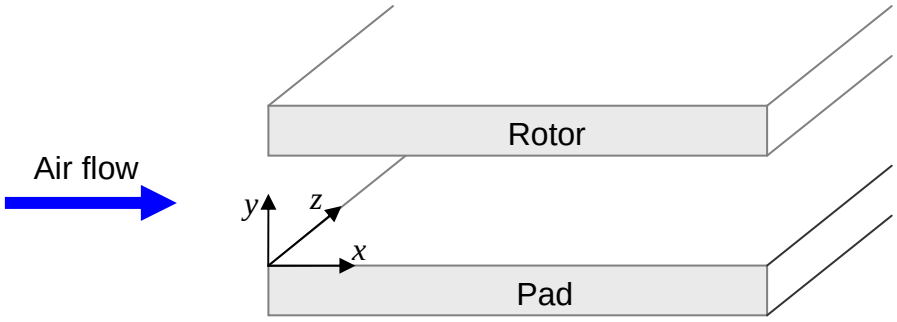

Fig. 5.2 Coordinate system for the energy equation and the generalized Reynolds equation in the air film

The Reynolds equation is solved to find a pressure field with a given temperature field, and then with the calculated pressure the energy equation is solved to calculate the temperature. The iteration continues until they converge. Mismatch of the 2-D pressure field from the Reynolds equation with the 3-D temperature field is resolved by the assumption of constant pressure across the film from the order of magnitude analysis of the momentum equation. Discretization of the energy equation follows the power-law scheme [31] to ensure all the coefficients not to be negative for convective terms with large Peclet numbers. Number of grid points within one pad was increased gradually

until both pressure and temperature do not change within 0.3%. Final grid scheme for the THD studies were 30×20×8 for *x*, *z*, and *y* direction, respectively.

5.2.1.2 Boundary Conditions

Appropriate thermal boundary conditions at the pad edges, as well as on the rotor and pad surfaces, should be determined for the solution to the governing equations. In the air film on a pad, there are one incoming flow from the leading edge, two side flows from the side edges, and one exit flow through the trailing edge. Thermal boundary condition for the inlet flow is determined in a different way from those for the outgoing (side and exit) flows. The thermal boundary conditions on the rotor and bearing pad will be discussed later.

Inlet flow temperature has large influence on the air film temperature [36]. Mixing between the exit flow from the previous pad and the ambient air sucked into the chamber between pads is assumed to occur intensively accompanying severe turbulence because the dimension of the chamber (Fig. 5.3) is much higher than the film thickness and the exit flow is very fast. The inlet temperature (T_{inlet}) is defined as a weighted value of the suction flow temperature (T_{suc}) and the exit flow temperature (T_2) from the previous pad, i.e., $T_{inlet} = T_{suc}C_1 + T_{exit}C_2$ [37]. The coefficients of C_1 and C_2 can be determined by experiments considering heat transfer through the wall [36]. However, a reasonable inlet temperature can be found without resorting to empiricism by utilizing the mass and energy balance in the chamber among the exit flow from the previous pad ($\dot{m}_{exit}$), the suction flow ($\dot{m}_{suc}$), and the inlet flow ($\dot{m}_{inlet}$), assuming full mixing of the

exit flow with the suction flow and negligible heat transfer to the surrounding solid walls. This method is very simple and widely used in [22,23,28], and thus adopted in this THD analysis.

In a chamber between pads (Fig. 5.3), the suction flow $\dot{m}_{suc}$ is determined by the mass balance

$$\dot{m}_{exit} + \dot{m}_{suc} = \dot{m}_{inlet} \tag{5.7}$$

Applying energy balance to the air flows in the chamber and assuming constant heat capacity of the air flows within temperature ranges of interest, the inlet temperature is determined by

$$\dot{m}_{exit} T_{exit} + \dot{m}_{suc} T_{suc} = \dot{m}_{inlet} T_{inlet} \tag{5.8}$$

where T_{exit}, T_{inlet}, and T_{suc} are the temperatures of $\dot{m}_{exit}$, $\dot{m}_{inlet}$, and $\dot{m}_{suc}$, respectively. The calculated inlet temperature becomes a boundary condition at the leading edge.

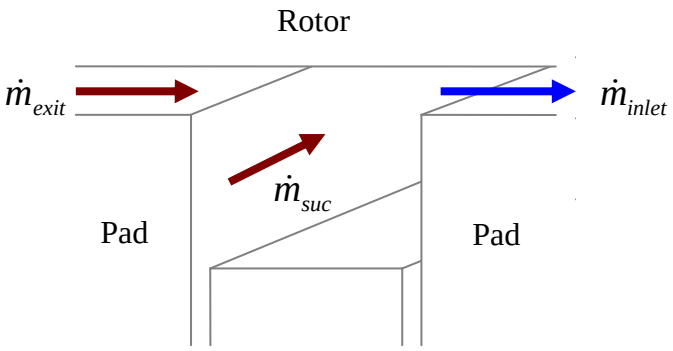

Fig. 5.3 Control volume of the chamber between pads

Thermal boundary conditions for the exit and side flows at the pad edges are remarkably simple, compared to the inlet boundary condition. All the pads have a positive pressure field due to self-adjusting motion of pads and have strong negative pressure gradients toward the trailing and side edges, which generate fast outgoing flows. From hydrodynamic analyses, the side flows as well as the exit flow have large Peclet numbers much higher than 10, which results from the high flow velocity and small air conductivity. For Peclet numbers over 10, temperature boundary condition is not necessary to be defined with the power-law scheme [31][1]. As a result, no boundary condition for both the exit and side flows is needed at the pad edges.

5.2.2 Heat Transfer Model to Pad

Rotor and pad surface temperatures become wall boundary conditions for the THD model in the film. While rotor temperature is assumed uniform in the circumferential direction, each pad has a different average temperature because of eccentricity of the rotor.

CFTPBs have complicated configurations with very narrow pivot web and beam structures, and slender and wide pads in the bearing shell. It is assumed that thermal effect of the pivot web is negligible, and pad heat conduction occurs only in the radial direction within pads. If only heat convection on the backside surface of pad is considered, heat conduction through the pad is equal to the outgoing heat flux from the backside surface of pad to the surrounding air, i.e.,

[1] In the power-law scheme, large Peclet numbers higher than 10 make corresponding nodal coefficients zero in finite difference methods, which results in the nodal temperature not taken into account in the numerical solution.

$$Q_p = k_p \frac{T_{P\_in} - T_{P\_out}}{t_p} = h_n (T_{P\_out} - T_\infty) \tag{5.9}$$

, where k_p is heat conduction coefficient of pad, T_{P_in} and T_{P_out} are the pad temperatures on the surfaces to the air film and to the ambient, respectively, and t_p is the pad thickness (Fig. 5.4). For stainless steel, k_p = 50.2 *W/mK*, and typical natural convection coefficients on flat surfaces (h_n) is approximately 5 W/m^2K. The pad thickness (t_p) does not exceed 3mm in most cases. Rearranging the above equation leads to $T_{P\_in} = Bi(T_{P\_out} - T_\infty) + T_{P\_out}$, where Biot number $Bi = h_n t_p / k_p$. Substitution of the thermal properties and geometry yields $Bi \approx 3\times10^{-4}$, which justifies the lumped heat capacity model.

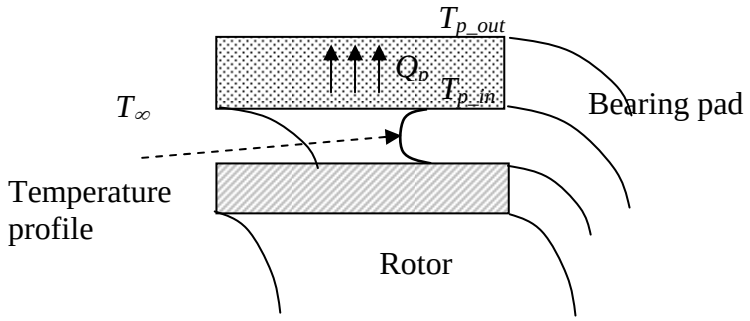

Fig. 5.4 Heat flux model for bearing pads

For the purpose of ensuring the lumped heat capacity model even with heat conduction through pivot web, numerical simulations were conducted with the 2-D heat conduction model using commercial software. The simulated temperature field at one pad is presented in Fig. 5.5(a), where the pad inner surface and bearing shell outer surface are given 30°C and 15°C, respectively, and other surfaces are assumed adiabatic. Overall pad temperature is approximately uniform with the given temperature of 30°C and bearing shell temperature is also almost uniform as the room temperature. Maximum temperature variation in both the pad and bearing shell is about 1.5°C. Stiff temperature variation is observed only at pivot. The heat flux field at pad and bearing shell for the same boundary conditions is shown in Fig. 5.5(b). From the simulations, a linear relation of heat conduction through the pivot web can be found as

$$Q_p = C_w(T_p - T_{bs}) \tag{5.10}$$

where T_p and T_{bs} denote the pad and bearing shell temperatures, respectively. C_w is a proportionality constant which can be evaluated for given web configuration through numerical simulation or experimental measurement. The bearing shell temperature T_{bs} is a boundary condition[2]. For given bearing geometry, it was estimated as 0.195 from numerical simulation using commercial software. Remarkably, the ratio of heat convection to the back side of the pad (assuming natural convection to ambient air) to the heat conduction through the pivot web is in the order of $O(10^{-2})$. Consequently, pad

[2] In most applications, the bearing shell temperature can be measured.

temperature is estimated using the lumped heat capacity model accounting for only heat conduction through the pivot web by Eq. (5.10). However, heat loss by forced convection on the backside of the pad is compatible to the conduction through the pivot web and should not be neglected

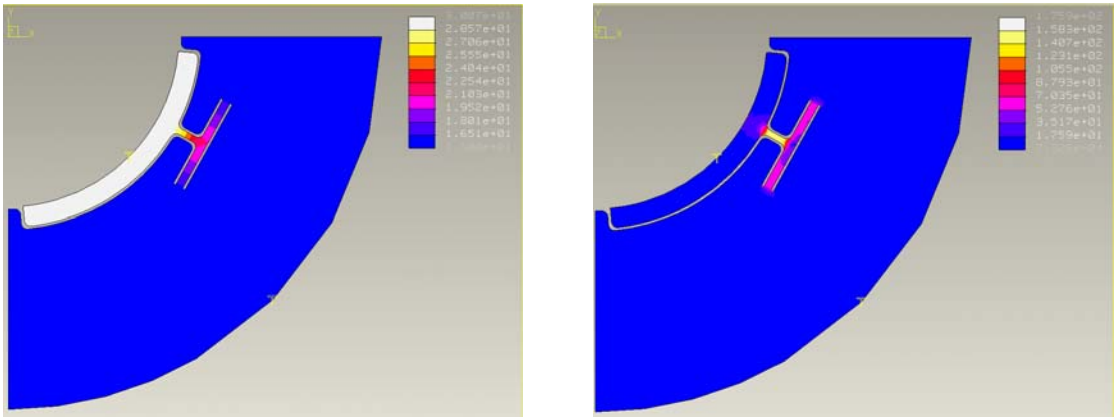

(a) Temperature field (b) Heat flux field

Fig. 5.5 Temperature field and heat flux filed at pad and bearing shell

5.2.3 Heat Transfer Model to Rotor

In many microturbomachinery applications, hollow rotors are used to reduce the rotor mass and increase bending critical speed. Therefore, the model developed in this paper applies to hollow rotor. The heat transferred to the rotor from the air film travels through the rotor shell by conduction and then convected on the rotor surface to the ambient.

At a given axial position, temperature of the rotor shell (T_r) is assumed to be constant in the radial (thickness) direction due to high thermal rotor conductivity and

small rotor shell thickness, and constant in the circumferential direction due to high thermal rotor conductivity and very fast rotor spin speed. Therefore, heat conduction within the rotor shell is modeled as a 1-D heat conduction problem along the axial direction.

The developed THD model can handle general boundary conditions of the sub-system such as temperature or heat flux at the rotor ends. For the current test rig configuration (see Fig. 5.1), the rotor center plane is adiabatic due to symmetry, and the other end with a turbine can be modeled as either heat flux or temperature boundary. The outer bearing surface is assumed to have the ambient temperature. Conceptually, the total thermal sub-system is composed of three domains as presented in Fig. 5.6, and the sub-domains are interconnected by the rotor. The interfaces of the domain I are the cross-section of the rotor at the bearing edge and the rotor end surface where the turbine is attached. The rotor end surface can be defined as a heat flux source (Q_E) or fixed temperature (T_E). The domain II encloses the bearing and the rotor inside the bearing: the boundaries in the rotor have heat fluxes Q_{r0E} and Q_{r0C} to the domain I and III, respectively, and the bearing outer surface is defined with a given temperature (T_B=T_∞ in this research). The domain III includes the rotor part from the right bearing edge to the center plane, and has heat flux Q_{r0C} at the boundary with the domain II and adiabatic condition (Q_C=0) at the rotor center plane. The domain I and III include the heat convection to the ambient air (Q_{conv1}, Q_{conv2}) within the domain, respectively. The three domains should meet the heat flux balances within the domain, and also total global heat balance should be satisfied.

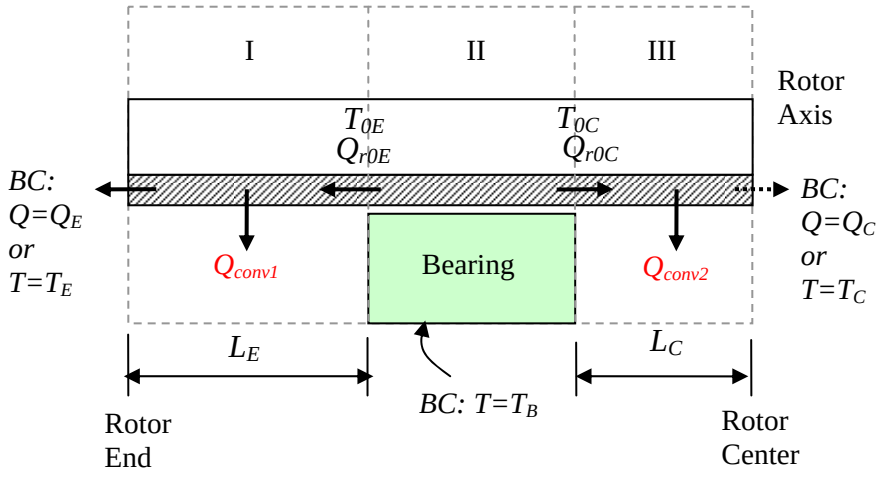

Fig. 5.6 Domains and thermal boundary conditions within total thermal sub-system

5.2.3.1 Heat Convection on the Exposed Rotor Outer Surface

Heat convection from the exposed rotor surface to the ambient air is calculated using the heat convection theory for a rotating cylinder, given by Eq. (5.11) [38]. Given a rotor geometry and a rotating speed, the heat convection coefficient on the exposed rotor surface is a function of rotor diameter (D) and rotation speed (Ω), defined as function of Reynolds number and Prandtl numbers as

$$h_c = 0.133Re^{2/3}Pr^{1/3}(k_a/D), \tag{5.11}$$

where $Re = \Omega D^2/\nu_a$ and $Nu = 0.133Re^{2/3}Pr^{1/3}$ for $Re < 4.3\times10^5$ and $0.7 < Pr < 670$. At 300°K of air, kinetic viscosity $\nu_a = 15.66\times10^{-6}$ m^2/s, Prandtl number $Pr = 0.69$, and heat conductivity of air $k_a = 0.0267$ W/(mK).

5.2.3.2 Heat Convection on the Rotor Inner Surface

Heat convection from the rotor shell to the rotor inner surface follows the same heat convection coefficient as Eq. (5.11). However, in many applications, both ends of the hollow rotor are sealed by impellers or other components. Due to the very small thermal capacity of the air, heat transfer to the air inside the hollow rotor is much less than heat conduction within the rotor shell. Therefore, in the currently-developed THD model, the heat convection from the rotor inner surface is neglected. However, the convection term can be easily added to energy balance within each domain in Fig. 5.6.

5.2.3.3 Axial Heat Flux within the Rotor at the Bearing Edge

Heat flux at the bearing edge serves as a boundary condition to find the temperature profile of the rotor inside the bearing. The heat fluxes at the left and right bearing edges are

$$Q_{r0E} = Q_{conv1} + Q_E \tag{5.12a}$$

$$Q_{r0C} = Q_{conv2} + Q_C \tag{5.12b}$$

, where Q_{conv1} and Q_{conv2} are the axial heat fluxes in the rotor at the left and right bearing edge, respectively, caused by the heat convections on the corresponding rotor outer surfaces when $Q_E = Q_C = 0$. The heat convections Q_{conv1} and Q_{conv2} are calculated by the fin theory [35] using the heat convection coefficient, Eq. (5.11). Evaluation of Q_{conv1} and

Q_{conv2} assumes adiabatic conditions at the rotor end surfaces. From the fin theory, the heat convections on the rotor outer surface can be given by

$$Q_{conv1} = k_r A\left[m\left(T_{0E} - T_\infty\right)\tanh mL_E\right] \tag{5.13a}$$

$$Q_{conv2} = k_r A\left[m\left(T_{0C} - T_\infty\right)\tanh mL_C\right] \tag{5.13b}$$

where $m^2 = h_c P / k_r A$, R and R_i are outer and inner radius of rotor, respectively, $P = 2\pi R$ is a circumferential length of rotor, $A = \pi(R^2 - R_i^2)$ is the cross-sectional area of rotor, h_c is the heat convection coefficient on the exposed rotor surface given by Eq. (5.11), and k_r is the heat conduction coefficient of the rotor.

When temperature boundary conditions are given at the rotor end surfaces instead of heat flux, equivalent conductive heat fluxes through the rotor shell [38] are evaluated as

$$Q_{E\_C} = k_r \frac{2\pi L_E}{\ln(R / R_i)}(T_{0E} - T_E) \tag{5.14a}$$

$$Q_{C\_C} = k_r \frac{2\pi L_C}{\ln(R / R_i)}(T_{0C} - T_C) \tag{5.14b}$$

which replace Q_E and Q_C respectively in Eq. (5.12).

5.2.4 Numerical Solution Procedure

Flow chart for solution procedures are given in Fig. 5.7. At a given rotor speed, an initial equilibrium position of rotor center and pads, and isothermal air film pressure field are obtained using the orbit simulation method [3] by solving the isothermal Reynolds equation for a given external load (rotor weight). No imbalance is implemented, and the orbit simulation finds the static equilibrium very quickly. Starting from the initial equilibrium pressure and film thickness, pressure-temperature iterations are performed as shown in Fig. 5.7. In the air film, the generalized Reynolds equation, Eq. (5.4), and the energy equation, Eq. (5.5), are solved simultaneously implementing the ideal gas equation and the viscosity-temperature relation. While pressure and temperature of the air film is being iterated, the rotor and pad temperatures are determined by solving a 1-D heat conduction problem in the axial direction and lumped heat capacity model. At the same time, inlet flow temperature is solved from the mass and energy balance in the chamber between pads. The calculated rotor, pad, and inlet flow temperatures act as boundary conditions for the air film temperature calculation. Iterations between the film temperature and the boundary conditions are required. Once all the temperature fields are calculated for the initial equilibrium point, a new equilibrium position is searched accounting for thermal rotor growth, which is determined from the calculated rotor temperature. The iterations for the pressure-temperature and equilibrium position continue until global convergence of all the temperatures, pressure, and static equilibrium. The rotor centrifugal growth is taken into account in the all iteration loops.

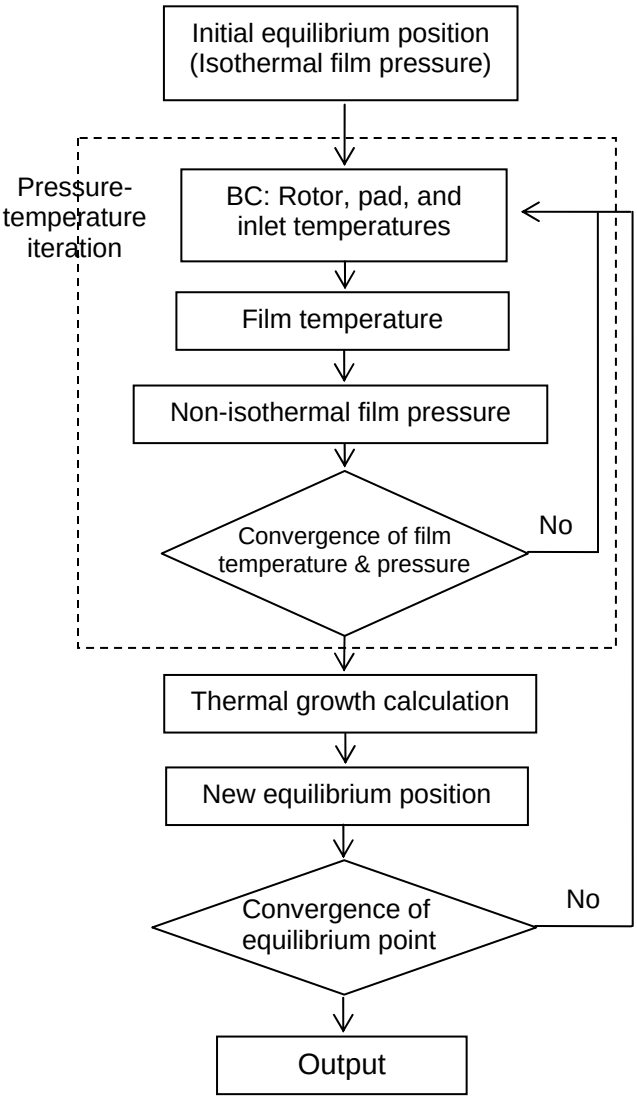

Fig. 5.7 Flow chart for the THD analysis

5.3 Numerical Simulation

Developed THD analysis method was applied to a rotor-bearing system in the current imbalance test rig shown in Fig. 5.1. Because it is very difficult to measure rotor

surface temperature within the bearing with current test rig configuration, and the manufactured bearings do not allow attachment of thermocouples on the bearing pads, experimental verifications could not be attempted. Currently, a new test rig with new bearings and high speed electric drive that allows measurement of rotor and pad temperature is under construction. In this paper, developed THD sub-module is applied to current imbalance response test rig to investigate THD behavior of the tilting pas gas bearing with different design parameters. Because rotor center is a symmetry plane, Q_C=0 in Eq. (5.12b). Furthermore, the heat loss by impulse turbine at the other end is modeled as large heat flux. Because actual heat loss from the turbine cannot be evaluated, it was assumed the heat loss at the turbine is five times the heat convection on the rotor outer surface, i.e., $Q_E = 5Q_{conv1}$ for initial parametric studies. Specifications of the bearing and rotor follow the actual configuration except for the pad radial stiffness and rotor mass. In the current test rig for imbalance response test, the upper pads (pads 1 and 4) have smaller stiffness than the lower pads (pads 2 and 3). Table 1 provides other design parameters used in the simulations. The THD numerical simulations can provide more accurate understandings of thermo-physical behaviors of gas bearing systems and allow identifying important design parameters for thermal characteristics. Numerical simulations were performed with grids of 30×20×8 in the circumferential, axial, and cross-film direction, respectively.

Table 5.1 Parameters for THD analysis

CFTPB Parameters	SI unit	
Number of pads	4	
Pad mass (m_p)	16×10^{-3}	kg
Pad inertia (i_p)	1.0×10^{-6}	kg-m^2
Pad start angle	5	degree
Pad arc length	80	degree
Pad thickness (t_p)	3	mm
Pivot offset	0.7	
Preload (r_p)	0.5	
Tilting stiffness (k_ϕ)	20	Nm/rad
Radial stiffness (k_δ)	1×10^{7}	N/m
Bearing length (L)	33.2	mm
Nominal clearance (C)	35	μm
Load per bearing (m_r)	4.06	N
Rotor diameter ($2R$)	28.60	mm
Total rotor length	120	mm
Rotor wall thickness (t_r)	3	mm

5.3.1 Simulated Temperature Fields

The simulated rotor temperature is presented in Fig. 5.8 along the rotor axis toward the rotor symmetry plane at 60 krpm. Axial position is non-dimensionalized by axial length of the bearing and numbers 0 and 1 correspond to the left and right edge of the bearing. As described in Section 2.3, heat transfer within the rotor is modeled as 1-D heat conduction along the rotor axis with constant temperature in the circumferential

direction. Outgoing heat fluxes at the bearing edges through the rotor shell cause rotor temperature profile inside bearing to appear parabolic. Rotor temperature at the left bearing edge (where Q_E is imposed) is smaller than that at the right bearing edge (adiabatic, Q_C =0).

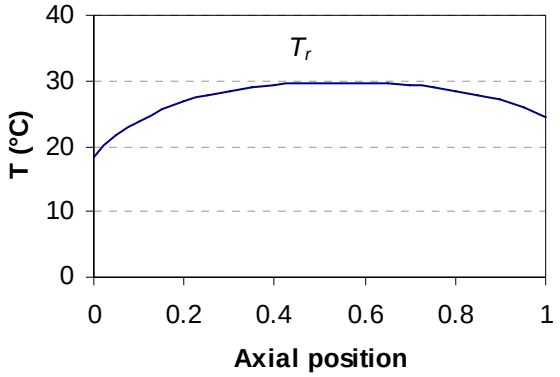

Fig. 5.8 Rotor temperature along the rotor axis, 60krpm, C=35μm

The simulated pad and inlet flow temperatures are presented in Fig. 5.9. The lower pads (Pad 2 and 3) have slightly higher temperatures than the upper pads (Pad 1 and 4) due to rotor eccentricity toward the lower pads. However, the eccentricity under the applied load is so small (about 0.02) that the temperature difference between the upper and lower pads is relatively small, less than 0.2°C. Inlet flow temperatures of pads, determined from mass and energy balances with the suction flow and the exit flow from the previous pad, have also small differences less than 0.5°C. The pad and inlet temperature variations (< 0.5°C) are practically negligible compared to those of the rotor temperature (Fig. 5.8) and the film temperature (Fig. 5.10 and Fig. 5.11).

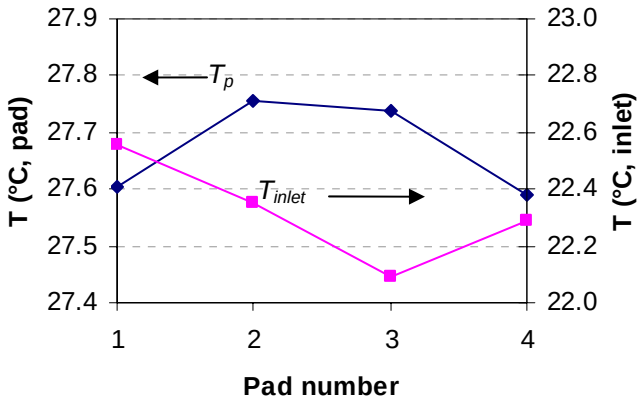

Fig. 5.9 Pad and inlet flow temperature, 60krpm, C=35μm

The simulated air film temperature field (Fig. 5.10) is presented in the xy plane (see Fig. 5.2) at the bearing axial center of Pad 3 at 60krpm. The film temperature in the middle is higher, which indicates cross-film heat transfer to the rotor and pad. Overall temperature gradient in the cross-film direction near the pad boundary is higher because the pad temperature of 27.7°C (Fig. 5.9) is lower than the rotor temperature of 30°C at the axial center (Fig. 5.8). Prompt temperature rise of inlet flow from 22 to 28°C is observed at the inlet area due to heat conductions from both the rotor and pad.

The simulated bulk film temperature (averaged over the film thickness) at Pad 3 is presented in Fig. 5.11(a). The circumferential positions 0 and 1 correspond to the leading and trailing edge of the pad, respectively. Axial film temperature profile follows the parabolic rotor temperature profile in Fig. 5.8. A bulk film temperature in the circumferential direction at the axial center of each pad is presented in Fig. 5.11(b) with an insert which shows slightly higher temperatures of the lower pads (Pad 2 and 3). The

film pressure in the circumferential direction at the axial center of each pad is presented in Fig. 5.11(c). Pressure increases until 80% of the pad arc length causing large amount of side flows. The inlet flow gains the temperature right after entering the film due to heat conductions from the pad and rotor. However, the film temperature slightly drops toward the pivot due to the large side flow. The stiffer temperature drop near the exit is due to pressure-related work with strong negative pressure gradients (the 3rd term in Eq. (5.5)).

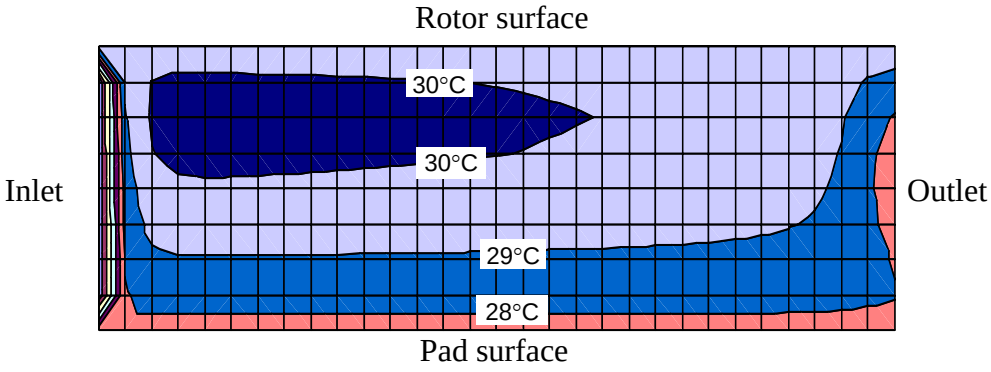

Fig. 5.10 Film temperature field in the xy plane at the axial center of Pad 3, 60krpm, C=35μm

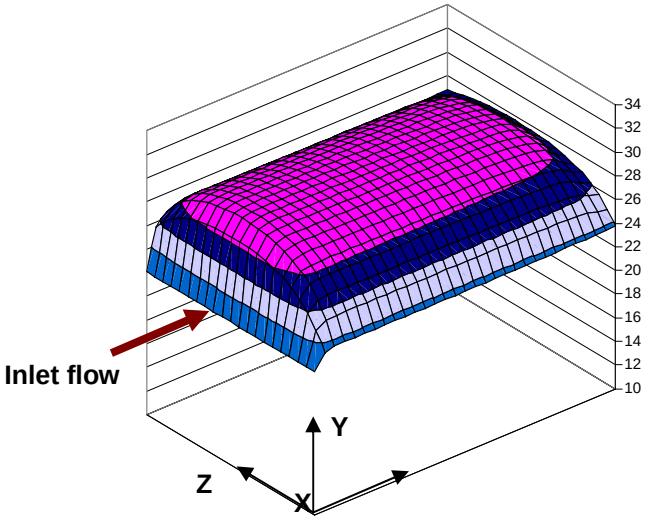

(a) Bulk film temperature field at Pad 3

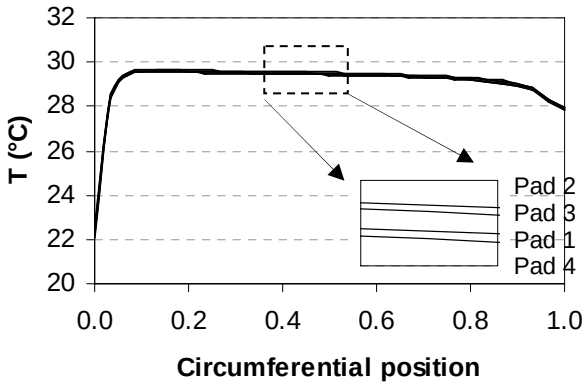

(b) Circumferential bulk film temperature at the axial center of each pad

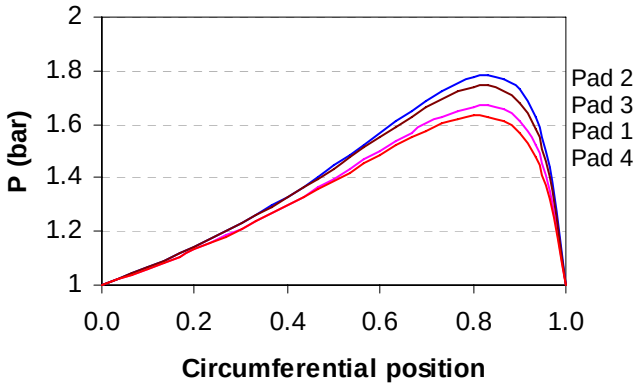

(c) Film pressure in the circumferential direction at the axial center of each pad

Fig. 5.11 Bulk film temperature and pressure distribution, 60krpm, C=35μm

Averaged rotor, pad, and bulk film temperatures over rotor speeds of 10~80krpm are presented in Fig. 5.12. The averaged bulk film temperature is higher than the averaged pad and rotor temperatures by small differences less than 1.5°C (however, larger temperature differences exist within the film as in Fig. 5.10). All the temperatures show approximately parabolic increases with rotor speeds, and reached up to about 45°C at 80krpm (temperature rises of 30°C). Rotor thermal growth due to the parabolic temperature rise is expected to affect overall bearing performance significantly at high speeds.

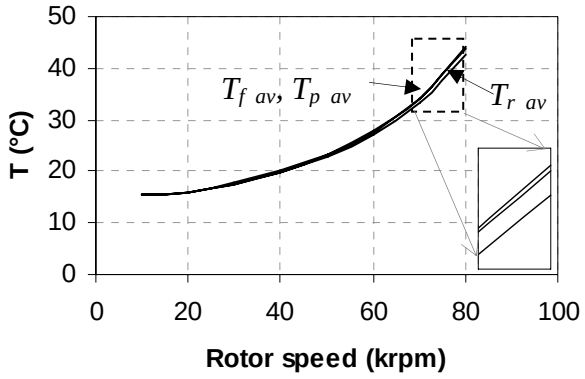

Fig. 5.12 Averaged rotor, pad, and bulk film temperature vs. rotor speed

5.3.2 Parametric Study

Parametric studies are conducted in terms of nominal clearance and external load. In general, larger nominal clearance tends to cause smaller temperature rise, and larger

external load tends to cause larger rotor eccentricity and higher temperature rise in the loaded pads.

5.3.2.1 Effects of Nominal Clearance on Temperature

THD analyses were performed with various nominal clearances from 30 to 40μm at a rotor speed of 60krpm. Three rotor temperature profiles along the rotor axis for nominal clearance of 30, 35, and 40μm are presented in Fig. 5.13. A similar tendency of temperature rise with nominal clearance is also observed in pad and bulk film temperatures given in Fig. 5.14 and Fig. 5.16. On the other hand, temperature rise of inlet flow is less than those of the rotor and pad due to mixing with the ambient air. The pad and inlet temperatures have very small temperature differences due to almost centered rotor position (eccentricity of 0.02). The inlet temperature of Pad 1 is slightly higher than other pads due to higher exit temperature of Pad 4, where temperature drop at the exit is minimal due to smaller pressure gradient. Pad 4 has smaller negative pressure gradient at the exit than Pad 2 and 3. Therefore, exit temperature of Pad 2 and 3 are slightly lower than that of Pad 4, which causes relatively lower inlet temperature of Pad 3 and 4. All the temperature plots for rotor, pad, inlet, and film show non-linear behavior with respect to nominal clearance. For example, the decrease of nominal clearance from 35 to 30μm leads to larger temperature rise than the decrease of nominal clearance from 40 to 35μm does.

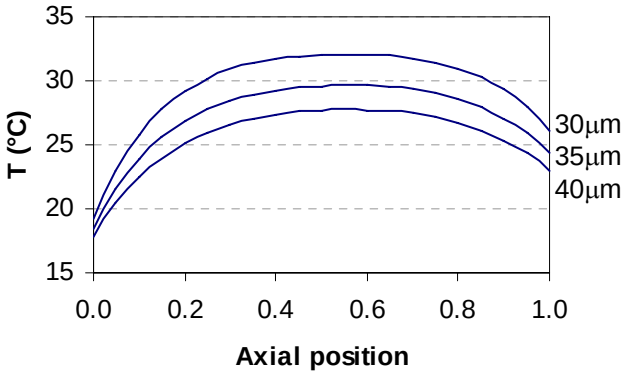

Fig. 5.13 Rotor temperature along the rotor axis for nominal clearance of 30~40μm, 60krpm

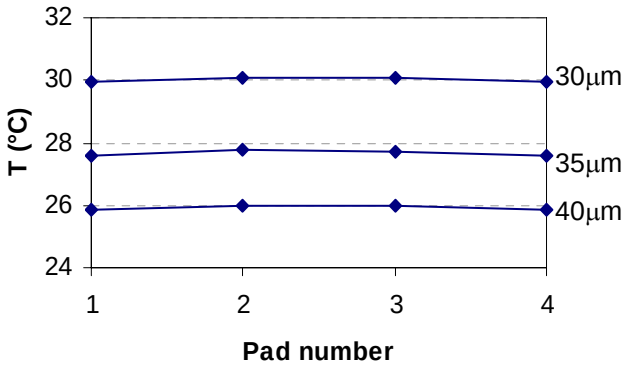

Fig. 5.14 Pad temperature for nominal clearance of 30~40μm, 60krpm

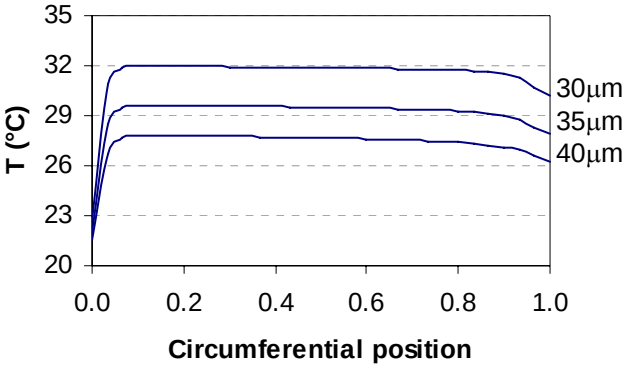

Fig. 5.15 Bulk film temperature along circumference at the axial center of pad 3 for nominal clearance of 30~40μm, 60krpm

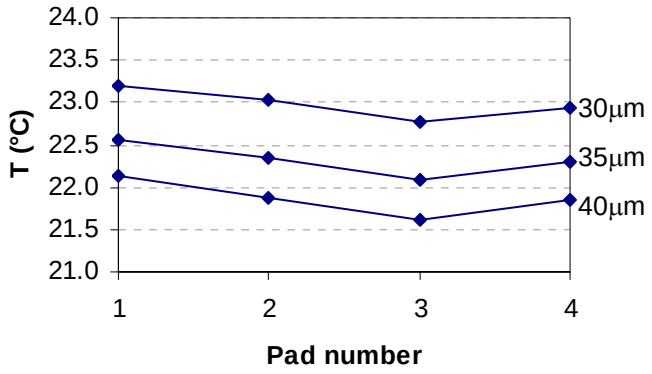

Fig. 5.16 Inlet flow temperature for nominal clearance of 30~40μm, 60krpm

5.3.2.2 Effects of External Load on Temperature

Effects of external loads on the THD behavior were investigated by increasing the external loads to 16.23 N and 28.4N at 60krpm. As given in Fig. 5.17, as external load is increased to 16.23N and 28.4N, non-dimensional rotor eccentricities are increased to 0.11, and 0.19, respectively. Rotor, pad, and inlet flow temperatures are presented in Fig. 5.18, Fig. 5.19 and Fig. 5.20. In Fig. 5.18, the rotor temperature is not sensitive to the increased external load, and only loaded pads experience temperature rise as in Fig. 5.19. The inlet temperature of Pad 1 is the highest among pads due to the highest exit temperature of Pad 4. In addition, for larger loads, the inlet temperature of Pad 3 decreases because the exit flow from Pad 2 becomes small due to increased rotor eccentricity toward the Pad 2, resulting in large suction flow with ambient temperature. Bulk film temperatures also show uneven temperature rises with loads among pads: the lower pad (Fig. 5.21(a)) experiences higher film temperature rise than the upper pad (Fig. 5.21(b)). Bulk film temperatures of all the pads with the highest load (28.40 N) are

presented in Fig. 5.22, where the lower pads (Pad 2 and 3) have higher film temperatures than the upper ones (Pad 1 and 4). In conclusion, large eccentricity due to large external load leads to uneven rotor, pad, inlet, and film temperature distributions over pads, i.e., the lower pads experience higher temperature rises than the upper ones. In general, effects of external load on temperature rises appear to be smaller than the nominal clearance effects within the ranges of external loads investigated.

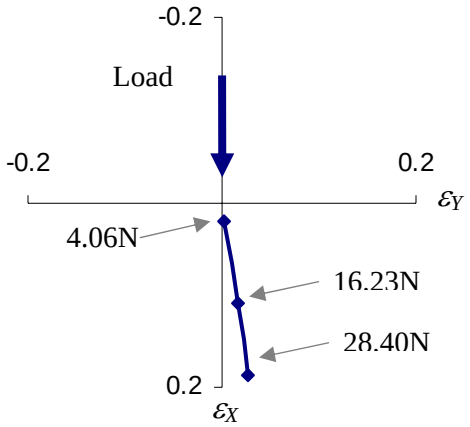

Fig. 5.17 Equilibrium position of rotor at different external loads, 60 krpm, C=35μm

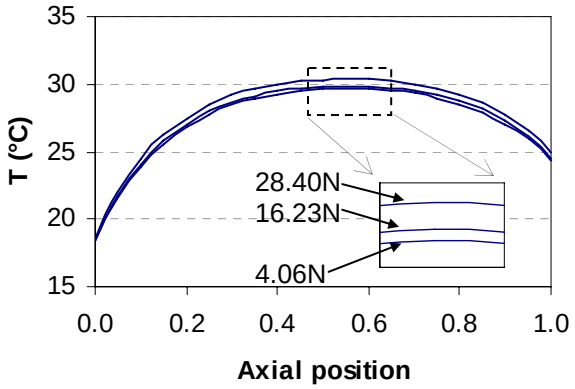

Fig. 5.18 Rotor temperature for different external loads along the rotor axis, 60krpm, C=35μm

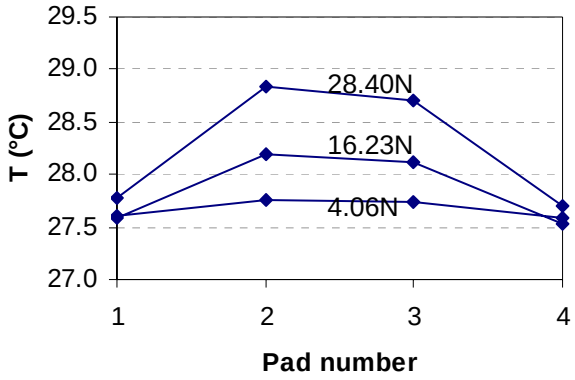

Fig. 5.19 Pad temperature along the rotor axis for different external loads, 60 krpm, C=35μm

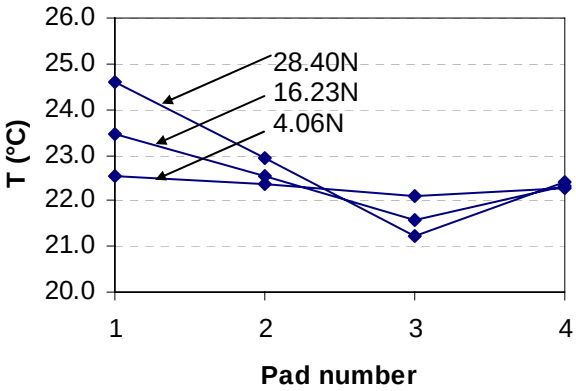

Fig. 5.20 Inlet temperature along the rotor axis for different external loads, 60krpm, C=35μm

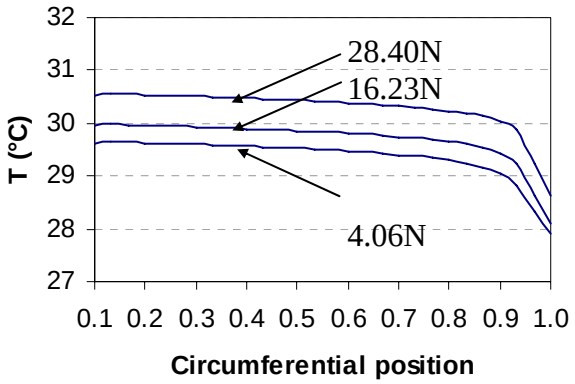

(a) Pad 2 (lower pad)

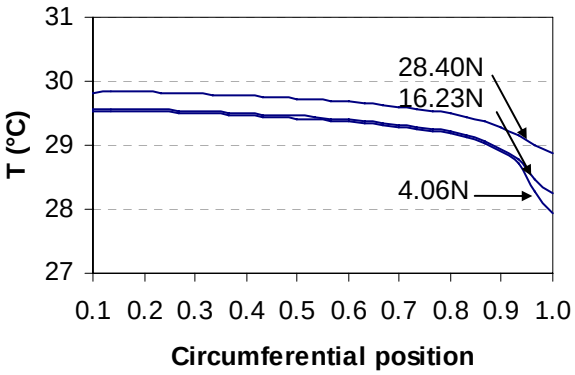

(b) Pad 4 (upper pad)

Fig. 5.21 Bulk film temperature along circumferential direction at the axial center for different external loads, 60krpm, C=35μm

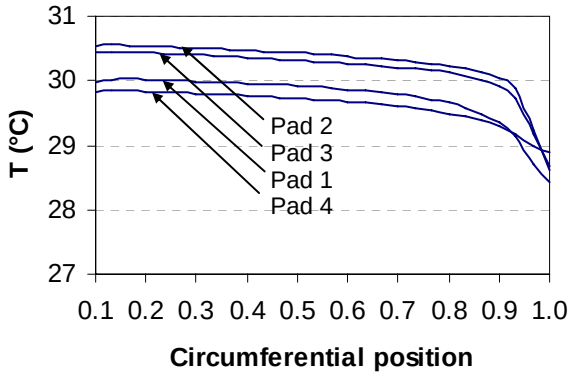

Fig. 5.22 Bulk film temperature at the center along circumferential direction at the axial center for external load of 28.40N, 60krpm, C=35μm

5.3.3 Other Case Studies

Thermal analyses were performed for different boundary conditions at the rotor end as summarized in Table 5.2. Case 2 is simulating the case when heat loss is only due to heat convection on the rotor surface. Case 3 is a limiting case of Case 1 considering that the rotor end temperature is specified as the ambient temperature, 15^{o}C.

Table 5.2 Description of thermal analysis cases

	Rotor growth	Pressure	BC at rotor end
Case 0	r_{gc}	Isothermal	-
Case 1	r_{gc} & r_{gt}	Non-isothermal	$Q_E = 5Q_{conv1}$
Case 2	r_{gc} & r_{gt}	Non-isothermal	$Q_E = 0$
Case 3	r_{gc} & r_{gt}	Non-isothermal	$T_E = 15^{o}$C

Centrifugal and thermal growths for Case 1 are presented in Fig. 5.23, co-plotted with total rotor growth. In general, rotor growth is equivalent to reduction of average clearance, which leads to increase of system natural frequency.

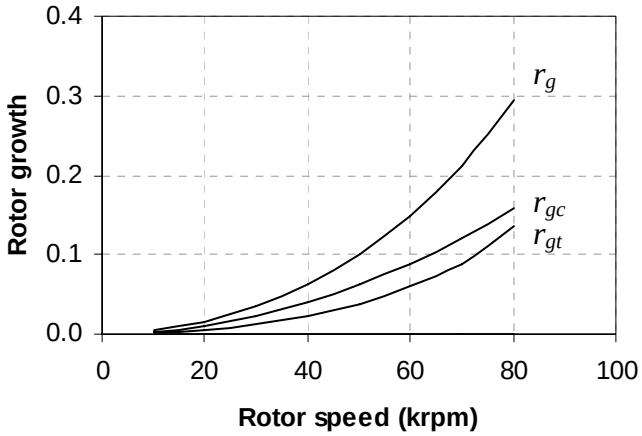

Fig. 5.23 Total growth for Case 1 over rotor speeds of 10~80krpm, co-plotted with rotor centrifugal and thermal growth (rotor growth was normalized by nominal clearance)

Rotor temperatures for different cases over rotor speed ranges of 10~80krpm are presented in Fig. 5.24. Thermal boundary condition of $Q_E = 5Q_{conv1}$ yields very similar but slightly higher rotor temperature compared to Case 3, where the rotor end temperature is specified as room temperature, showing the turbine cooling of $5Q_{conv1}$ 5 is reasonable for the impulse turbine. However, Case 2 reaches up to 60°C at 80krpm with temperature difference of more than 15°C from Case 1 or 3. Not shown is the rotor thermal growth for Case 2 which is quite significant rendering total rotor growth (including centrifugal growth) approaching set bore clearance at 80krpm. Consequently, bearing operations without an adequate cooling mechanism can cause thermal runaway at high speeds.

Rotor temperatures within the bearing at 60 krpm are presented in Fig. 5.25 for different levels of heat flux boundary conditions at the rotor end. As heat loss at the rotor end approaches infinite, the rotor temperature at the bearing edge approaches the room

temperature (15^{o}C). On the other hand, the changes of the rotor temperatures at the right end where the symmetry boundary condition was applied are much smaller than those at the left end.

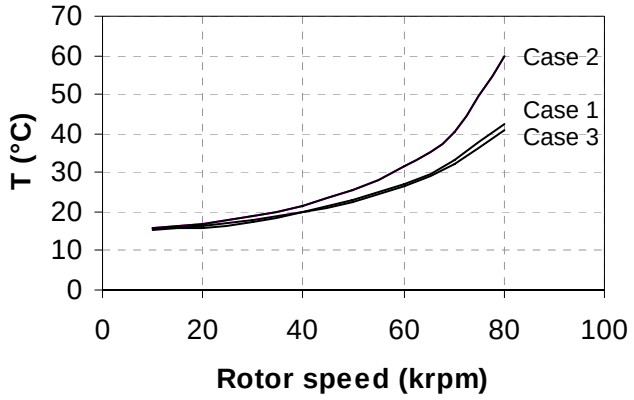

Fig. 5.24 Rotor temperature with speed for different thermal boundary condition at the rotor end

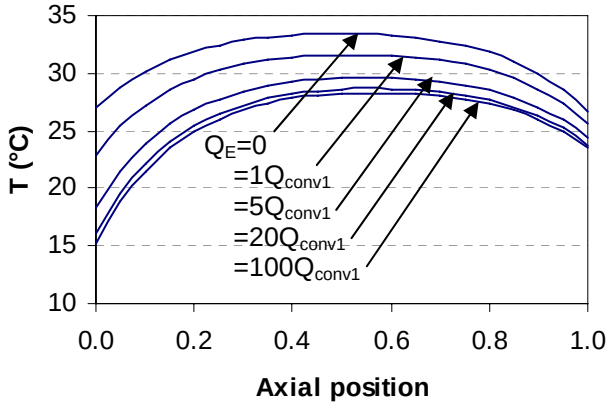

Fig. 5.25 Rotor temperature along the rotor axis for different heat fluxes at the rotor end, 60krpm, C=35μm

As Fig. 5.24 and Fig. 5.25 suggests, imposing heat flux boundary condition beyond five times the heat convection on the rotor surface yields similar rotor

temperature profile regardless of the level of the heat loss at the rotor end. The simulation also suggests minimum necessary amount of cooling for near-isothermal operation of the given rotor-bearing configuration. To better understand the effect of thermal expansion of the rotor on the rotor dynamic performance, linear perturbation analyses were performed following the procedure developed by [7,16]. For infinitesimal perturbation motions of the rotor and each pad, it is assumed the viscosity and air temperature remain the values evaluated at the final static equilibrium point.

Synchronous direct stiffness and damping coefficients for the three cases are compared in Fig. 5.26 and Fig. 5.27, where Case 3 is not plotted because it is very similar to Case 1. The stiff increase of direct stiffness at high speeds for Case 2 is attributed to the increased preload via the decreased nominal clearance by the rotor thermal expansion. Effect of different preloads on rotor imbalance response and natural frequencies can be found in [3]. The remarkable difference between the isothermal force coefficients (Case 0) and the non-isothermal coefficients (Case 1&2) at higher speeds justifies the necessity of thermal analyses for high speed turbomachinery.

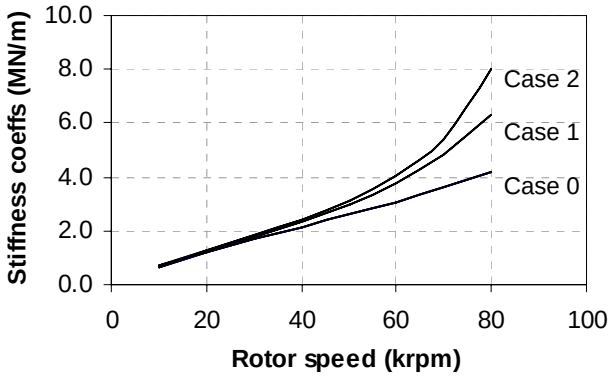

Fig. 5.26 Synchronous direct stiffness coefficients

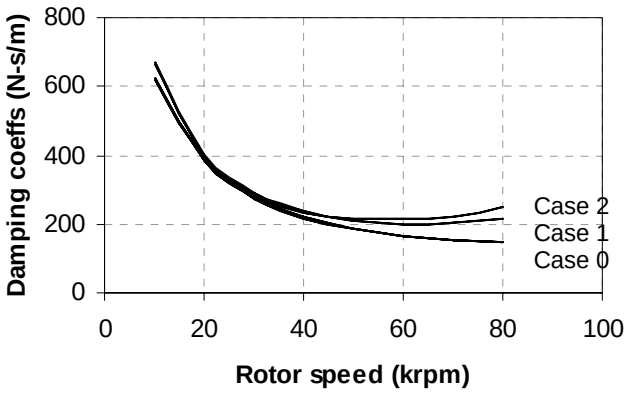

Fig. 5.27 Synchronous direct damping coefficients

5.4 Conclusion

A new THD model capable of predicting the thermal and rotordynamic performances of a rotor-bearing system with CFTPBs was presented. The new THD model solves the generalized Reynolds equation, 3-D energy equation, and energy balance equations for surrounding sub-domains including bearing shell and exposed rotor surface. Boundary conditions such as inlet flow temperature, rotor temperature, and pad temperature are also calculated simultaneously from iterative procedure to meet global thermal balance.

The developed THD model can handle general boundary conditions (temperature or heat flux) of the thermal sub-system for various system configurations and operating conditions. Once the bearing shell temperature and the thermal boundary conditions at the rotor end away from the bearing edge are known or measured, the developed THD model can estimate analytical temperature profiles of the rotor, tilting pad, and gas film.

It is expected that the thermal sub-module can be used to analyze and design various tilting pad bearings for a wide range of operation conditions. Linear perturbation analyses were also performed to investigate thermal effects on the bearing stiffness and damping coefficients.

Parametric studies on nominal clearance and external load were conducted to provide useful design guide. Nominal clearance showed significant influence on temperature fields, and external load had uneven thermal effects among pads. Case studies with heat flux and temperature boundary conditions were performed to present physical insight on thermal and rotordynamic behavior of various system configurations. Zero heat flux condition at the rotor end led to much higher temperature rise at high speeds than either heat flux or temperature boundary conditions, demonstrating the necessity of an adequate cooling system for high speed applications. Large rotor thermal growth due to the high rotor temperature showed significant influence on rotordynamic performance by increasing direct stiffness and damping coefficients. In addition, the large thermal growth at high speeds imposed an upper limit of operating speed to avoid system failure.

CHAPTER VI

FUTURE WORK AND CONCLUSION

In this chapter, future research related to this dissertation is proposed, and concluding remarks and contributions of this dissertation are presented.

6.1 Future Work: New Test Rig

For complete experimental studies on rotordynamic and thermal performance of CFTPBs with the developed simulation tools, a new test rig is desired to measure the rotor and pad temperatures as well as rotor position. Table 6.1 summarizes the features and capabilities of the new test rig, and Fig. 6.1 through Fig. 6.3 illustrate these items (the table and figures are from [39]).

Improved features from the current test rig are: AC motor driving of rotor for easier speed control and removal of driving air cooling effect, tap holes on the rotor end surfaces for imbalance masses, measurements of pad positions for pad dynamics, measurements of the rotor and pad temperatures for thermal studies, advanced control of the axial position of the rotor by new thrust bearing. With the new test rig, future thermal analyses and deeper insight into CFTPB behavior can be tested to compliment currently developed simulation tools.

Table 6.1 List of features and capabilities of new test rig design

Features

1. New 2 in. (50.8 mm) diameter rotor; mass approximately 13.7 lbm (6.2 kg)
2. New 3-pad CFTPBs
    a. Hybrid (hydrodynamic + hydrostatic) operation possible
    b. Special design allows thermal measurement capabilities
3. AC motor drive system capable of 70 krpm
4. Hydrostatic air thrust bearing

Capabilities

1. Imbalance response measurements
    a. Horizontal and vertical proximity probes at both bearings
    b. Rotor can accommodate insertion of additional imbalance masses to promote cylindrical or conical imbalance responses for rigid rotor modal vibration studies
2. Pad vibration measurements – proximity probes for top pads
3. Thermal measurements
    a. Special clearance in bearing allows for thermocouple measurement of pad temperatures
    b. View channel in housing and in bearing allows for IR thermometer measurement of rotor temperatures at bearing center and other locations adjacent to bearing

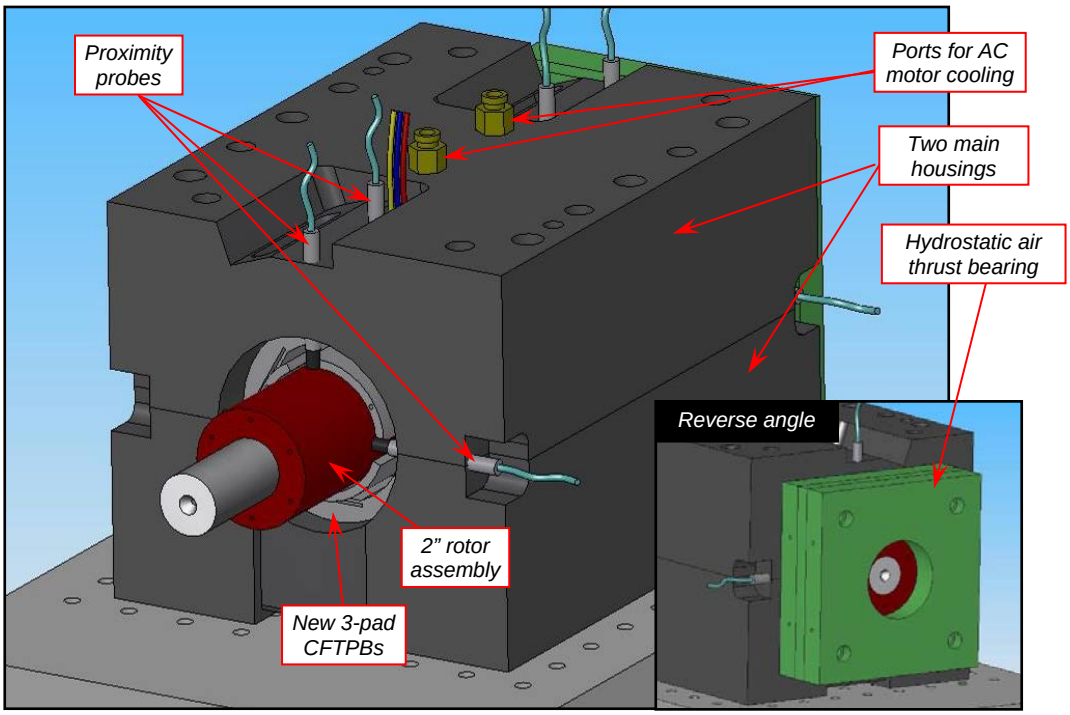

Fig. 6.1 New test rig design – assembly views

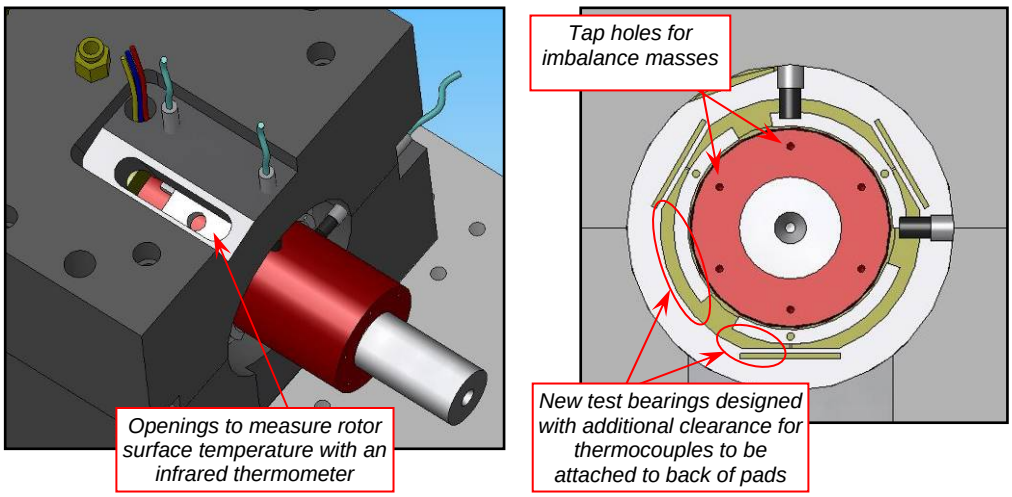

Fig. 6.2 New test rig design – thermal measurement capabilities

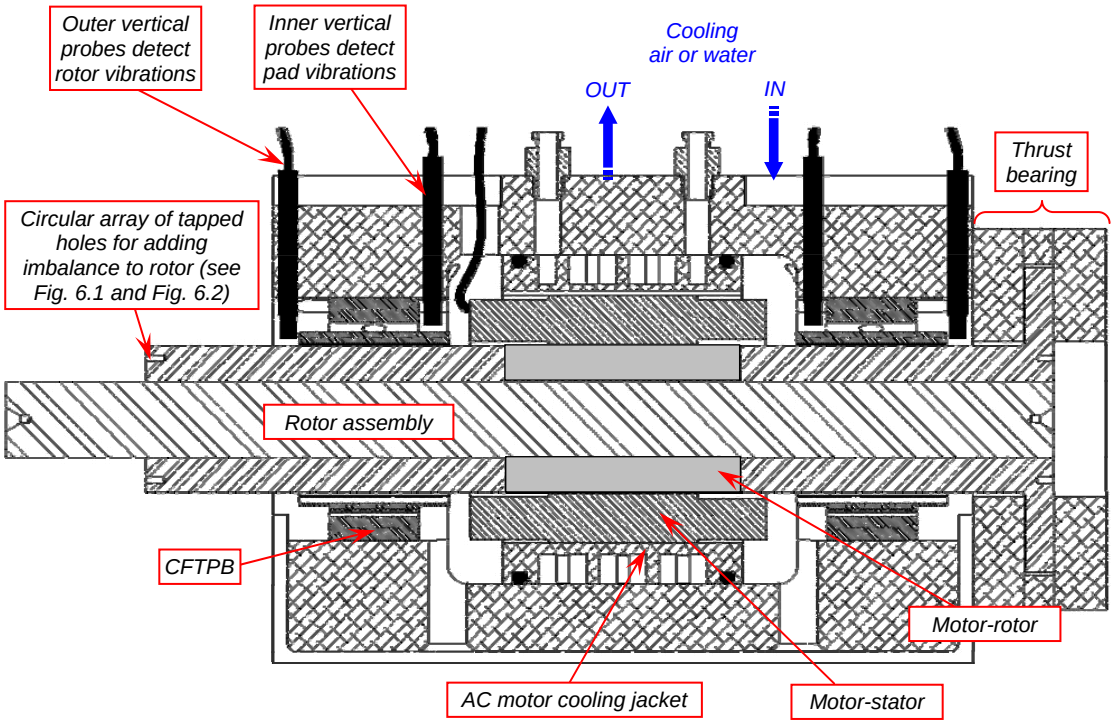

Fig. 6.3 New test rig design – center section view

6.2 Contributions and Conclusions

The main purpose of this dissertation is to present rotordynamic analyses with experimental validation to predict dynamic performance of compliant flexure pivot tilting pad bearings, and to develop a thermo-hydrodynamic model for a typical rotor-bearing system with compliant flexure pivot tilting pad bearings. Major contributions and conclusions are as follows.

1. A generalized orbit simulation program and a perturbation analysis program were developed for rotordynamic analyses of CFTPBs. The generalized orbit simulation

program deals with both translational and angular motions of a rigid rotor with two different bearings, and thus, the conical rotor vibration mode is evaluated as well as the cylindrical vibration mode. The perturbation analysis program for CFTPBs was developed to calculate synchronous force coefficients for XLTRC, and non-synchronous force coefficients for linear stability analyses based on the Lund method. The two linear and non-linear analytical methods are expected to provide comprehensive design and analysis tools for rotordynamic performance of CFTPBs.

2. A test rig was constructed for experimental investigation of rotordynamic performance of CFTPBs, and a data acquisition program based on LabVIEW was developed for measurements of coast-down response. The test rig is composed of two CFTPBs, one rotor assembly with impulse turbines, compressed air supply system for driving the rotor assembly, and data acquisition system with proximity probes and NI board. The LabVIEW program contains basic functions to present rotor orbits and Fast Fourier Transformation. The constructed test rig and data acquisition system is expected to be a foundation for future thermal studies.

3. A THD analysis program was developed for a thermal sub-system including half the rotor-bearing system. The developed THD model can handle general boundary conditions (temperature or heat flux) of the thermal sub-system to the environments for various system configurations and operating conditions. Once the bearing shell temperature and the thermal boundary conditions at the rotor end away from the bearing

edge are known or measured, the developed THD model can estimate analytical temperature profiles of the rotor, tilting pad, and gas film. It is expected that the thermal sub-module can be used to analyze and design various tilting pad bearings for a wide range of operation conditions. The THD analysis program also contains the linear perturbation analysis module for rotordynamic analyses considering thermal effects on the bearing stiffness and damping coefficients.

4. Parametric studies were performed to understand overall rotor-bearing system characteristics of CFTPBs. To fully understand the non-linear characteristics at high-speeds, nonlinear orbit simulations and coast down simulations were used. Higher preload and pivot offset increased both critical speeds of the rotor-bearing system and onset speeds of instability due to the increased wedge effect. A change of tilting stiffness has a little effect on the critical speed but smaller tilting stiffness increased onset speed of instability in a linear fashion reducing the WFR, which implies the change of tilting stiffness affects cross-coupled stiffness rather than direct system stiffness and damping at critical speed. Pad radial stiffness and nominal bearing clearance were very important design parameters at high speeds due to rotor growth. From the series of parametric studies, the maximum achievable rotor speed was limited by the minimum clearance at pivot calculated from the rotor growth and radial deflection of pads. Pad radial stiffness also affects rotor instability significantly. Small radial stiffness could accommodate rotor growth more effectively but deteriorated rotor instability. From parametric studies on a bearing with 28.5mm in diameter and 33.2mm in length, optimum pad radial stiffness

and bearing clearance are $1\sim2\times10^7$ N/m and 35μm, respectively, and the maximum achievable speed appears 180krpm. The final design with suggested optimum design variables could be also stable under relatively large destabilizing forces.

5. Imbalance coast-down response tests were performed for a rotor-bearing system with CFTPBs over rotor speeds less than 55 krpm. Overall rotor vibrations for all the imbalance modes were subjected to the conical vibration mode with the forward precession, and their major critical speeds were about 32 krpm. The predicted critical speeds for conical vibration mode were 31 and 34 krpm for the rear and front bearing, respectively. The double peaks occurred in the coast-down test for in-phase imbalance masses were found to result from the in-phase imbalance component from XLTRC. Stability coast-down tests were conducted with the vertical distance between the upper and lower parts of the bearings increased, in order for onset speed of instability to be placed in the operating speeds. In coast-down tests for stability, sub-synchronous instabilities were initiated at about 49 krpm with whirl speeds of 18 and 32 krpm (WFRs of 0.35 and 0.65, respectively). From the orbit simulations, onset speeds of instability were estimated to occur at 39 krpm with whirl speeds of 24.5 krpm. From the linear stability analyses with XLTRC and the perturbation analysis, the predicted onset speed of instability was 46 krpm with the critical speed of 26 krpm (WFR 0.57). On the whole, predictions of whirl speed by the generalized orbit simulations and the linear stability analyses showed good agreements to the averaged whirl speed of 25 krpm from the test, but the estimated onset speed of instability appeared lower than the measured instability.

6. A new THD model capable of predicting the thermal and rotordynamic performances of a rotor-bearing system with CFTPBs was developed. Parametric studies on nominal clearance and external load were conducted to provide useful design guide. Nominal clearance showed significant influence on temperature fields, and external load had uneven thermal effects among pads. Case studies with heat flux and temperature boundary conditions were performed to present physical insight on thermal and rotordynamic behavior of various system configurations. Zero heat flux condition at the rotor end led to much higher temperature rise at high speeds, demonstrating the necessity of an adequate cooling system for high speed applications. Large rotor thermal growth due to the high rotor temperature showed significant influence on rotordynamic performance by increasing direct stiffness and damping coefficients. In addition, the large thermal growth at high speeds imposed an upper limit of operating speed to avoid system failure.

REFERENCES

[1] Childs, D.W., 1993, *Turbomachinery Rotordynamics: Phenomena, Modeling, and Analysis*, John Wiley & Sons, New York.

[2] Chen, W.J., Zeidan, F.Y., and Jain, D., 1994, "Design, Analysis and Testing of High Performance Bearing in A High-Speed Integrally Geared Compressor," Proceedings of the 23rd Turbomachinery Symposium, Dallas, Texas, pp. 31-42.

[3] Sim, K., and Kim, D., 2007, “Design of Flexure Pivot Tilting Pad Gas Bearings for High Speed Oil-Free Micro Turbomachinery,” ASME Journal of Tribology, **129**, pp. 112-119.

[4] Zhu, X. and San Andres, L., 2004, "Rotordynamic Performance of Flexural Pivot Hydrostatic Gas Bearings for Oil-Free Turbomachinery", ASME Paper GT2004-53621.

[5] Zeidan, F. and Paquette, D.J., 1994, "Application of High-speed and High Performance Fluid Film Bearings in Rotating Machinery", Proceedings of the 23th Turbomachinery Symposium, Dallas, Texas, pp. 209-234.

[6] KMC bearing, Inc. (http://www.bearingsplus.com, access date: Sep’06).

[7] Delgado, A., Justak, J. F., and San Andrés, L., 2004, “Analysis of Performance and Rotordynamic Force Coefficients of Brush Seals with Reverse Rotation Ability,” ASME Paper GT-2004-53614.

[8] Kim, D., 2004, Design and Fabrication of Sub-Millimeter Scale Gas Bearings with Tungsten-Containing Diamond Like Carbon Coatings, PhD thesis, University of Texas at Austin.

[9] Kim, D., Lee, S., Bryant, M. D., and Ling, F. F., 2004, "Hydrodynamic Performance of Gas Microbearings," Mil. Eng., **126(**4), pp. 711–718.

[10] Cheng, H. S., and Pan, C. H. T., 1965, "Stability Analysis of Gas-Lubricated, Self Acting, Plain, Cylindrical, Journal Bearings of Finite Length Using Galerkin's Method," ASME J. Basic Eng., **87**(1), pp. 185–192.

[11] Castelli, V., and Elrod, H. G., 1965, "Solution of the Stability Problem for 360 Deg Self-Acting, Gas-Lubricated Bearings," ASME J. Basic Eng., **87(**1), pp. 199–210.

[12] Han, D. C., Park, S. S., Kim, W. J., and Kim, W. J., 1994, "A Study on the Characteristics of Externally Pressurized Gas Bearings," Precis. Eng., **16(**3), pp. 164–173.

[13] San Andrés, L., and Wilde, D., 2001, "Finite Element Analysis of Gas Bearings for Oil-Free Turbomachinery," Revue Européenne des Eléments Finis, **10(**6/7), pp. 769–790.

[14] Lund, J. W., 1964, "Spring and Damping Coefficients for the Tilting Pad Journal Bearing," ASLE Transactions, **7**, pp. 342-352.

[15] Lund, J. W., 1968, "Calculation of Stiffness and Damping Properties of Gas Bearings," Journal of Lubrication Technology, **90**(4), pp. 793-803.

[16] San Andrés, L., 2006, “Hybrid Flexure Pivot-Tilting Pad Gas Bearings: Analysis and Experimental Validation,” ASME Journal of Tribology, **128**, pp. 551-558.

[17] Cope., W. F., 1949, “Hydrodynamic Theory of film lubrication,” Proc. Royal Soc. A, **197**, pp. 201-216.

[18] Zienkiewicz, O., 1958, “Temperature Distribution within Lubrication Film between Parallel Bearing Surfaces and Its Effect on the Pressures Developed,” Proc. Conf. Lub. Wear Instn. Mech Engrs., London, **28**, pp. 135-141.

[19] Hunter, W., and Zienkiewicz, O., 1960, “Effect of Temperature Variation across the Lubrication Film in The Theory of Hydrodynamic Lubrication,” J. of Mech. Engr. Science, **2**(1), pp. 52-58.

[20] Dowson, D., 1962, “A Generalized Reynolds Equation for Fluid-Film Lubrication,” Int. J. Mech. Sci, **4**, pp. 159-170.

[21] Knight, J. D., and Barrett, L. E., 1988, “Analysis of Tilting Pad Journal Bearings with Heat Transfer Effects,” ASME Journal of Tribology, **110**, pp. 128-133.

[22] Taniguchi, S., Makino, T., Takeshita, K., and Ichimura, T., 1990, “A Thermohydrodynamic Analysis of Large Tilting Pad Journal Bearing in Laminar and Turbulent Flow Regimes with Mixing,” ASME Journal of Tribology, **112**, pp. 542-549.

[23] Kim, J., Palazzolo, A., and Gadangi, R., 1994, “TEHD Analysis for Tilting-Pad Journal Bearings Using Upwind Finite Element Method,” STLE Tribology Transactions, **37**, pp. 771-783.

[24] Fillon, M., Bligoud, J.-C, and Frene, J., 1992, “Experimental Study of Tilting-Pad Journal Bearings - Comparison with Theoretical Thermoelastohydrodynamic Results,” ASME Journal of Tribology, **114**, pp. 579-567.

[25] Khonsari, M. M., and Beaman, J. J., 1986, “Thermohydrodynamic Analysis of Laminar Incompressible Journal Bearings,” ASLE Transactions, **29**, pp. 141-150.

[26] Salei, M., Swanson, E., and Heshmat, H., 2001, “Thermal Features of Compliant Foil Bearings – Theory and Experiments,” ASME Journal of Tribology, **123**, pp. 566-571.

[27] Pinkus, O., and Bupara, S. S., 1979, “Adiabatic Solution for Finite Journal Bearings,” ASME Journal of Lubrication Technology, **101**, pp. 578-587.

[28] Peng, Z-C., and Khonsari, M. M., 2006, “A Thermohydrodynamic Analysis of Foil Journal Bearings,” ASME Journal of Tribology, **128**, pp. 534-541.

[29] Gere, J. M., and Timoshenko, S. P., 1997, *Mechanics of Materials*, PWS, Boston, pp. 881–886.

[30] Chapra, S. C., and Canale, R. P., 1989, *Numerical Methods for Engineers*, McGraw-Hill, New York, pp. 631–634.

[31] Patankar, S. V., 1980, Numerical Heat Transfer and Fluid Flow, McGraw-Hill, New York, Ch.5.

[32] Timoshenko, S. P. and Goodier, J. N., 1970, Theory of Elasticity, 3rd edition, McGraw-Hill, Singapore, pp. 80-83.

[33] Pinkus, O., and Bupara, S. S., 1979, “Adiabatic Solution for Finite Journal Bearings,” ASME J. Lubr. Technol., **101**, pp. 492–496.

[34] Lund, J. W., 1974, “Stability and Damped Critical speeds of a Flexible Rotor in Fluid-Film Bearings,” Journal of Engineering for Industry, **96**, pp. 509-517.

[35] Holman, J. P., 1997, *Heat Transfer, 8th edition*, McGraw-Hill, New York, pp. 44-47.

[36] Heshmat, H. and Pinkus, O., 1986, “Mixing Inlet Temperatures in Hydrodynamic Bearings,” ASME Journal of Tribology, **108**, pp. 231-248.

[37] Ettles, C., 1980, “The Analysis and Performance of Pivoted Pad Journal Bearings Considering Thermal and Elastic Effects,” ASME Journal of Lubrication Technology, **102**, pp.182-192.

[38] Mills, A. F., 1999, *Heat transfer, 2nd edition*, Prentice Hall, Upper Saddle River, New Jersey.

[39] Rimpel, A., and Kim, D., 2007, “Flexure-pivot Tilting Pad Gas Bearing with Viscoelastic and Foil Damper,” Technical Report TRC-B&C-5-07.

[40] Yum, K., 2002, Numerical simulation of micro air-lubricated journal bearings for 3-D micro actuators, MS Thesis, Mechanical Engineering, UT-Austin.

[41] White, F. M., 1994, *Fluid Mechanics, 3rd edition*, McGraw-Hill, Singapore.

APPENDIX A

FORMULATION OF PERTURBATION ANALYSIS AND LINEAR STABILITY

The perturbation analysis on CFTPBs for frequency-dependent force coefficients are formulated based on the derivation given in [7,15]. Overall procedures of the formulations are reviewed and presented in non-dimensional forms in this paper. For arbitrary pad and rotor position, non-dimensional local film thickness is described by

$$H(\theta) = 1 - R_g + \varepsilon_X \cos\theta + \varepsilon_Y \sin\theta - \Phi \sin\left(\theta - \theta_p\right) - \left(R_p - \Psi\right)\cos\left(\theta - \theta_p\right) + 0.5D\left|\cos\theta\right| \tag{A.1}$$

where ε_X and ε_Y are respective eccentricities of the journal center along the X and Y directions, Φ is the pad tilting angle ($=\phi R/C$), Ψ is the pad radial displacement ($=\delta/C$), R_g is the rotor centrifugal growth, R_p is the preload (distance between the bearing center and pad arc center), and D is the split offset. All the parameters above are non-dimensional (normalized by nominal bearing clearance C).

With the given film thickness, the pressure field can be obtained by solving unsteady, isothermal, continuum flow Reynolds Equation given by

$$\frac{\partial}{\partial\theta}\left(PH^3\frac{\partial P}{\partial\theta}\right) + \frac{\partial}{\partial Z}\left(PH^3\frac{\partial P}{\partial Z}\right) = \Lambda\frac{\partial}{\partial\theta}(PH) + \sigma\frac{\partial}{\partial\tau}(PH) \tag{A.2}$$

$$\Lambda = \frac{6\mu\Omega}{p_a}\left(\frac{R}{C}\right)^2,\ \sigma = \frac{12\mu\omega}{p_a}\left(\frac{R}{C}\right)^2$$

Here, P is a dimensionless pressure normalized by atmospheric pressure ($P=p/p_a$), μ is air viscosity, θ is a circumferential coordinate, Z is a dimensionless axial coordinate normalized by R ($Z=z/R$), and τ is a dimensionless time normalized by excitation frequency ($\tau=\omega t$). Λ is a bearing number defined using the rotor rotational frequency (Ω), and σ is a squeeze number. For discretization of the Reynolds equation, the power-law scheme [31] with finite difference methods is adapted to ensure all coefficients are not negative for convective terms with large Peclet numbers. Yum [40] showed that the power-law scheme has excellent numerical stability for high speed convections.

A.1 Dynamic Force Coefficients

In the perturbation analyses, a rotor is perturbed harmonically with small amplitudes ($\Delta\varepsilon_X$, $\Delta\varepsilon_Y$) with a frequency ω around an equilibrium point (ε_{X0}, ε_{Y0}) of interest, and the rotor perturbation induces perturbed motions of pads. The rotor and pad motions, therefore, are composed of static and dynamically perturbed terms, associated respectively with the equilibrium position and perturbation, and are given as:

$$\varepsilon_X = \varepsilon_{X0} + \Delta\varepsilon_X e^{i\tau},\ \varepsilon_Y = \varepsilon_{Y0} + \Delta\varepsilon_Y e^{i\tau} \quad \text{(A.3a)}$$

$$\Phi = \Phi_0 + \Delta\Phi e^{i\tau},\ \Psi = \Psi_0 + \Delta\Psi e^{i\tau} \quad \text{(A.3b)}$$

An equilibrium position of the rotor generates a static film thickness (H_0) and a static pressure field (P_0) on each pad with corresponding static pad positions (Φ_{p0}, Ψ_{p0}), and the perturbed motions of rotor and pads generate perturbed film thickness (ΔH) and pressure field (ΔP). Dynamic film thickness and pad pressure fields are given by:

$$H = H_0 + \Delta H e^{i\tau} \tag{A.4a}$$

$$P = P_0 + \Delta P e^{i\tau} \tag{A.4b}$$

where the perturbed film thickness and pressure field are summations of all the contributions from the perturbed motions of rotor and pads, i.e.,

$$\Delta H = H_X \Delta\varepsilon_X + H_Y \Delta\varepsilon_Y + H_\Phi \Delta\Phi + H_\Psi \Delta\Psi \tag{A.5a}$$

$$\Delta P = P_X \Delta\varepsilon_X + P_Y \Delta\varepsilon_Y + P_\Phi \Delta\Phi + P_\Psi \Delta\Psi \tag{A.5b}$$

where P_α and H_α are respectively a perturbed pressure gradient and a film thickness gradient with respect to each finite perturbation (α = X, Y, Φ, Ψ), given in the Table A.1 with the corresponding rotor and pad motions.

Substitution of Eqs. (A.4) and (A.5) into Eq. (A.2) yields one zeroth order nonlinear PDE for the equilibrium pressure field and four first order linear PDEs for the perturbed pressure fields, and given by:

$$\frac{\partial}{\partial\theta}(P_0 {H_0}^3 \frac{\partial P_0}{\partial\theta}) + \frac{\partial}{\partial Z}(P_0 {H_0}^3 \frac{\partial P_0}{\partial Z}) = \Lambda \frac{\partial}{\partial\theta}(P_0 H_0) \tag{A.6a}$$

$$\begin{aligned} &\frac{\partial}{\partial\theta}\left[\Lambda P_\alpha H_0 - P_0 {H_0}^3 \frac{\partial P_\alpha}{\partial\theta}\right] + \frac{\partial}{\partial Z}\left[-P_0 {H_0}^3 \frac{\partial P_\alpha}{\partial Z}\right] \\ &= \frac{\partial}{\partial\theta}\left[\left(3{H_0}^2 P_0 H_\alpha + {H_0}^3 P_\alpha\right)\left(\frac{\partial P_0}{\partial\theta}\right) - \Lambda P_0 H_\alpha\right] \\ &+ \frac{\partial}{\partial Z}\left[\left(3{H_0}^2 P_0 H_\alpha + {H_0}^3 P_\alpha\right)\left(\frac{\partial P_0}{\partial Z}\right)\right] - \sigma i\left(P_0 H_\alpha + P_\alpha H_0\right) \end{aligned} \tag{A.6b}$$

Table A.1 Perturbed pressure gradients and corresponding film thickness gradients

	P_α	H_α
ε_X	P_X	$\cos\theta$
ε_Y	P_Y	$\sin\theta$
Φ	P_Φ	$-\sin(\theta-\theta_p)$
Ψ	P_Ψ	$\cos(\theta-\theta_p)$

The pressure gradient fields for rotor (P_X, P_Y) and for pads (P_Φ, P_Ψ) are related to each other by a homogeneous condition that the two pressure gradient fields are balanced on each pad [7], and thus, the pressure gradient field for pad motion is described as

$$\begin{pmatrix} P_\Phi \\ P_\Psi \end{pmatrix} = \begin{bmatrix} \sin\theta_p & -\cos\theta_p \\ \cos\theta_p & \sin\theta_p \end{bmatrix} \begin{pmatrix} P_X \\ P_Y \end{pmatrix} \tag{A.7}$$

where the transformation matrix is corresponding to a coordinate transformation of the pad at the pivot to the bearing for the summation to be zero. Once all the pressure gradient fields are calculated, fluid film impedance coefficients are obtained by integrating each perturbed pressure field over each pad by the definitions of

$$\begin{pmatrix} Z_{X\alpha} \\ Z_{Y\alpha} \end{pmatrix} = -\iint P_{\alpha} \begin{pmatrix} \cos\theta \\ \sin\theta \end{pmatrix} d\theta dZ \tag{A.8a}$$

$$\begin{pmatrix} Z_{\Phi\alpha} \\ Z_{\Psi\alpha} \end{pmatrix} = \begin{bmatrix} \sin\theta_p & -\cos\theta_p \\ \cos\theta_p & \sin\theta_p \end{bmatrix} \begin{pmatrix} Z_{X\alpha} \\ Z_{Y\alpha} \end{pmatrix} \tag{A.8b}$$

Using the fluid film impedance matrix (Z), pad dynamic equations for the tilting and radial motions of each pad are described with matrices of pad mass (M_p) and structural stiffness (K_p), and given as

$$[M_p] \begin{pmatrix} \Phi'' \\ \Psi'' \end{pmatrix} + [K_p] \begin{pmatrix} \Phi \\ \Psi \end{pmatrix} = \begin{pmatrix} M_{p\Phi} \\ F_{p\Psi} \end{pmatrix} \tag{A.9}$$

$$[M_p] = \begin{bmatrix} I_p & 0 \\ 0 & M_p \end{bmatrix}, \; [K_p] = \begin{bmatrix} K_{p\Phi} & 0 \\ 0 & K_{p\Psi} \end{bmatrix}$$

where Φ'' and Ψ'' are time derivatives with respect to the non-dimensional time (τ). The moment and force applied to the pad along the tilting and radial directions are described with the static and perturbed terms using the fluid film impedance as

$$M_{p\Phi} = M_{p\Phi 0} - \left(Z_{\Phi X}\Delta\varepsilon_X + Z_{\Phi Y}\Delta\varepsilon_Y + Z_{\Phi\Phi}\Delta\Phi + Z_{\Phi\Psi}\Delta\Psi\right)e^{i\tau} \qquad \text{(A.10a)}$$

$$F_{p\Psi} = F_{p\Psi 0} - \left(Z_{\Psi X}\Delta\varepsilon_X + Z_{\Psi Y}\Delta\varepsilon_Y + Z_{\Psi\Phi}\Delta\Phi + Z_{\Psi\Psi}\Delta\Psi\right)e^{i\tau} \qquad \text{(A.10b)}$$

Substituting Eqs. (A.3) and (A.10) into Eq. (A.9) and canceling out the static equilibrium leads to the following perturbed equations for the pad radial and tilting motions:

$$\left(-\left[M_p\right]+\left[K_p\right]\right)\begin{pmatrix}\Delta\Phi\\ \Delta\Psi\end{pmatrix} = -\begin{bmatrix}Z_{\Phi X} & Z_{\Phi Y}\\ Z_{\Psi X} & Z_{\Psi Y}\end{bmatrix}\begin{pmatrix}\Delta\varepsilon_X\\ \Delta\varepsilon_Y\end{pmatrix} - \begin{bmatrix}Z_{\Phi\Phi} & Z_{\Phi\Psi}\\ Z_{\Psi\Phi} & Z_{\Psi\Psi}\end{bmatrix}\begin{pmatrix}\Delta\Phi\\ \Delta\Psi\end{pmatrix} \qquad \text{(A.11)}$$

Note that the excitation frequency (ω) of the perturbation has been distributed in the non-dimensional mass matrix (see the definition in Nomenclature). In the balance of the external force on the rotor with the bearing reaction force from the pads, the perturbed external load (ΔW_X, ΔW_Y) balances the perturbed bearing reaction force from all the pads, i.e.,

$$\begin{pmatrix}\Delta W_X\\ \Delta W_Y\end{pmatrix} = \sum_{pad}\left\{\begin{bmatrix}Z_{XX} & Z_{XY}\\ Z_{YX} & Z_{YY}\end{bmatrix}\begin{pmatrix}\Delta\varepsilon_X\\ \Delta\varepsilon_Y\end{pmatrix} + \begin{bmatrix}Z_{X\phi} & Z_{X\delta}\\ Z_{Y\phi} & Z_{Y\delta}\end{bmatrix}\begin{pmatrix}\Delta\Phi\\ \Delta\Psi\end{pmatrix}\right\} \qquad \text{(A.12)}$$

Isolating $(\Delta\Phi, \Delta\Psi)^T$ in Eq. (A.11) and replacing into Eq. (A.12), the perturbed equation of the rotor motion due to the external force is derived in terms of the fluid film impedance and the pad mass and structural stiffness (and damping) as

$$\begin{pmatrix} \Delta W_X \\ \Delta W_Y \end{pmatrix} = [Z_R] \begin{pmatrix} \Delta \varepsilon_X \\ \Delta \varepsilon_Y \end{pmatrix} \tag{A.13}$$

where the reduced fluid film impedance matrix is

$$[Z_R] = \sum_{pad} \left\{ \begin{bmatrix} Z_{XX} & Z_{XY} \\ Z_{YX} & Z_{YY} \end{bmatrix} - \begin{bmatrix} Z_{X\phi} & Z_{X\delta} \\ Z_{Y\phi} & Z_{Y\delta} \end{bmatrix} \left\{ \begin{bmatrix} Z_{\Phi\Phi} & Z_{\Phi\Psi} \\ Z_{\Psi\Phi} & Z_{\Psi\Psi} \end{bmatrix} - [M_p] + [K_p] \right\}^{-1} \begin{bmatrix} Z_{\Phi X} & Z_{\Phi Y} \\ Z_{\Psi X} & Z_{\Psi Y} \end{bmatrix} \right\} \tag{A.14}$$

The dimensional stiffness and damping coefficients for the lateral motion of rotor are derived from the non-dimensional reduced impedance coefficients by the definitions of

$$k_{\alpha\beta} = \frac{p_a R^2}{C} \mathrm{Re}\left([Z_R]_{\alpha\beta} \right) \tag{A.15a}$$

$$d_{\alpha\beta} = \frac{p_a R^2}{\omega C} \mathrm{Im}\left([Z_R]_{\alpha\beta} \right) \tag{A.15b}$$

and dimensional fluid film reduced impedance coefficients are $z_{\alpha\beta}=k_{\alpha\beta}+i\omega d_{\alpha\beta}$, where $\alpha=X,Y$ and $\beta=X,Y$.

A.2 Linear Stability Analyses

Stability analyses were performed by solving eigenvalue problems applied to gas bearings [15], using the reduced frequency-dependent impedance matrix. The homogeneous equation of the rotor motions is

$$\begin{bmatrix} m_r & 0 \\ 0 & m_r \end{bmatrix} \begin{Bmatrix} \ddot{x} \\ \ddot{y} \end{Bmatrix} + \begin{bmatrix} z_{XX} & z_{XY} \\ z_{YX} & z_{YY} \end{bmatrix} \begin{Bmatrix} x \\ y \end{Bmatrix} = 0 \tag{A.16}$$

where the impedance coefficients are dimensional values (Eq. 15). For solving eigenvalue problems, the homogeneous equation is restated as

$$\begin{bmatrix} z_{XX} - z_K & z_{XY} \\ z_{YX} & z_{YY} - z_K \end{bmatrix} \begin{Bmatrix} x \\ y \end{Bmatrix}_{K=b,f} = 0 \tag{A.17}$$

where modal impedance $z_K = -m_r\lambda^2$, $\lambda=\sigma\pm j\omega_s$, and ω_s is the excitation (or whirl) frequency. Subscripts b and f denote the backward and forward whirl motions, respectively. For having non-trivial solutions, the determinant of the combined impedance matrix (the characteristic equation) should be zero, and yields

$$z_{b,f} = \frac{z_{XX} + z_{YY}}{2} \pm \sqrt{\left(\frac{z_{XX} + z_{YY}}{2}\right)^2 - \left(z_{XX} z_{YY} - z_{XY} z_{YX}\right)} \tag{A.18}$$

where the positive and negative signs correspond to the backward and forward whirl, respectively. Instability (diverging amplitude) occurs when the real part of λ is positive, i.e. the onset of instability occurs at $\lambda=0\pm j\omega_s$ (called the neutral stability). At the onset of instability, the imaginary part of the modal impedance (modal damping) is zero, and the real part of the modal impedance (modal stiffness) becomes

$$k_{modal} = m_r\omega_s^2 \tag{A.19}$$

Considering only the forward whirl, Lund [15] suggested a simple way to find onset speed of instability and whirl frequency ratio (WFR) by substituting the homogeneous solution corresponding to the neutral stability into the homogeneous dynamic equation of Eq. (16). For a given running speed (Ω) at an equilibrium point of interest, frequency-dependent force coefficients are calculated at the excitation frequency (whirl frequency) $\omega_s=\Omega\xi$, where ξ is WFR. Modal stiffness is calculated with the force coefficients by

$$k_{\text{modal}} = \frac{d_{XX}k_{YY} + d_{YY}k_{XX} - d_{XY}k_{YX} - d_{YX}k_{XY}}{d_{XX} + d_{YY}} \tag{A.20}$$

WFR is updated with the modal stiffness by

$$\xi^2 = \frac{(k_{\mathrm{mod}\,al} - k_{XX})(k_{\mathrm{mod}\,al} - k_{YY}) - k_{XY}k_{YX}}{\Omega^2(c_{XX}c_{YY} - c_{XY}c_{YX})} \tag{A.21}$$

Iteration continues until ξ converges. The converged WFR and corresponding modal stiffness determine the critical mass from Eq. (A.19). If the current rotor mass is larger than the calculated critical mass, then the system is considered unstable. Whirl frequency (ω_s) is only valid at onset of instability because the whirl motion does not occur during stable operations.

APPENDIX B

DERIVATION AND DISCRETIZATION OF THE ENERGY EQUATION

B.1 Derivation of the Energy Equation

The steady state energy equation for compressible air flows in the thin film between rotor and bearing are derived from fundamental heat balances in an infinitesimal control volume, by using the equations of mass and momentum conversation and assuming the compressible air flows as the perfect gas and a Newtonian flow. Coordinates for the infinitesimal control volume are presented in Fig. B.1, where the axes of *x*, *y*, and *z* correspond to the circumferential, cross-film, and axial directions, respectively.

For compressible air flows, heat balances for the infinitesimal control volume yield the following equation with respect to the total stored energy [41]:

$$\rho\frac{de}{dt}+\nabla\cdot\left(pV\right)=\nabla\cdot(k\nabla T)+\nabla\cdot(V\cdot\tau_{ij}) \tag{B.1}$$

where e is the total stored energy per unit mass, ρ is the density, p is the hydrostatic pressure, V is the velocity vector, τ_{ij} is the viscous stress tensor, k is the heat conduction coefficient, T is the fluid temperature. The total stored energy is described in terms of the molecular internal energy ($\hat{u}$) and the kinetic and potential energy as

$$e = \hat{u} + \frac{1}{2}V^2 + gy \tag{B.2}$$

where g is the gravitational constant. The net viscous work $\nabla \cdot (V \cdot \tau_{ij})$ in Eq. (B.1) is split up into

$$\nabla \cdot \left(V \cdot \tau_{ij}\right) = V \cdot \left(\nabla \cdot \tau_{ij}\right) + \Phi \tag{B.3}$$

, where Φ is the viscous-dissipation function[1] ($\Phi = \tau_{ij} : \nabla V$). For a Newtonian fluid, the viscous-dissipation function is described as:

$$\begin{aligned} \frac{\Phi}{\mu} = 2\left\{\left(\frac{\partial u}{\partial x}\right)^2 + \left(\frac{\partial v}{\partial y}\right)^2 + \left(\frac{\partial w}{\partial z}\right)^2\right\} \\ + \left(\frac{\partial v}{\partial x} + \frac{\partial u}{\partial y}\right)^2 + \left(\frac{\partial w}{\partial y} + \frac{\partial v}{\partial z}\right)^2 + \left(\frac{\partial u}{\partial z} + \frac{\partial w}{\partial x}\right)^2 - \frac{2}{3}\left(\frac{\partial u}{\partial x} + \frac{\partial v}{\partial y} + \frac{\partial w}{\partial z}\right)^2 \end{aligned} \tag{B.4}$$

By combining the linear momentum equation $\rho g - \nabla p + \nabla \cdot \tau_{ij} = \rho \frac{dV}{dt}$ to Eq. (B.1) to eliminate $\nabla \cdot \tau_{ij}$ and rearranging it[2], the energy equation with respect to the internal energy becomes

---

[1] The double dot product for the symmetric tensor is A:B = $A_{xx}B_{xx}$+ $A_{yy}B_{yy}$+ $A_{zz}B_{zz}$.

[2] $\nabla \cdot \left(V \cdot \tau_{ij}\right) = V \cdot \left(-\rho g + \nabla p + \rho \frac{dV}{dt}\right) + \Phi$, $\rho \frac{d}{dt}\left(\frac{1}{2}V^2 + g_z z\right) + \nabla \cdot (pV) = V \cdot \left(\rho \frac{dV}{dt}\right) - V \cdot (\rho g) + V \cdot (\nabla p) + p(\nabla \cdot V)$

$$\rho\frac{d\hat{u}}{dt}+p(\nabla\cdot V)=\nabla\cdot(k\nabla T)+\Phi \tag{B.5}$$

where the internal energy is a function of temperature ($d\hat{u}=c_v dT$).

By using the relation of the internal energy to the enthalpy ($h=\hat{u}+\frac{p}{\rho}$) and the mass conservation[3] ($\frac{\partial\rho}{\partial t}+\nabla\cdot(\rho V)=0$), the energy equation is derived with respect to the enthalpy as:

$$\rho\frac{d\hat{h}}{dt}-\frac{dp}{dt}=\nabla\cdot(k\nabla T)+\Phi \tag{B.6}$$

By eliminating the time-dependent terms, the energy equation for steady state air flows in the thin film between rotor and bearing assuming the perfect gas with constant specific heat becomes:

$$\rho c_p V\cdot\nabla T=\nabla\cdot(k\nabla T)+V\cdot\nabla p+\Phi \tag{B.7a}$$

$$\rho c_p\left(u\frac{\partial T}{\partial x}+v\frac{\partial T}{\partial y}+w\frac{\partial T}{\partial z}\right)=k\left(\frac{\partial^2 T}{\partial x^2}+\frac{\partial^2 T}{\partial z^2}+\frac{\partial^2 T}{\partial y^2}\right)+\left(u\frac{\partial p}{\partial x}+w\frac{\partial p}{\partial z}\right)+\Phi \tag{B.7b}$$

---

[3] By using the mass conservation $\frac{\partial\rho}{\partial t}+\nabla\cdot(\rho V)=\frac{\partial\rho}{\partial t}+V\cdot\nabla\rho+\rho\nabla\cdot V=\frac{d\rho}{dt}+\rho\nabla\cdot V=0$, the LHS of Eq. (B.2) becomes $\rho\frac{d\hat{u}}{dt}+p(\nabla\cdot V)=\rho\frac{d}{dt}\left(\hat{h}-\frac{p}{\rho}\right)-\frac{p}{\rho}\frac{d\rho}{dt}=\rho\frac{d\hat{h}}{dt}-\rho\frac{d}{dt}\left(\frac{p}{\rho}\right)-\frac{p}{\rho}\frac{d\rho}{dt}=\rho\frac{d\hat{h}}{dt}-\frac{dp}{dt}$

where the pressure gradients with respect to y is zero from the momentum equation in the y direction. The viscous-dissipation function, simplified with the assumption that all the velocity gradients except for $\partial u/\partial y$ and $\partial w/\partial y$ are negligible [28], is given as:

$$\Phi = \mu\left[\left(\frac{\partial u}{\partial y}\right)^2 + \left(\frac{\partial w}{\partial y}\right)^2\right] \tag{B.8}$$

Finally, Eqs. (B.7) and (B.8) are used to analyze heat transfer within the air film by the following discretization of the energy equation for numerical computations.

B.2 Discretization of the Energy Equation

Discretization of the energy equation is performed in a general form following the Patankar notation [31]. The energy equation given in Eq. (B.7) is composed of the terms for the heat convection, the heat diffusion (conduction), and the heat generation, and described by the general variable (ϕ), the diffusion factor (Γ), and the heat generation (S) as:

$$\rho\left(u\frac{\partial \phi}{\partial x} + v\frac{\partial \phi}{\partial y} + w\frac{\partial \phi}{\partial z}\right) = \Gamma\left(\frac{\partial^2 \phi}{\partial x^2} + \frac{\partial^2 \phi}{\partial y^2} + \frac{\partial^2 \phi}{\partial z^2}\right) + S \tag{B.9}$$

, where

$$\phi = T,\ \Gamma = \frac{k}{c_p},\ S = \frac{1}{c_p}\left[\left(u\frac{\partial p}{\partial x} + w\frac{\partial p}{\partial z}\right) + \mu\left[\left(\frac{\partial u}{\partial y}\right)^2 + \left(\frac{\partial w}{\partial y}\right)^2\right]\right]$$

The generalized energy equation Eq. (B.9) are expressed in terms of the total flux (J) from/to a control volume in the x, y and z direction. The total heat flux including the heat convection and heat dissipation are defined as $J_x \equiv \rho u\phi - \Gamma\frac{\partial \phi}{\partial x}$, $J_y \equiv \rho v\phi - \Gamma\frac{\partial \phi}{\partial y}$, and $J_z \equiv \rho w\phi - \Gamma\frac{\partial \phi}{\partial z}$, where the first term in the RHS is of the heat convection and the second is of the heat dissipation. The generalized energy equation is converted with the total fluxes at the boundaries of the control volume to:

$$\begin{aligned}&\left(J_e - F_e\phi_P\right) - \left(J_w - F_w\phi_P\right) + \\ &\left(J_n - F_n\phi_P\right) - \left(J_s - F_s\phi_P\right) + \\ &\left(J_t - F_t\phi_P\right) - \left(J_b - F_b\phi_P\right) = S\Delta x\Delta y\Delta z\end{aligned} \tag{B.10}$$

, where

$$J_e = \left(\rho u\phi - \Gamma\frac{\partial \phi}{\partial x}\right)\Delta y\Delta z,\ J_n = \left(\rho w\phi - \Gamma\frac{\partial \phi}{\partial z}\right)\Delta x\Delta y,\ J_t = \left(\rho v\phi - \Gamma\frac{\partial \phi}{\partial y}\right)\Delta x\Delta z$$

$$F_e = (\rho u)_e\Delta y\Delta z,\ F_n = (\rho w)_n\Delta x\Delta y,\ F_t = (\rho v)_b\Delta x\Delta z$$

$$D_e = \frac{\Gamma}{\Delta x}\Delta y\Delta z,\ D_n = \frac{\Gamma}{\Delta z}\Delta x\Delta y,\ D_t = \frac{\Gamma}{\Delta y}\Delta x\Delta z$$

J_i is an integrated value of the total heat flux over its crossing surface in Fig. B.1, and F_i and D_i are the convection and diffusion factors of the total heat fluxs (i = *e, w, n, s, b, t,* denoting the east, west, north, south, bottom, top boundaries of the control volume).

Substituting the total flux with the convection (F) and diffusion (D) terms (Eq. (B.10b) to Eq. (B.10a) employing the power-law scheme [31], the discretized energy equation becomes:

$$a_P\phi_P = a_E\phi_E + a_W\phi_W + a_N\phi_N + a_S\phi_S + a_T\phi_T + a_B\phi_B + b \tag{B.11}$$

, where

$$a_E = D_e A(|P_e|) + \|-F_e, 0\|$$

$$a_W = D_w A(|P_w|) + \|F_w, 0\|$$

$$a_N = D_n A(|P_n|) + \|-F_n, 0\|$$

$$a_S = D_s A(|P_s|) + \|F_s, 0\|$$

$$a_T = D_t A(|P_t|) + \|-F_t, 0\|$$

$$a_B = D_b A(|P_b|) + \|F_b, 0\|$$

$$a_P = a_E + a_W + a_N + a_S + a_T + a_B - S_P\Delta x\Delta y\Delta z$$

$$b = S_C\Delta x\Delta y\Delta z$$

Substituting the linear viscosity-temperature correlation, $\mu=a_1(T+a_2)$ where $a_1=4\times10^{-8}$ and $a_2=458.75$ [26], into the source term yields

$$S = S_C + S_P \phi_P \tag{B.12}$$

, where

$$S_P = \frac{a_1}{c_p}\left[\left(\frac{\partial u}{\partial y}\right)^2 + \left(\frac{\partial w}{\partial y}\right)^2\right],\ S_C = \frac{1}{c_p}\left(u\frac{\partial p}{\partial x} + w\frac{\partial p}{\partial z}\right) + \frac{a_1 a_2}{c_p}\left[\left(\frac{\partial u}{\partial y}\right)^2 + \left(\frac{\partial w}{\partial y}\right)^2\right]$$

The pressure gradients are calculated from given pressure fields, and the velocities and velocity gradients are given by the momentum equations and velocity boundary conditions on the rotor and bearing surface.

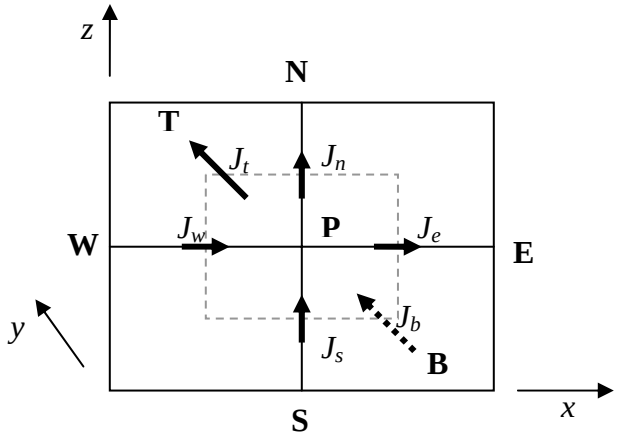

Fig. B.1 Total heat flux from/to control volume

VITA

Kyu-Ho Sim was born in Sangju, Republic of Korea in 1974. He received his Bachelor of Science degree in mechanical engineering from Yeonsei University, Seoul, Korea in 2000. After completing his B.S., he began his graduate studies at KAIST in mechanical engineering and earned his M.S. degree in 2002. His master's coursework emphasis was on computational solid mechanics. He completed his Ph.D. program at Texas A&M University in the Department of Mechanical Engineering under the supervision of Dr. Daejong Kim in 2007. His research interests include experimental studies and numerical analyses on rotordynamic systems with fluid bearings.

Mr. Kyu-Ho Sim may be reached at Texas A&M University, Department of Mechanical Engineering, 3123 TAMU, College Station, Texas 77843-3123. His email address is sim@tamu.edu.

This dissertation was typed by the author.